POST-COMMON ENVELOPE PRE-CATACLYSMIC AND CATACLYSMIC VARIABLE BINARIES

by

David Kent Sing

A Dissertation Submitted to the Faculty of the

DEPARTMENT OF PHYSICS

In Partial Fulfillment of the Requirements
For the Degree of

DOCTOR OF PHILOSOPHY

In the Graduate College

THE UNIVERSITY OF ARIZONA

2 0 0 5

THE UNIVERSITY OF ARIZONA
GRADUATE COLLEGE

As members of the Final Examination Committee, we certify that we have read the dissertation prepared by David Kent Sing
entitled Post-Common Envelope Pre-Cataclysmic and Cataclysmic Variable Binaries and recommend that it be accepted as fulfilling the dissertation requirement for the Degree of Doctor of Philosophy.

Date: 16 December 2005
Dr. Jay Holberg

Date: 16 December 2005
Dr. Michael Shupe

Date: 16 December 2005
Dr. Li-Zhi Fang

Date: 16 December 2005
Dr. James Liebert

Date: 16 December 2005
Dr. William Bickel

Final approval and acceptance of this dissertation is contingent upon the candidate's submission of the final copies of the dissertation to the Graduate College.

I hereby certify that I have read this dissertation prepared under my direction and recommend that it be accepted as fulfilling the dissertation requirement.

Date: 16 December 2005
Dissertation Director: Dr. Jay Holberg

STATEMENT BY AUTHOR

This dissertation has been submitted in partial fulfillment of requirements for an advanced degree at The University of Arizona and is deposited in the University Library to be made available to borrowers under rules of the Library.

Brief quotations from this dissertation are allowable without special permission, provided that accurate acknowledgment of source is made. Requests for permission for extended quotation from or reproduction of this manuscript in whole or in part may be granted by the head of the major department or the Dean of the Graduate College when in his or her judgment the proposed use of the material is in the interests of scholarship. In all other instances, however, permission must be obtained from the author.

SIGNED: _____

David Kent Sing

ACKNOWLEDGEMENTS

Analysis of the *FUSE* observations of HS1136+6646 were supported by NASA grant NAG5-10700 and those of V405 Aurigae by a NASA grant to Dr. Steve Howell. The analysis of the *STIS* observations of HS1136+6646 were supported by *HST* grant 09769. This research has made use of the USNOFS Image and Catalog Archive operated by the United States Naval Observatory, Flagstaff Station (http://www.nofs.navy.mil/data/fchpix/). Based on observations made with the NASA-CNES-CSA Far Ultraviolet Spectroscopic Explorer. FUSE is operated for NASA by the Johns Hopkins University under NASA contract NAS5-32985. Based on observations made with the NASA/ESA Hubble Space Telescope, obtained at the Space Telescope Science Institute, which is operated by the Association of Universities for Research in Astronomy, Inc., under NASA contract NAS 5-26555. These observations are associated with program #9769. Based on observations from Kitt Peak National Observatory, National Optical Astronomy Observatory, which is operated by the Association of Universities for Research in Astronomy, Inc., under cooperative agreement with the National Science Foundation. Based on observations from telescopes owned by the University of Arizona and operated by Steward Observatory in Tucson Arizona.

Some of the results in this dissertation have been reported in the following papers:

Sing D. K., Holberg J. B., Barstow M. A., Burleigh M., Good S., Oswalt T., Howell S., Brinkworth C., Rudkin M., Johnston K., & Rafferty S.
Spectroscopic and Photometric Analysis of HS1136+6646: A Hot Young DAO+K7V Post-Common Envelope Pre-Cataclysmic Variable Binary
2004, AJ, 127, 2396

Sing D. K., Howell S. B., Szkody P., and Cordova F. A
Far Ultraviolet Spectroscopic Explorer Spectroscopy of the Transitional Magnetic Cataclysmic Variable V405 Aurigae
2004, PASP, 116, 1056

Sing D. K., Holberg J. B., Burleigh M., Good S., Barstow M. A., Oswalt T. & Howell S.
FUSE Analysis of the Pre-Intermediate Polar Candidate HS1136+6646
2005, MNRAS, submitted.

DEDICATION

I would like to dedicate this work to my advisor Jay Holberg. His unwaivering support, beginning with my time as an undergraduate and continuing throughout my entire graduate career, provided me with the foundation I needed to successfully pursue science. His natural physical insight and extensive experience has been the guiding light in the success of my research. I also dedicate this work to my family and fiance who continues to teach me how to live and finally God, teaching me how to love.

TABLE OF CONTENTS

TABLE OF CONTENTS – *Continued*

TABLE OF CONTENTS – *Continued*

LIST OF FIGURES

LIST OF FIGURES – *Continued*

LIST OF FIGURES – *Continued*

LIST OF TABLES

ABSTRACT

Extensive photometric and spectroscopic observations have been obtained for the binary HS1136+6646, a newly formed post-common envelope binary system containing a hot ∼DAO.5 primary and a highly irradiated secondary. H1136+6646 is the most extreme example yet of a class of short period systems containing a hot H-rich white dwarf with a K-M companion. An orbital period of 0.83607 ± 0.00003 days has been determined through the phasing of radial velocities, emission line equivalent widths, and photometric measurements spanning a range of 24 months. Radial velocity measurements yield an amplitude of K_{WD} = 69 ±2 km s^{-1} for the white dwarf and K_{K7V} = 115 ± 1 km s^{-1} for the secondary star. Photometric measurements revealed a low amplitude modulation with a period of 234 minutes, associated with the rotation of the white dwarf. The white dwarf is estimated to have an effective temperature and gravity of ∼100,000 K and log g∼8.29 respectively, indicating the binary system is the second earliest post-CE objects known, having an age around 6.4x10^5 years. Indications are that the secondary star is overly luminous for its mass.

I also present *FUSE* observations of the magnetic cataclysmic variable V405 Aurigae. Together with four other DQ Her type binaries, V405 Aur forms a small subclass of intermediate polars which are likely to evolve into low magnetic field strength polars. The *FUSE* spectrum exhibits broad O VI and C III emission-lines as well as a narrow O VI emission-line component which likely forms near the white dwarf surface in an optically thin gas. Radial velocity measurements restrict any orbital modulation to a very low amplitude (K$_{WD}$ =2.5 ± 0.5 km s^{-1}) indicating that the binary system is at low inclination.

Recent photometric and spectroscopic observations have revealed J0644+3344 to be a bright, deeply eclipsing cataclysmic variable binary with a 6.46488± 0.00024

hour period. Although the nature of the hot component is not presently clear, J0644+3344 is one of the brightest eclipsing nova-like cataclysmic variable system yet. As such, the possibility exists for an unambiguous determination of the masses and temperatures of both components in future studies.

CHAPTER 1

Introduction

1.1 Interacting Binary Stars

The majority of stars in the galaxy do not exist alone, as our sun, but rather are a members of binary, triple, or even higher order multiple star systems. Most binary stars have little interaction during their hydrogen burning main sequence lifetimes. A star towards the end of its main sequence lifetime, however, undergoes a radical change from a small dwarf star into a large giant, opening up the possibility of interaction with its binary companion. The end products of stellar evolution in such binary systems include some of the most exotic objects in astronomy such as:

- cataclysmic variables, consisting of an accreting white dwarf primary star and low-mass secondary star
- low mass X-ray binaries, consisting of either a neutron star or a black hole primary, and a low-mass secondary which is filling its Roche lobe
- millisecond pulsars, consisting of a spun up accreting neutron star and a low-mass secondary
- type Ia supernovae, produced when either binary star accretion or a double degenerate merger causes a C/O white dwarf to exceed the Chandrasekhar mass limit.

The evolutionary phase that brings the binary star pair closer together, is called the common-envelope process. First theorized by Paczynski (1976) to explain cataclysmic variables, this important and little understood mechanism has far reaching consequences for the evolution of close binary stars.

1.2 Evolution of Close Binary Stars

1.2.1 Common-Envelope Evolution

In the standard evolutionary scheme for interacting close binary systems, a moderately separated pair of main sequence stars are brought into close proximity through the common-envelope (CE) process. During this short lived phase, the more massive star of the binary pair evolves to fill its Roche-lobe. Mass inside the Roche-lobe is gravitationally bound to the star. However, once the lobe of the primary star is filled, mass transfer onto the secondary star begins. Accreting mass from the more massive primary star to the secondary causes the orbital separation, and Roche-lobe, to contract resulting in an increased mass transfer rate. The mass transfer rate ultimately becomes too large for the secondary star to accommodate. The secondary star's Roche-lobe also fills, ultimately extending the primary star's atmosphere around both binary components, forming a CE. In the standard α-formalism developed by (Paczynski 1976, see §1.6.1), the secondary star helps eject the outer layers of the CE with efficiency α, usually resulting in a newly detached post common-envelope binary (PCEB). The resulting binary usually consists of a subdwarf or white dwarf (WD) primary together with a low mass main sequence secondary, in a much tighter orbit compared to its pre-CE state. Depending on initial conditions, a second CE phase may occur when the secondary star evolves off of the main sequence ultimately forming a double degenerate system. When this occurs, the evolving degenerate core of the secondary star can be stripped of its envelope, truncating its growth before He burning can proceed to completion. The result is a low mass ($M_{core} < 0.47\ M_{\odot}$) degenerate He core white dwarf. The entire CE phase is very short lived, perhaps lasting only one to one hundred years. With such a short lifespan, it is virtually impossible to expect to directly observe a binary system in the CE phase.

Computer modeling of the CE phase has also proven to be very difficult, yielding little insight. Our knowledge of this key evolutionary phase is thus dependent on observations of stars which have already undergone the CE process. Such post-CE binaries provide the necessary limiting cases for testing current CE theories.

1.2.2 Post-Common Envelope Evolution

PCEBs with sufficiently short orbital periods and with favorable mass ratios are dubbed to be pre-cataclysmic variable (CV) binaries. In Pre-CVs, the primary star's remnant, a white dwarf, is more massive than the secondary star, eventually resulting in stable mass transfer during its CV lifetime. The separation (and period) also has to be sufficiently small so that the binary can come into contact. In these pre-CVs, angular momentum loss mechanisms such as gravitational wave emission (see Appendix A) and magnetic braking (see Appendix B), slowly decrease the orbital separation until the Roche-lobe contracts the surface of the secondary star or the secondary star evolves off the main sequence. With the secondary star's Roche lobe filled, stable mass transfer onto the primary star can ensue. Although mass transfer from the less massive secondary star to the more massive primary acts to separate the two stars, continued angular momentum loss keeps the binary star interacting, turning the system into a CV.

1.2.3 Cataclysmic Variables

Cataclysmic variables (CVs) are close interacting binary star systems consisting of a white dwarf (WD) primary and a late type secondary which overflows its Roche lobe, often forming an accretion disk. In most CVs, the luminosity of the accretion disk dominates over the stellar components. In the simplest models, an accretion disk consists of concentric rings of material in which the temperature of the material in the disk decreases with radius. Accretion gas is processed through the accretion disk and ultimately onto the surface of the white dwarf star where about half of the kinetic energy is emitted as short wavelength radiation, X-ray and EUV radiation. The accretion process is often not stable, resulting in recurrent outbursts from which cataclysmic variables derive their name.

Magnetic CVs make up a particular subclass in which the magnetic field of the WD influences the accretion flow from its companion. Magnetic CVs have two distinct subclasses, polars (or AM Her binaries) and intermediate polars (IPs or DQ

Her binaries). In polars, the white dwarf rotates synchronously with its companion and possesses a sufficiently strong magnetic field ($\sim$ 10-100 MG) which prevents an accretion disk from forming. Synchrotron radiation is often emitted in these systems, as electrons spiral down the converging field lines near the poles. The mass transfer stream is instead funneled into accretion columns terminating at one or both magnetic poles. In intermediate polars, the WD rotates asynchronously with its companion, developing a partial accretion disk before the material is channeled onto the white dwarf. The partially collimated material in IPs falls onto the magnetic poles of the WD, usually releasing its kinetic energy via thermal bremsstrahlung in the hard X-ray through the UV range. Modulation of the X-ray and EUV spectrum can be attributed to self occultation of the WD and/or photo-electric absorption. It is thought that as IPs evolve to shorter orbital periods, the WD's magnetic field will eventually synchronize its rotation with the orbit and the system will become a polar (Howell et al., 2001).

1.3 Observed Post-Common Envelope Binaries

1.3.1 Identification

PCEBs are usually identified in photometric and spectroscopic surveys by eclipses, large radial velocity variations or, more commonly, through the discovery of a reflection effect (see Schreiber and Gänsicke 2003 for the discovery history of most PCEB pre-cataclysmic variable systems). The reflection effect is characterized by strong narrow optical emission lines and a photometric modulation on the orbital period. Ultraviolet radiation from a hot young subdwarf or WD heats the exposed hemisphere of the secondary star. This radiation gets reprocessed by a fluorescence effect, being emitted at longer wavelengths. The heated hemisphere of the cool secondary effectively produces an inverted optically thin photoshere with a positive (with radius) thermal gradient. Typically the hydrogen Balmer series and He I optical lines are the most prominent and, with their narrow full-with at half-maximum (FWHM), can easily be distinguished from wide Doppler-broadened accretion disk

emission lines. For example, the resolved Hα emission line seen in HS1136+6646 has a FWHM width of $\sim$300 km s^{-1} (Sing et al., 2004a), while a full accretion disk in a non-magnetic CV typically have widths thousands of km s^{-1} (Marsh and Horne, 1988). These narrow emission lines often elude surveys, sometimes requiring high-resolution spectra over an entire orbital period for detection.

1.3.2 Spectral Energy Distribution

Post-common (CE) pre-cataclysmic variable binaries frequently exhibit composite spectra, showing features from both the primary, either WD or sdB/sdO, and the late type secondary main sequence star. In the optical, hot white dwarf or sdB/sdO primaries dominate the continuum at shorter wavelengths, while the secondary star dominates at long wavelengths (see Figure 1.1). In older post-CE systems, or ones with earlier type secondary stars, the primary star can be difficult to observe, being much smaller and fainter than its companion. These systems often go undetected in photometric surveys and require additional information, such as a UV excess, for detection. Thus the current sample of well studied pre-CVs contain a strong selection bias toward young hot systems (see Schreiber and Gänsicke 2003).

In order to effectively study a binary system such as HS1136+6646, multi-wavelength observations are often essential to understanding many aspects of the system. As evident from the spectral energy distribution of this system shown in Figure 1.1, the far ultraviolet (UV) and UV regions are dominated by the hot white dwarf, while the red and infrared are dominated by the cool secondary. The white dwarf is most effectively studied in the far UV and UV, where it is possible to accurately measure its orbital motion, measure its gravitational redshift, determine the heavy element content of the photosphere, and find evidence of a magnetic field. In the optical, the properties of the secondary star are most evident. For example, the spectral type , its orbital motion, and its mass can be determined. As will be evident, the task of elucidating this system required observations from two NASA spacecraft (*FUSE* and *HST*) as well as spectroscopic and photometric observations from six ground based telescopes, all spanning a four year period.

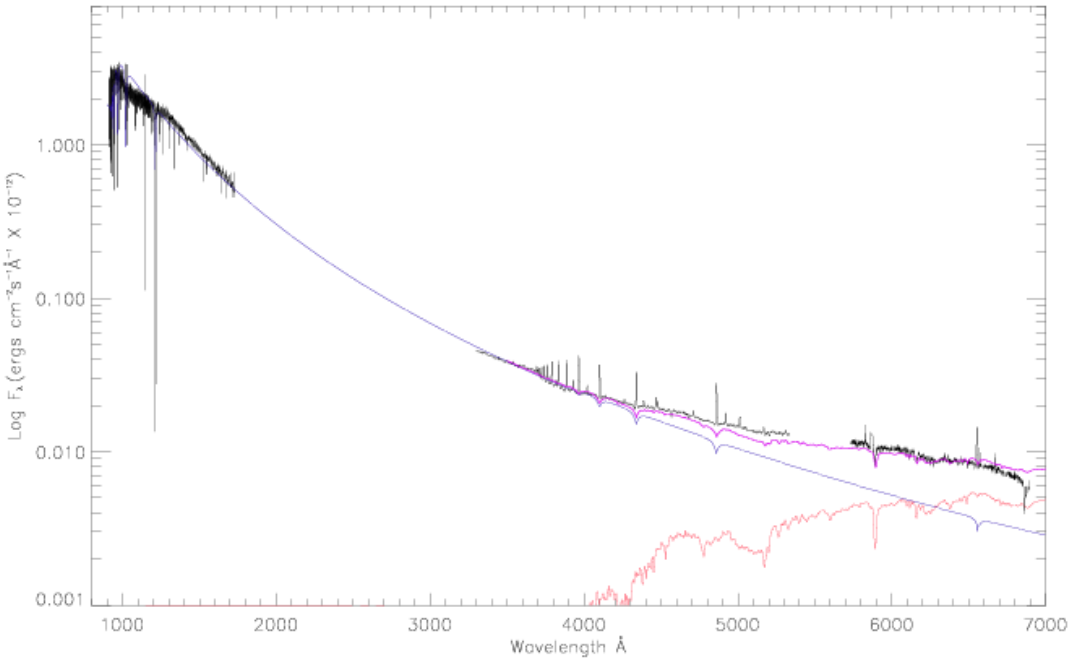

Figure 1.1: The spectral energy distribution of HS1136+6646 from the far ultraviolet to the optical wavelengths. The white dwarf star dominates the continuum shortward of 6000 Å. Plotted is the *FUSE*, *HST*, and 90" Bok spectra in black; a white dwarf model atmosphere in blue; a K7 V main sequence model in Red; and the composite model in purple. The optical spectra were taken near orbital superior conjunction making the narrow H and He emission lines from the reflection effect visible.

Figure 1.2 highlights the contribution the reflection effect has to the spectrum of HS1136+6646. The reflection effect, the white dwarf and the K7 all have similar flux equally contributing to the overall spectra in the red. It is interesting to note that the reflection effect emanating from the illuminated face of the K7 star has a larger overall contribution to the observed flux than the K7 star alone.

1.3.3 Current List of Known Post-Common Envelope Binaries

The number of known post-common envelope binaries is modest; approximately 28 are listed by Schreiber and Gänsicke (2003) in their review of these systems (see Table 1.1). As can be seen, HS1136 is among those having the hottest primary (ie. it is one of the youngest and most recently evolved systems of the type). In addition

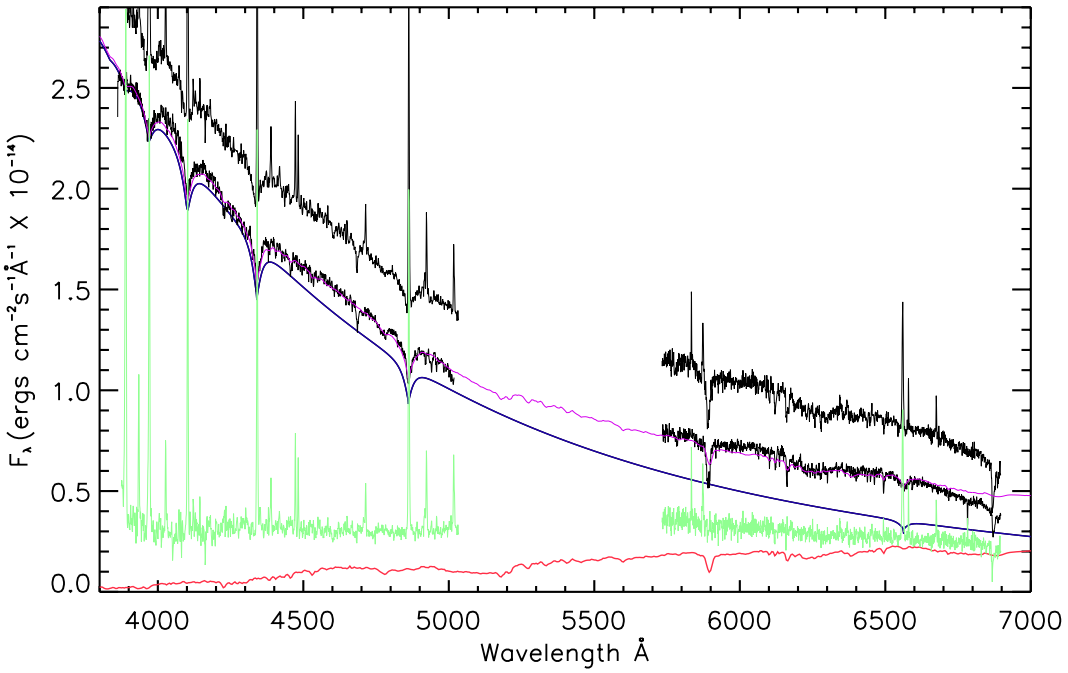

Figure 1.2: The optical spectral energy distribution of HS1136+6646. Plotted is the 90" red and blue spectra for superior and inferior conjuction in black; a white dwarf model atmosphere in blue; a K7 V main sequence model in Red; and the composite model in purple. The green spectrum is the difference between the spectra at superior and inferior conjuntion, indicating the contribution from the reflection effect.

to being one of the most extreme post-CE systems, HS1136+6646 is also one of the brightest, making it a relatively easy object to study from either the ground or from space. In effect, many observations are possible for HS1136+6646 which would be difficult if not impossible for many of the other systems listed in Table 1.1.

1.4 History of Pre-Cataclysmic Variable HS1136+6646

The DAO star HS1136+6646 was first discovered by Heber et al. (1996) during follow-up spectroscopy of stellar sources from the Hamburg-Schmidt objective prism survey. The authors classified HS1136+6646 as a binary star consisting of a hot DAO (He II λ4686 Å in absorption) with a late K companion. No emission lines were seen in the 1993 March 11, 1:14 UT spectrum (Heber private communication), despite the fact that our ephemeris (see Table 1.2) places the phase at 0.64±0.1, when the emission lines should be visible. A combination of significantly lower spectral resolution along with the fact that all of the strongest emission lines observed between 4000 Å and 7000 Å are located the cores of the white dwarf's broad photospheric absorption lines, could be a possible reason for the lack of emission lines seen. Moreover, the Heber spectra do not extend shortward of 4000 Å where some of the strongest emission lines are observed. Although the spectral type of the secondary was determined to be that of a K7 (Heber et al., 1996), the mass determined in this work points towards that of a lower mass M2.5 secondary star. Throughout the dissertation I refer to the secondary star as a K7 when discussing spectral characteristics and M2.5 when discussing its mass. The reason for the discrepancy between spectral type and mass will be discussed later.

The coordinates of HS1136+6646, derived from the STScI Digital Sky Survey plates, are included in Table 1.2 along with a finding chart in Figure 1.3. Estimates of proper motion derived from the USNO-B1.0 catalog (Monet et al., 2003) indicate a small proper motion of 0.065" yr^{-1} at a position angle of 248°.

We first observed HS1136+6646 on 2001 March 15 at the Steward Observatory 2.4m telescope as part of a spectroscopic survey of DAO and H-rich planetary neb-

Table 1.1: Well Studied Post-Common Envelope Binaries. The top portion of the list contains pre-cataclysmic variable binaries.

Object	Primary Spec.Type	P_{orb} days	M1 $M_\odot$	M2 $M_\odot$	R2 $R_\odot$	T_{eff} K
PG 1017-086	sdB	0.073	0.5±0.1	0.078±0.0055	0.085±0.04	30,300
HS 0705+6700	sdB	0.096	0.483±0.005	0.134±0.005	0.186	28,800
NY Vir	sdB	0.101	0.5±0.1	0.15±0.05	0.205±0.01	33,000±3000
HR Cam	WD	0.103	0.41±0.01	0.096±0.004	0.125±0.020	19,000
MT Ser	sdO,PN	0.113	0.6±0.1	0.2±0.1	0.2±0.1	50,000
HW Vir	sdB	0.117	0.48±0.09	0.14±0.02	0.180±0.011	28,488±208
NN Ser	WD	0.13	0.57±0.04	0.12±0.03	0.166	55,000±8000
EC 13471-1258	WD	0.151	0.77±0.04	0.58±0.05	0.42	14,085±100
MS Peg	WD	0.174	0.487±0.002	0.227±0.002	0.27±0.02	22,170
BPM 71214	WD	0.201	0.77±0.06	0.4±0.05	0.38	17,200±1000
LM Com	WD	0.259	0.457±0.05	0.28±0.05	0.296	29,300
AA Dor	sdO	0.262	0.33±0.003	0.066±0.001	0.10±0.01	42,000±1000
CC Cet	WD	0.284	0.39±0.1	0.18±0.05	0.21±0.02	26,200±2000
RR Cae	WD	0.304	0.467±0.005	0.095±0.005	0.189	7,000
BPM 6502	WD	0.337	0.5±0.05	0.16±0.09	0.204	20,640±200
GK Vir	WD	0.344	0.51±0.04	0.1±0.05	0.15	48,800±1200
KV Vel	sdO,PN	0.357	0.63±0.03	0.25±0.06	0.402±0.005	77,000±3000
UU Sge	sdO,PN	0.465	0.63±0.06	0.29±0.03	0.53±0.02	87,000±13000
V477 Lyr	sdOB,PN	0.472	0.51±0.07	0.15±0.02	0.46±0.03	60,000
V471 Tau	WD	0.521	0.84±0.05	0.93±0.07	0.98±0.10	34,500±1000
HZ 9	WD	0.564	0.51±0.1	0.28±0.04	0.296	20,000±2000
UZ Sex	WD	0.597	0.65±0.23	0.22±0.05	0.25±0.03	17,600±2000
EG UMa	WD	0.668	0.64±0.03	0.42±0.04	0.4	13,125±125
RE 2013+400	WD	0.706	0.56±0.03	0.18±0.04	0.221	49,000±700
RE 1016-053	WD	0.789	0.6±0.02	0.15±0.02	0.195	55,000±1000
HS 1136+6646	**WD**	**0.83607**	**0.85±0.02**	**0.37±0.02**	**0.6**	**110,000**
IN CMa	WD	1.26	0.57±0.02	0.39±0.07	0.375	53,000±1100
BE UMa	sdO,PN	2.291	0.7±0.07	0.36±0.07	0.72±0.05	105,000±5000
Feige 34	WD+WD	0.5325	0.5	0.42		
V664 Cas	sdO,PN	0.5817	0.57±0.03	1.09±0.07	1.3±0.8	83,000±6000
VW Pix		0.6758				
HD 49798	NS	1.5477	1.75±1	1.75		
HD 33959C		3.75	1	1.8		
Feige 24	WD	4.2316	0.47±0.02	0.295±0.035		65,290±1553
V651 Mon		15.991	0.4±0.05	1.8±0.3		100,000

References: Schreiber and Gänsicke (2003), Ritter (1986) and references therein.

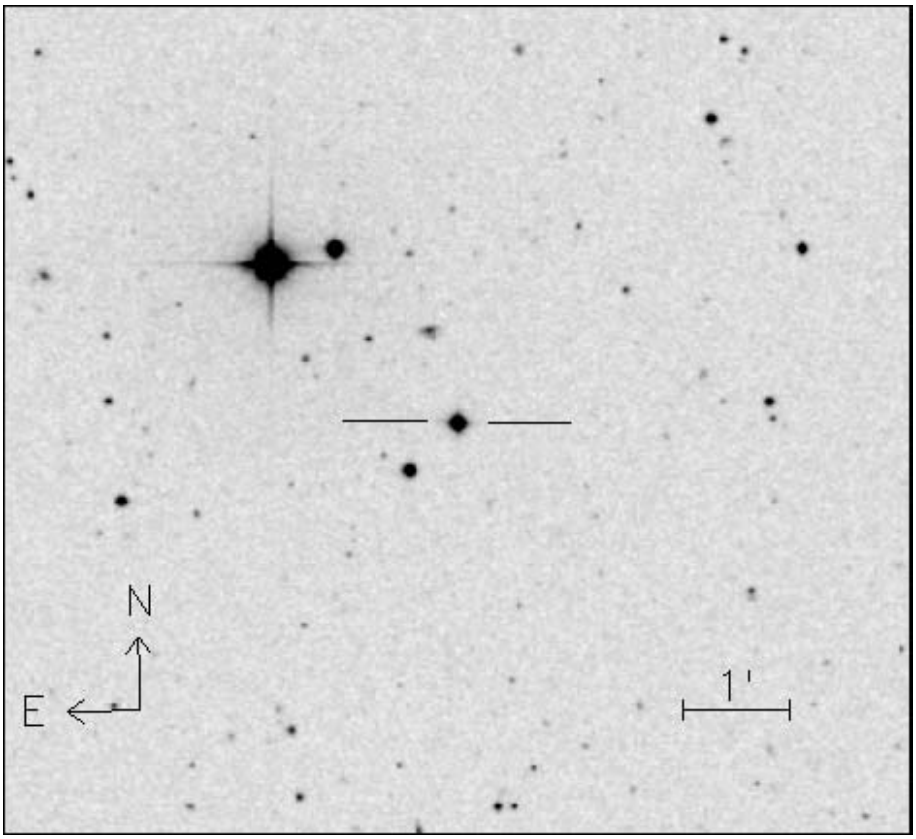

Figure 1.3: Digital Sky Survey finding chart (POSS II, blue) for HS1136+6646

Table 1.2: HS1136+6646 System Parameters

Parameter	Value	Note
Primary Star	DAO White Dwarf	
Secondary Star	M2.5	Mass
	K7	Spectral Type
RA(2000)	11:39:05.98	
DEC(2000)	+66:30:17.98	
Radial Velocity Ephemeris	T_0 = HJD2452360.566+0.83607E	
V magnitude	13.63 ±0.03	
J magnitude	12.314±0.021	
H magnitude	11.695±0.024	
K magnitude	11.543±0.021	
V_{dK}	15.46 ±0.04	Inferior Conjunct. est.
V_{WD}	13.85±0.03	
V-band Photometric semi-Amp.	0.11 mag. (Orbital)	
V-band Photometric semi-Amp.	0.0093 mag. (Rotational)	
White Dwarf T_{eff}	70,000 K	Balmer line fits
White Dwarf T_{eff}	120,000 K	Lyman line fits
White Dwarf surface gravity	log g = 8.29 (calculated)	cgs units
Low-Amp. Photometric Period	234.156 min.	
K_{WD} Velocity	55.4 ± 0.3 km s^{-1}	
K_{MS} Velocity	130 ± 7 km s^{-1}	
γ system	-20.9 ±1 km s^{-1}	
γ'	27.5 ± 0.5 km s^{-1}	WD system vel.
v_g	48.8 ± 1.5 km s^{-1}	Grav. Redshift
M_{MS}	0.37 ± 0.02 $M_\odot$	M star mass
M_{WD}	0.85 ± 0.02 $M_\odot$	WD mass
R_{MS}	0.68 $R_\odot$	M star radius est.
R_{WD}	0.011 $R_\odot$	WD radius est.
a	3.99±0.02 $R_\odot$	Orbital Separation
Estimated Distance	388^{+100}_{-50} pc	

ulae central stars. At that time its spectrum was dramatically different from that published by Heber et al. (1996). Strong emission lines due to H I, He II, Ca II, and Mg II were observed. Follow-up observations, on 2001 May 5 through 6, 2002 March 26 through 29, and 2003 March 21 through 23 showed a large amplitude orbital motion between the emission lines and the He II λ4686 photospheric absorption line, due to the white dwarf, as expected in a double-line spectroscopic binary. Discussion of these initial observations are contained in Holberg et al. (2001) and Sing et al. (2003).

1.5 History of Cataclysmic Variable V405 Aurigae

V405 Aurigae was discovered in the ROSAT all-sky survey by Haberl et al. (1994) and classified as an intermediate polar (IP). Follow up X-ray observations and optical spectroscopy revealed the binary to have a 4.15 hour orbital period and a 545.455 sec WD spin period (Table 1). V405 Aur along with PQ Gem, RXJ0512, and RXJ0757 (James et al. 2002; Burwitz et al. 1996; Kemp et al. 2002 respectively) form a particular subclass of IPs which are likely to soon become polars as they evolve. Evolutionary models show that these four binary systems have likely only recently become CVs and will probably become short period AM Her type stars within $\sim$1 Gyr. (Howell et al., 2001). This group displays properties common to both IPs and polars. In common with IPs this group displays: (1) a white dwarf spin period much shorter than the orbital period, (2) a strong, spin modulated X-ray pulsation, and, (3) a synodic beat period seen in optical observations. The group's polar properties include: (1) spin modulated polarization, (2) red flux variations modulated on the rotation period, (3) a luminous cyclotron component indicative of stronger than normal IP magnetic field strengths, (4) a strong soft X-ray/EUV component similar to many high field strength polars, and (5) narrow X-ray dips, suggesting a highly magnetically collimated geometry of the in-falling accretion material. The study of these few objects will ultimately provide many key insights into the accretion dynamics, magnetic field distribution on the WD surface, and evolutionary aspects

Table 1.3: V405 Aur System Parameters

Parameter	Value	Ref.
Orbital Period	4.15 hours	1
WD Spin Period	545.4565(8) sec	2
Estimated Distance	300-310 pc	1
Estimated Magnetic Field Strength	> 5 MG	3
Radial velocity ephemeris T_0	HJD 2,451,088.76164+0.1726196E	4
Zero phase difference ϕ	-0.01±0.07	5
Inclination	< 5 degrees	5
γ velocity	+41.1±0.1 km s^{-1}	5
K_{WD} Velocity	2.5± 0.5 km s^{-1}	5

(1)Haberl et al. (1994); (2)Allan et al. (1996); (3)Haberl and Motch (1995); (4)Szkody et al. (2000); (5)Sing et al. (2004b)

of magnetic CVs.

1.6 Discovery of a Bright New Eclipsing Cataclysmic Variable J0604+3344

I present discovery observations of a new bright nova-like cataclysmic variable (CV), NSVS07178256. This star was initially discovered as a large amplitude eclipsing variable in the ROTSE survey(Median Unfiltered ROTSE Mag = 13.392, Wozniak 2004; RA: 06:44:34.637, DEC: +33:44:56.615; J2000, hereafter J0644+3344). We (Sing D. K., Green E. M., Lopez-Morales M., Shaw J. S., and Howell S. B.) have identified this system as a variable star while conducting an extensive search campaign for short period eclipsing binaries among objects in the Northern Sky Variability Survey (NSVS, Woźniak et al. 2004) photometry database.

The NSVS database was searched for periodicities by simultaneously using the String-Length (Clarke, 2002) and Analysis of Variance (Schwarzenberg-Czerny, 1989) methods. J0644+3344 revealed itself as a possible candidate having strong photometric variations exceeding one magnitude, interpreted as brief periodic eclipses occurring with a period of 0.538669 days.

There are no previous references to this binary in the literature. The only initial estimation that we had of its apparent magnitude was the I-band value provided by the NSVS ($I_{NSVS} \sim 13.4$). A more careful search on this object revealed that it can

be identified with the ROSAT All Sky Survey source 1RXS J064434.5+334451. The object also appears in the 2MASS catalog as object 2MASS J06443435+3344566 (J=12.493 ± 0.023; H=12.163 ± 0.026; Ks=12.03 ± 0.022). The J-Ks, J-H, and H-Ks colors from 2MASS (J-Ks=0.463 ± 0.032; J-H=0.330 ± 0.035, and H-Ks = 0.133 ± 0.034) provide the first clues about the nature of this binary. From the UCAC2 catalog (Zacharias et al., 2004), we find that J0644+3344 has a small proper motion (μ_a= -5 ± 4.3; μ_d= -3.3 ± 1.7 mas yr^{-1})

Its H-Ks color is consistent with the system being a low-mass eclipsing binary, however its J-H color is too blue (J-H > 0.5 for low-mass stars). Placing this binary in the (J-H) vs (H-Ks) diagrams for CVs (Hoard et al., 2002) suggests that J0644+3344 could be a nova-like CV. However, the system could also be an eclipsing hot subdwarf (sdB), based on the its location in the (J-Ks) vs (J-H) diagram of Stark (2005).

We obtained followup photometric and spectroscopic observations of J0644+3344 in an attempt to identify the binary system as well as determine its orbital period. The study of eclipsing cataclysmic variables, such as J0604+3344 offers the opportunity to study the complex structure of the accretion disk components and stellar components through eclipse profiling. The presence of an eclipse also places strict limits on the inclination of the orbit, thereby further constraining the stellar masses.

1.7 Common-Envelope Theory

1.7.1 Classical α Theory

The standard formalism describing the common-envelope phase was developed by Paczynski (1976) to explain the existence of short period binaries. It was recognized that in binary systems, the initial orbital separation would had to have been much larger than the observed final close white dwarf+main sequence binary separation. This would allow the primary star sufficient orbital separation space to evolve into a red giant and to form the white dwarf. Paczynski (1976) conceived a mechanism to decrease the orbital separation by assuming angular momentum conservation

during the common-envelope phase. In this scenario, the orbital energy of the binary system is used to eject the primary star's expanding envelope. Qualitatively, this is accomplished by the binary system experiencing a drag force as it orbits in the low density medium of the envelope, causing the orbital separation to decrease. During the CE phase, it is assumed that the decrease in separation halts when the loss in orbital energy equals the binding energy of the envelope with an efficiency α (Webbink, 1984),

$$\frac{GM_gM_e}{R_g} = \alpha\lambda\left[\frac{GM_cM_{MS}}{2a_f} - \frac{GM_gM_{MS}}{2a_i}\right], \tag{1.1}$$

where G is the gravitational constant, a is the separation, and the subscripts g, e, c, MS, i, f stand for giant, envelope, core, secondary main sequence, initial and final respectively. The dimensionless number λ is a parameter characterizing the envelope structure and is normally taken as a constant. The relative change in separation is then given by,

$$\frac{a_f}{a_i} = \frac{M_c}{M_g}\left[1 + \frac{2M_ea_i}{\alpha\lambda R_gM_{MS}}\right]^{-1}, \tag{1.2}$$

where it is assumed the radius of the giant R_g equals the Roche lobe at the start of the CE process, and that the secondary does not accrete matter during the CE phase. Typical values of the product $\alpha\lambda$ are around 1.

1.7.2 Alternative γ Theory

In addition to the classical α theory of common-envelope (CE) evolution, a second alternative formalism has been recently developed by Nelemans et al. (2000) to explain the evolution of double-degenerate binaries. Nelemans et al. used the core mass-radius relation for giants with degenerate helium cores to reconstruct the evolution of double degenerate helium core white dwarf binaries. With this relation, an initial separation and mass could be estimated. These are the crucial observationally elusive parameters needed to test CE theory. The authors found that the standard α CE theory was insufficient, and suggested an alternative, first suggested by Paczyński and Ziółkowski (1967). In this theory energy, rather than angular

momentum, is assumed to be conserved. Mass loss from the primary stars envelope reduces the system angular momentum, J, of the binary system given by,

$$\frac{\Delta J}{J} = \gamma \frac{M_e}{M_g + M_{MS}}, \tag{1.3}$$

with γ a dimensionless parameter characterizing the efficiency of the process. The change in separation is then given by,

$$\frac{a_f}{a_i} = \left[\frac{M_g}{M_c}\right]^2 \frac{M_c + M_{MS}}{M_g + M_{MS}} \left[1 - \gamma \frac{M_e}{M_g + M_{MS}}\right]^2. \tag{1.4}$$

Nelemans and Tout (2005) found good agreement in values of γ around 1.5 when reconstructing 19 known double degenerate binaries.

1.8 Type Ia Supernova Progenitors and the Common-Envelope Process

1.8.1 Importance for Dark Energy

Recent observations of distant type Ia supernova have revealed the presence of dark energy (Schmidt et al. 1998; Perlmutter et al. 1999). Type Ia supernova are viewed as precise distance indicators, as they are believed to be standard candles, and are thought to result from a thermonuclear detonation of a carbon-oxygen white dwarf at the Chandrasekhar mass limit. These supernovae, viewed at the highest redshift (ie. farthest distance), are observed to be dimmer than originally expected, meaning they are at a greater distance. This result has led to the conclusion that the universe must be accelerating in its expansion, a phenomena now attributed to dark energy. There are currently complementary results to the supernova data from cosmic microwave background surveys (Tegmark et al., 2004) and large scale structure (called the integrated Sachs-Wolfe effect Boughn and Crittenden 2004), providing further support for the existence of dark energy. Type Ia supernova, however, are still the only *direct* observational evidence for dark energy, as well as the most potentially sensitive probe as to its behavior (Leibundgut, 2001). Example of the progenitors of Type Ia supernova are uncertain, and the astronomy community relies on empirical corrections (Riess et al., 1996) to the light curves of supernova

when determining the distance to these events. Given the cosmological importance of Type Ia supernova on dark energy, it is worth reviewing the candidate binary progenitors of Type Ia supernova and the important role the common-envelope process plays.

1.8.2 Evolutionary Scenarios for Type Ia Supernova Progenitors

There are two main Type Ia supernova formation channels within standard stellar evolutionary theory, binaries containing one white dwarf and those with two (see Belczynski et al. 2005 and Figure 1.4). For close-binary systems, the evolutionary scenarios diverge after the first common-envelope (CE) phase. For those binaries which will ultimately undergo one CE phase, after a detached post-CE phase, further interaction is possible with stable mass transfer from the donor secondary star. The binary pair becomes a soft X-ray source due to accretion on the WD. The WD can then produce a supernova if a sufficient amount of mass accumulates. This is the first Single Degenerate Scenario (SDS).

In the Double Degenerate Merger (DDM) scenario, a second CE phase, due to the secondary star, creates a WD+WD pair. If both WDs have CO cores, they will eventually merge due to the loss of angular momentum from emission of gravitational waves. If the system has a total mass exceeding the Chandrasekhar limit, the merger creates a Type Ia supernova. If the secondary star creates a WD with a He core, stable mass transfer of degenerate He matter onto the CO WD creates an AM CVn type system. These He accreting binaries can detonate at a sub-Chandrasekhar limit (called edge-lit detonation, Livne 1990) due to He layer ignition causing a CO detonation.

In another SDS, a second CE phase takes place if the secondary star does not have a degenerate core, like the double degenerate cases, but rather contains a nondegenarate He core. The WD + He star or subdwarf B binary pair can later start He accretion, becoming an AM CVn binary. As with the double degenerate case, the WD can detonate at a sub-Chandrasekhar mass, although such scenarios are highly controversial.

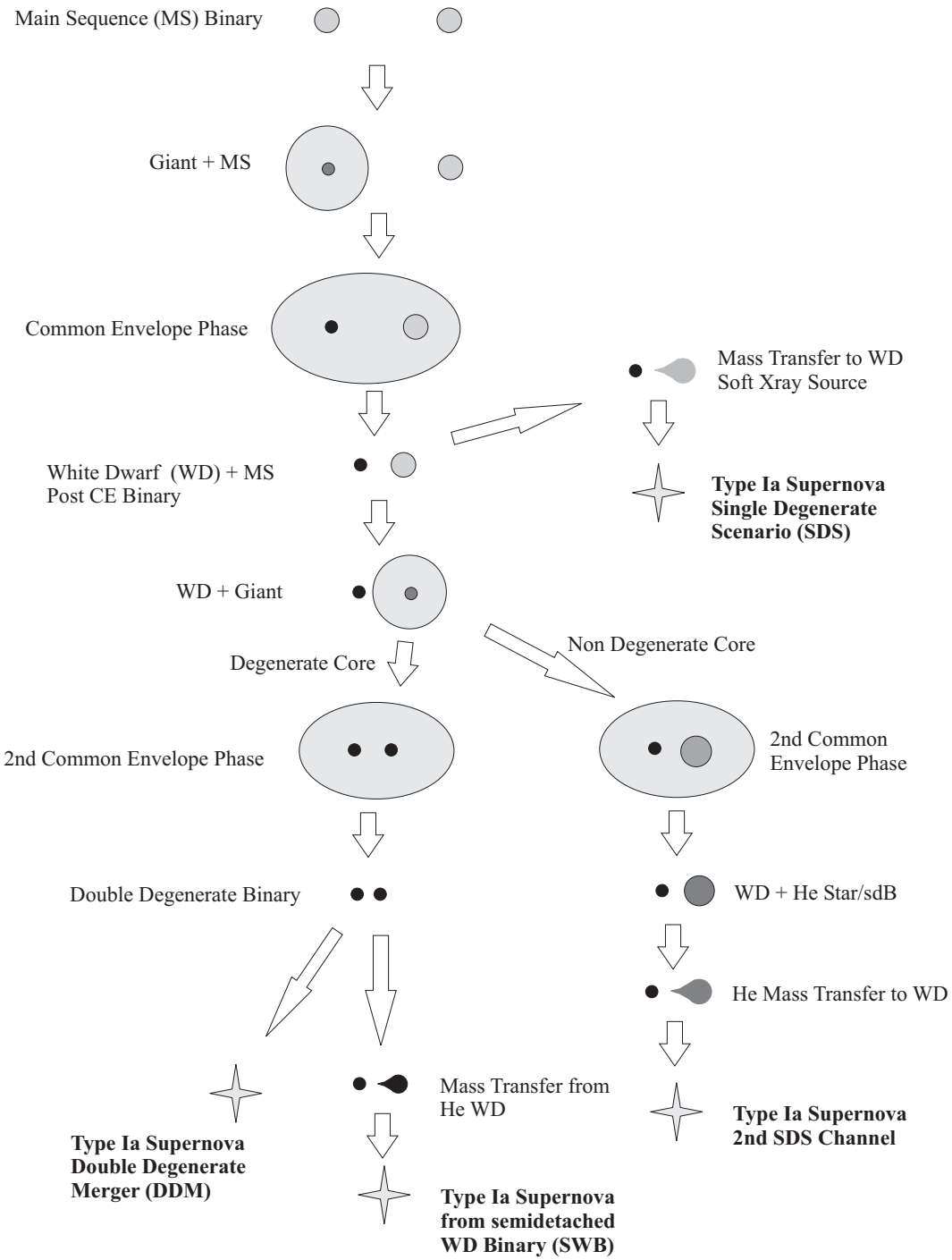

Figure 1.4: Evolutionary Scenarios for close-binary systems resulting in Type Ia supernova. Based on Belczynski et al. (2005) and Solheim and Yungelson (2005).

1.8.3 Effect of the Common-Envelope

Recent studies trying to determine Type Ia progenitors have focused on the delay time between star formation and supernova explosion. By looking at supernova up to z=1.6 and assuming a star formation rate, Strolger et al. (2004) found the average delay time 2.4-3.8 Gyr, using a Gaussian to describe the delay time distribution. This distribution can be compared to Type Ia progenitors population synthesis codes like Belczynski et al. (2005), who compared theoretical delay times with the results of Strolger et al. (2004). These results are highly dependent on which CE prescription is used, and what values for the input parameters are chosen. Belczynski et al. (2005) found the observed delay times matched DDM scenario with both the α and γ CE prescription, while the delay times matched the SDS when one tuned the CE parameters. Given the lack of theoretical understanding of the CE process, it appears an empirical fit to post-CE binaries will be needed to properly constrain the current CE models and thus Type Ia progenitors.

1.9 Structure of Thesis

In this dissertation I present observations and analysis of two post-common envelope systems. The first is an extensive study of HS1136+6646, a pre-cataclysmic variable while the other, an analysis of the Far UV spectra of V405 Aurigae, an intermediate polar cataclysmic variable. I also report on the discovery of a new bright eclipsing cataclysmic variable.

In the first five chapters, I present a complete description of the existing ground-based and space based ultraviolet data of the pre-cataclysmic variable HS1136+6646. This includes the ground and spaced based spectroscopic data in Chapter 2 and ground based photometric data in Chapter 3. In Chapter 4, I provide an analysis consisting of the data described in the previous two chapters, determining all of the binary parameters. Discussion of the analysis is included in Chapter 5, including the complete past and future history of HS1136+6646, a comparison to other similar binary star systems, and a reconstruction of the common-envelope efficiency.

Chapter 6 contains the observations and analysis for the cataclysmic variables V405 Aurigae and the discovery of J0604+3344, a bright eclipsing cataclysmic variable. The results from the analysis of V405 Aurigae are also contained in Chapter 6, while Chapter 7 contains the conclusions. Two appendices are included. The first, appendix A, I present a derivation of the angular momentum loss in a binary system from gravitational waves. In the second appendix, B, I review the mechanism of angular momentum loss due to magnetic breaking.

CHAPTER 2

Spectroscopic Observations of HS1136+6646

2.1 Far Ultraviolet Spectroscopic Explorer

2.1.1 *FUSE* Instrument Layout

The *Far Ultraviolet Spectroscopic Explorer* (*FUSE*) was launched into space on 1999 June 24 to conduct high sensitivity, high spectral resolution ($\Delta\lambda/\lambda \sim 20,000$) observations between the Lyman limit at 912 Å and Lyman α at 1216 Å. The *FUSE* spacecraft uses four separate off-axis mirrors, two made of LiF and two made of SiC. These mirrors, each 387×352 mm, reflect light along four separate optical paths, called channels, to a Rowland circle based spectrometer (see Figure 2.1 and Oegerle et al. 2000). Two of the diffraction gratings are coated with SiC while the other two have an Al+LiF coating. This configuration maximizes the throughput of the instrument, resulting in a total wavelength range from 907 Å to 1187 Å. The spectroscopic data is recorded by two microchannel plate (MCP) double-delay inline detectors with the surfaces curved to match the Rowland circle. The MCPs amplify photoelectrons from a potassium bromide photocathode, resulting in a cloud of electron called a photon event. The analog signal of these photon events are then digitized, with the spectral directions determined by the propagation time of the electron cloud. This detection technique allows an approximate arrival time of each photon event to be recorded, called Time Tagged mode (TTG). A second mode called histogram mode returns an integrated spectra having no time resolution. A resulting *FUSE* spectrum thus consists of eight (four channels times two sides) separate spectra, which partially span the 900 Å to 1180 Å band with overlapping coverage. These component spectra can be studied individually or combined and coadded into a single spectrum.

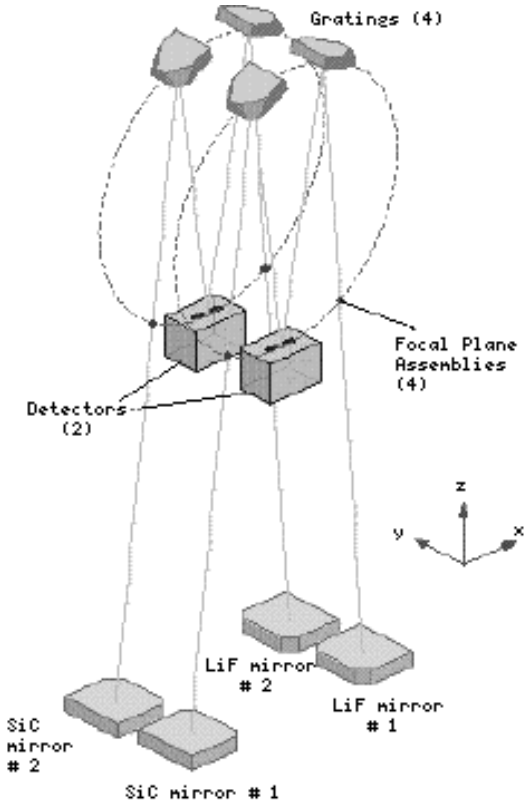

Figure 2.1: FUSE optical design showing the four separate optical paths. Figure from the *FUSE* Instrument and Data Handbook (Oegerle et al., 2000).

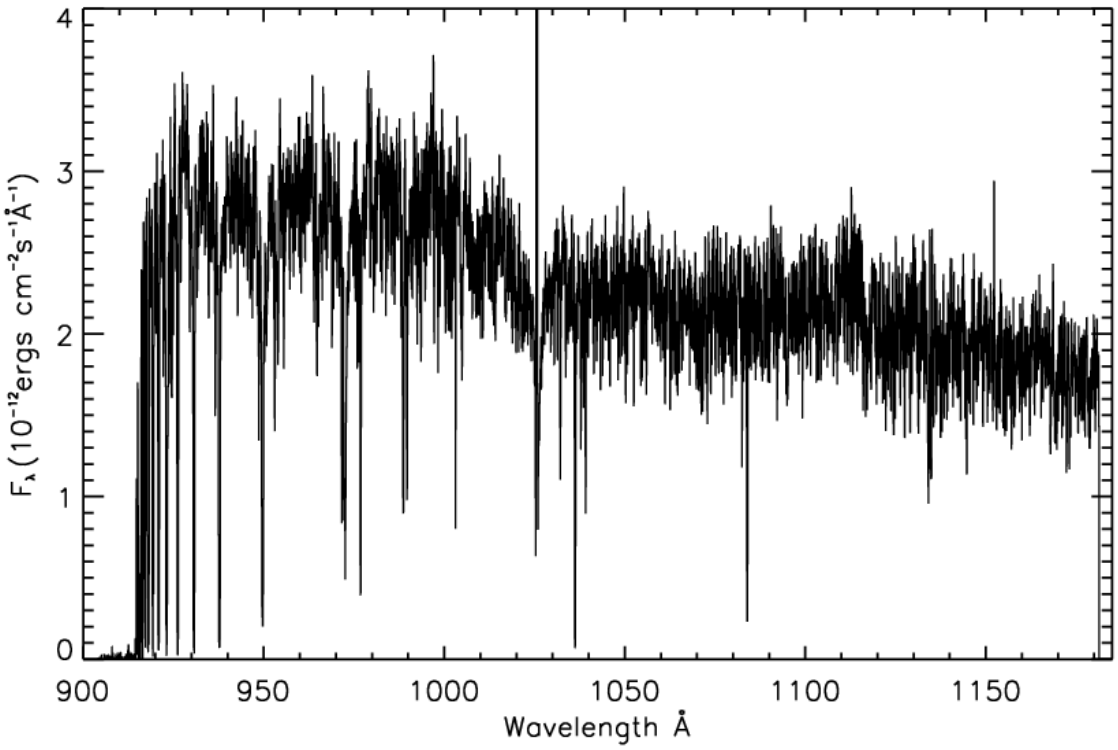

Figure 2.2: A sample exposure of the 2003 observations showing the *FUSE* spectrum of HS1136+6646.

2.1.2 *FUSE* Observations Of HS1136+6646

Far UV (900 Å - 1180 Å) spectra of HS1136 were obtained with the *FUSE* satellite (Moos et al., 2000) during 2001 January 12 Cycle 2 (B053080100), 2002 January 29 Cycle 3 (S60106061), and 2003 May 14 Cycle 4 Observations (D0920102). The main goals of the latter observations were to directly study the white dwarf star over an entire orbital period, in order to provide radial velocity data on the white dwarf. All of the observations were obtained through the large (30"×30", LWRS) aperture in Time Tagged (TTG) mode. The 2001 and 2002 data sets are briefly discussed in detail in Sing et al. (2004a) along with a preliminary analysis of the 2003 data. The 2003 observations were taken between JD 2452773.3198 and 2452774.9339 with 18 exposures totaling 78.9 ksec that cover 87% of the total orbital ephemeris.

2.1.3 HS1136+6646 *FUSE* data reduction

Data from the 2001 and 2002 observations were reduced using the most recent available version of the *FUSE* data reduction software (CalFUSE v2.4). In short, the CalFUSE data reduction pipeline takes the raw spectroscopic data, corrects for spacecraft motion, removes cosmic rays, flatfields the spectra, applies a wavelength calibration, and finally flux calibrates the spectra. Extracted spectra from each of the four instrumental channels (separate optical paths consisting of different combinations of mirrors and gratings) and the two instrumental sides (independent microchannel plate detectors) were extracted. The resulting eight spectra were combined into a single continuous spectrum as follows. First, the spectra were compared and scaled in flux to match the observed flux in the LiF1 channel over the 1050 Å to 1070 Å range, since this wavelength region is common to all four channels. Second, the spectra were re-sampled onto a common uniform wavelength scale with increments of 0.05 Å, which approximate the instrumental spectra resolution. Mutual alignment of the component spectra was achieved with respect to interstellar absorptions features. Third, for each exposure, a single composite spectrum was produced by a coaddition process that weighted the fluxes with respect to the S/N in each spectral region. Photospheric features in the spectra corresponding to each exposure were measured and apparent stellar velocities relative to the ISM velocity were obtained. A final aggregate spectrum was also produced by Doppler shifting each of the exposures into the laboratory velocity frame using its measured relative stellar velocity. This aggregate spectrum, which has an S/N $\sim$ 50 near 1000 Å, is shown in Figure 2.3.

Data from the extensive 2003 observations were processed using the *FUSE* data-reduction software (CalFUSE v2.4.1 and 3.0.6). Extracted spectra from each of the four instrumental channels were extracted. In order to separately analyze spectral variations on the WD spin and orbital period, we re-extracted the 2003 TTG spectra as a function of the 113.13 minute low-amplitude photometric period (Sing et al., 2004a) using the following method. Note, in the initial analysis of HS1136+6646

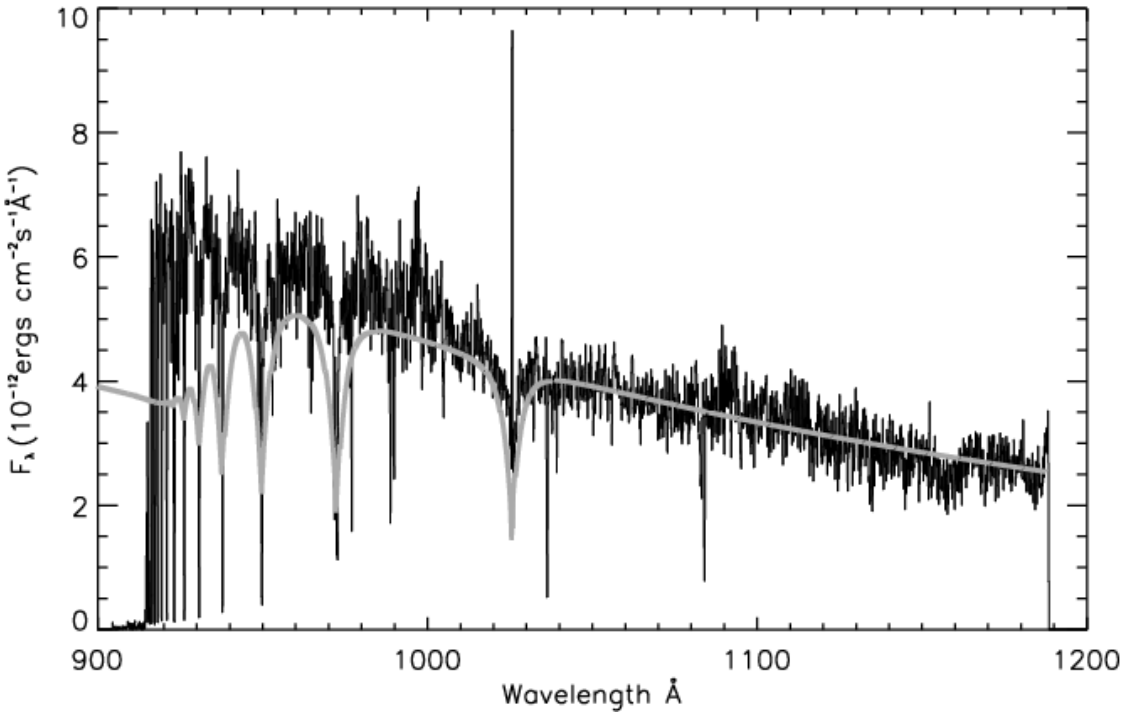

Figure 2.3: *FUSE* spectrum of HS1136+6646 along with a T_{eff}=110,000 K Log g=7.0 model. Note the strong continuum that continues up to the Lyman limit without any roll-off.

(Sing et al. 2004) the low-amplitude photometric period was determined to be 113.13 minutes, while this work concludes the modulation is in fact double peaked, with a period of 234 min (see §4.2.2). First, the headers in the screen parameter FITS files, used by CalFUSE for time extraction in TTG spectra, were edited to extract only the data from the desired phase interval, spin phase 0.0 to 0.1 for example. The keywords GTIBEG01 and GTIEND01 specify the first phase interval, defined in seconds from the start of the first observation. Subsequent numbered GTIBEG and GTIEND headers specify the next interval pairs while the total number of interval pairs is specified by NUSERGTI. Second, the CalFUSE command ttag_combine was then run for all of the raw data in one of the detector segments. Third, the output of ttag_combine was then calibrated with the command cal_fuse_exp_ttag.csh, which only extracts data from the desired phase interval. The above procedure was then repeated for the remaining detector segments (1a, 1b, 2a, and 2b). For HS1136, we extracted 678.87 second (0.0094 orbital phase or 0.1 spin phase) intervals individually such that radial velocity corrections for the WD could be applied before the intervals were combined on the spin phase.

The most striking feature of the HS1136 *FUSE* spectra is the clear presence of the O VI $\lambda\lambda$1032, 1036 resonance doublet (see Fig 2.4). Barstow et al. (2001) determined that temperatures in excess of 56,000 K are required to produce observable O VI lines in DA stars having non-stratified atmospheres.

Table 2.1: Log of Spectroscopic Observations

Date	MJD Start	MJD END	Telescope	Spec. Range	Number Obs.
2001 Jan. 12	1921.85486	1921.96217	*FUSE*	FUV	2
2001 Mar. 15	1984.91318	1984.92952	Bok	Blue	2†
2001 May. 05	2035.65081	2035.94868	Bok	Blue	18*
2001 May. 06	2036.63678	2036.84621	Bok	Blue	18*
2001 Dec. 20	2264.85638	2264.93835	Bok	Blue	5
2001 Dec. 21	2265.99446	2266.00834	Bok	Blue	1
2002 Jan. 03	2277.82778	2277.84861	Mayall	Red	1
2002 Jan. 04	2278.83333	2279.01389	Mayall	Red	4
2002 Jan. 29	2303.64792	2303.73803	*FUSE*	FUV	2
2002 Mar. 26	2360.63557	2360.99945	Bok	Blue	14†
2002 Mar. 27	2361.65752	2361.98831	Bok	Blue	14†
2002 Mar. 28	2362.69017	2362.98201	Bok	Blue	11†
2002 Mar. 29	2363.62567	2363.96778	Bok	Blue	18†
2002 Dec. 18	2627.80817	2628.05427	Bok	Red	13†
2003 Mar. 21	2720.62975	2721.01248	Bok	Blue	16†
2003 Mar. 22	2721.61615	2722.00100	Bok	Blue	18†
2003 Mar. 23	2722.63475	2723.00905	Bok	Blue	19†
2003 May. 14	2773.31983	2774.93389	*FUSE*	FUV	18

*1000 second exposure times

†1200 second exposure times

Bok: Steward Observatory 2.3m telescope at Kitt Peak.

Mayall: NOAO 4m telescope on Kitt Peak.

FUSE: Far Ultraviolet Spectroscopic Explorer.

MJD=JD-2450000;

Blue: 3880 - 5040 Å;

Red: 5733 - 6896 Å

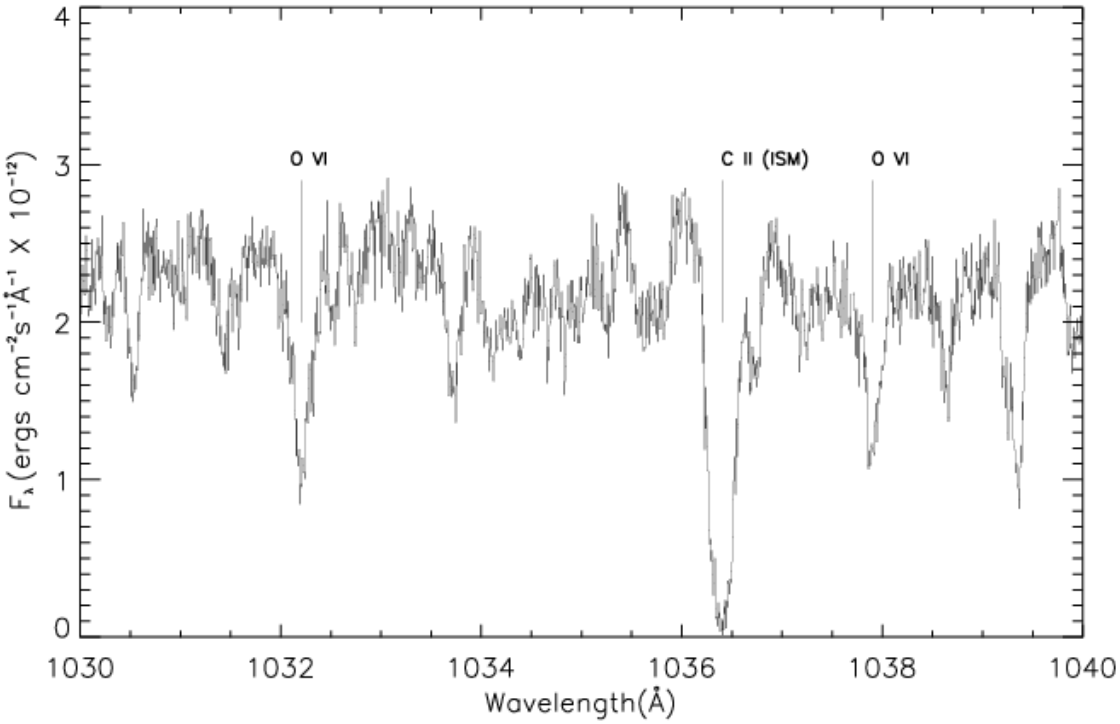

Figure 2.4: A portion of the 2002 *FUSE* spectrum of HS1136+6646 showing the O VI stellar lines along with a C II interstellar line.

2.2 Hubble Space Telescope

2.2.1 *STIS* Instrument Layout

The *Space Telescope Imaging Spectrograph* (*STIS*) instrument on-board the 2.4 meter *Hubble Space Telescope* (*HST*) has a total of three instrumental modes, one imaging detector and two spectrographs (see Mobasher 2002, and Figure 2.5). The imager is a Scientific Image Technologies imaging CCD, called the *STIS/CCD*. It has 0.05 arcsecond square pixels, covering a nominal 52 x 52 arcsecond square field of view (FOV) and operates from 2000 to 10,300 Å. The two spectrograph detectors cover the near and far ultraviolet wavelength ranges. The near ultraviolet (NUV) spectrograph uses a Cs_2Te Multi-Anode Microchannel Array (MAMA) detector, called the *STIS/NUV-MAMA*. It has 0.024 arcsecond square pixels, a nominal 25 x 25 arcsecond square field of view, and operates from 1600 to 3100 Å using echelle gratings, first order gratings, or a prism. The far ultraviolet (FUV) spectrograph uses a solar-blind CsI MAMA detector, called the *STIS/FUV-MAMA*. It has 0.024 arcsec pixels, a nominal 25 x 25 arc-second square field of view, and operates from 1150 to 1700 Å with first order and echelle gratings. The FUV echelle gratings, used in this work, offers high resolution spectroscopy. The E140M medium resolution grating provides 1/91,700 Å pixel^{-1} dispersion over 600 Å with a central wavelength of 1425 Å. The E140H high resolution grating gives 1/228,000 Å pixel^{-1} dispersion over 210 Å over 50 orders. The spectrometer has several selectable apertures, we used the 0.2×0.2" science aperture for our observations.

2.2.2 *STIS* Observations Of HS1136+6646

We obtained *HST STIS* observations of HS1136+6646 to realize two major scientific goals. The first was to determine the absolute wavelength scale of the *FUSE* observations. Since the *HST* spectra has an absolute wavelength scale, the velocities measured from interstellar medium absorption lines could be used to wavelength shift the *FUSE* spectra, making them match the *HST* velocities and placing the *FUSE* spectra on an absolute wavelength scale as well. This makes it possible to

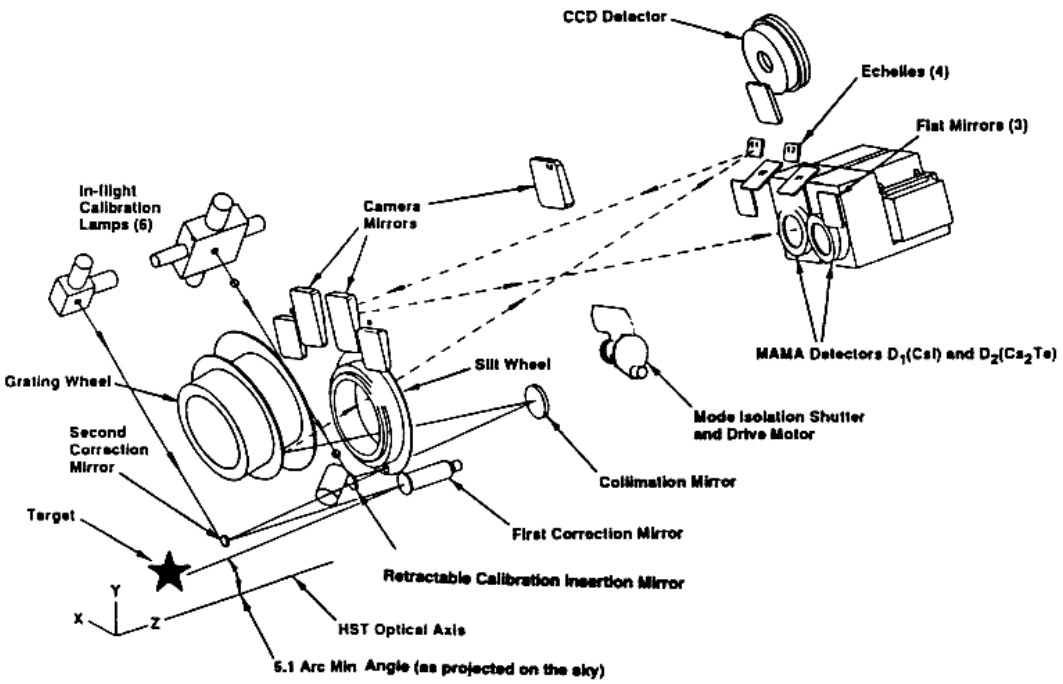

Figure 2.5: *STIS* optical design. Figure from HST instrument handbook (Mobasher, 2002)

use the *FUSE* and *HST* spectra to measure a gravitational redshift and determine the white dwarf's mass. Our second goal was to determine the photospheric heavy element abundance in HS1136+6646 from such species as Fe and Ni. To accomplish these goals, ultraviolet spectra of HS1136+6646 were obtained with the *HST* using the *STIS/FUV-MAMA*) instrument during 2004 February 05 and 2004 February 08 Cycle 12 observations (see Table 2.2). The February 05 observations were obtained with the FUV-MAMA detector using the E140H grating through a 0.2"×0.2" aperture. A prime grating tilt centered at 1234 Å was used, producing a resolving power of 110,000 from 1147-1335 Å. Because HS1136+6646 lies in the *HST* continuous viewing zone near the orbital pole of the spacecraft, continuous long exposures of this star are possible, without earth occultations. A single 4,048 second exposure was taken, occurring near the WD's radial velocity minimum. The 2004 February 08 data were obtained with the FUV-MAMA detector using the E140M grating through a 0.2"×0.2" aperture. The E140M uses a prime tilt at 1425 Å producing a resolving power of 45,800 over a wavelength range of 1123-1710 Å. Three 1400 second exposures were taken when the WD was near radial velocity maximum.

The *STIS* data were processed using the Space Telescope Science Data Analysis System (STSDAS) within the Image Reduction and Analysis Facility (IRAF) software package with the post-reduction analysis done using custom Interactive Data Language (IDL) programs. For each exposure, the extracted echelle orders were concatenated onto a single wavelength solution. The four HST spectra were Doppler shifted into the laboratory velocity frame by using the measured stellar velocity. A single composite spectrum was then produced by using a co-addition process which weighting the flux of each spectra with respect to its S/N (see Figure 2.6). A heliocentric composite spectrum was used for the analysis of the interstellar medium (ISM) absorption lines.

Table 2.2: Log of *HST* STIS Observations

Date	HJD Start	HJD End	Exp. Time
2004 Feb. 05	2453040.843082	2453040.889933	4048 sec
2004 Feb. 08	2453043.730836	2453043.747040	1400 sec
2004 Feb. 08	2453043.748718	2453043.764922	1400 sec
2004 Feb. 08	2453043.767758	2453043.783961	1400 sec

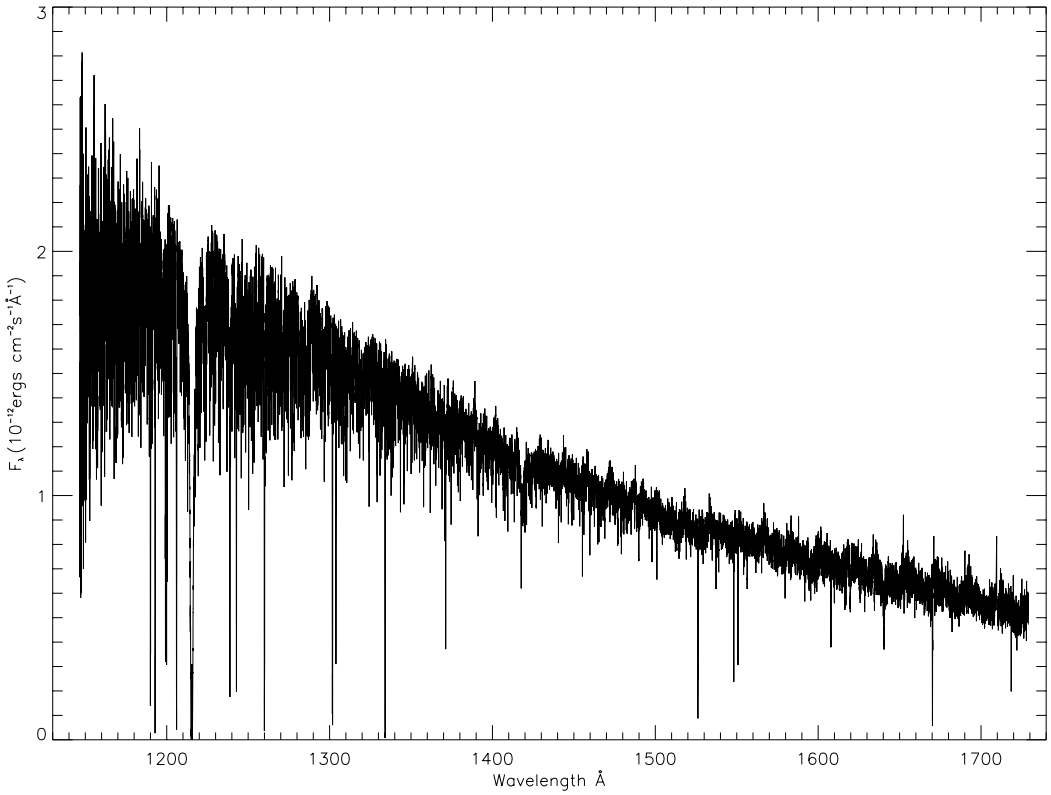

Figure 2.6: Composite *HST* spectrum of HS1136+6646.

2.3 Ground Based Spectroscopy

2.3.1 Bok 90”

Optical spectra of HS1136+6646 were obtained from the Steward Observatory 2.4m Bok telescope, located on Kitt Peak, during three observing runs between 2001 May and 2003 March (see Table 2.1). The spectra were obtained using the Boller and Chivens Spectrograph at the Ritchey-Chretien f/9 focus. A 1200×800 15 μm pixel CCD was used in combination with a 1st order 1200 line/mm grating blazed at 5436 Å to record the blue channel spectra covering a wavelength range of 3880 - 5040 Å. With a 2.5 arcsec slit width, a typical spectral resolution of 3.5 Å was achieved at a reciprocal dispersion of 0.99 Å/pixel on the CCD. Typical exposure times of 1000-1200 seconds yielded characteristic S/N ratios of 50-60. Before each observation, the instrument was rotated to align the slit perpendicular to the horizon, minimizing the effects of atmospheric dispersion.

Standard Image Reduction and Analysis Facility (IRAF) routines were used to reduce the data. The wavelength calibration was established with He-Ar arc-lamp spectra, interpolated between exposures taken before and after each observation, to account for any small wavelength shifts from instrument flexure which occur when the telescope tracks an object. The spectra were flux calibrated using the Massey et al. (1988) spectrophotometric standard Feige 34 observed over a range of zenith angles covering the program stars’ airmass range. HR4550 and HD103095 were used as radial velocity standards.

2.3.2 Mayall 4 Meter

High dispersion measurements of the emission line profiles were obtained on the NOAO 4m Mayall telescope located at KPNO in February 2002 (See Table 2.1). The CCD Echelle Spectrograph instrument was used with a 58.5 groves/mm grating along with the 226-1 226 groves/mm cross dispersal grating having a first order blaze at 6700 Å. The T2KB 2048 × 2048 24 μm CCD recorded the spectra from 4270-7467Å with a typical resolution of 0.16 Å at a reciprocal dispersion of 0.079 Å/pixel.

Exposure times of 1800 seconds produced typical S/N ratios of 20. Standard IRAF routines were used to reduce the data. Th-Ar lamps were used for wavelength calibration and G191-B2B was used as a spectrophotometric standard (Massey et al., 1988). The high resolution spectra obtained with this telescope made it possible to resolve the emission lines emanating from the secondary star.

CHAPTER 3

Photometric Observations of HS1136+646

3.1 SARA

In collaboration with Dr. Terry Oswalt from the Florida Institute of Technology, UBVRI observations were obtained with the SARA 0.9m automated telescope at Kitt Peak in Arizona. Both differential time-series and absolute photometry was obtained between March 2002, June 2002, March 2003, May 2003, 2004 February 06 and June 2004 (see Table 3.1) by both on-site and remote-access observers. Images were collected using an Apogee AP7p camera with a back-illuminated SITe SIA 502AB 512×512 pixel CCD. The pixels are 24 microns square, corresponding to 0.73" at the telescope focal plane. Read noise and gain for the camera are about 12.2 electrons (rms) and 6.1 electrons/ADU, respectively.

Duty cycle times were typically 25-35 seconds for the time-series work, including a readout time of ∼5 seconds. Sky flats, dark and bias exposures were taken every night. All data were calibrated and reduced using standard IRAF routines. Differential magnitudes were obtained using a brighter comparison star in the CCD field of view.

3.2 La Palma

Intensive photometric monitoring of HS1136 was also carried out by two collaborators (Drs. Matt Burleigh & Simon Good from the University of Leicester, UK) over five nights in 2002 February with the 1.0 m Jacobus Kapteyn Telescope (JKT) on La Palma. The JAG-CCD system was used with a SITe2 detector. This device has 2048×2048 24 micron pixels and an image scale of 0.33"/pixel, giving an approximately 10×10 arcminute field of view. Observations were made for up to ~ 9 hours

Table 3.1: Log of Photometric observations

Date	MJD Start	MJD End	Telescope	Bands	No. Frames
March 27, 2002	2360.698148	2361.037407	SARA†	V	723
April 08, 2002	2372.643831	2373.025324	SARA†	V	571
April 17, 2002	2381.877269	2382.016227	SARA†	V	299
May 16-18, 2002	2410.935729	2412.904575	JKT⋆	BVR	12V, 2B&R
May 23, 2002	2417.647118	2417.925058	SARA†	UBVRI	59 V
May 28-31, 2002	2422.870693	2426.912329	JKT⋆	V	42
June 07, 2002	2432.655880	2432.831655	SARA†	UBVRI	48 V
March 21, 2003	2720.624375	2721.019988	SARA†	V	799
March 22, 2003	2721.615058	2722.037674	SARA†	V	756
March 23, 2003	2722.871736	2722.799479	SARA†	V	752
April 08, 2003	2737.84757	2737.93868	OPTIC‡	V	110
May 25, 2003	2784.670671	2784.846204	SARA†	V	492
May 26, 2003	2785.746435	2785.896933	SARA†	V	374
May 27, 2003	2786.665949	2786.870926	SARA†	V	490
Feb. 05, 2004	3040.812986	3041.065336	SARA†	V	700
Feb. 06, 2004	3041.654815	3042.068947	SARA†	V	881
Feb. 08, 2004	3043.635623	3044.067523	SARA†	V	956
Feb. 09, 2004	3044.614618	3045.020116	SARA†	V	876

†SARA: Southeastern Association for Research in Astronomy telescope at Kitt Peak

⋆JKT: Jacobus Kapteyn Telescope at La Palma

‡OPTIC: University of Hawaii 88" telescope at Mauna Kea

Table 3.2: Summary of 2002 February JKT observing run

UT Date	Filter	Exp. time (sec.)	Duration (hrs.)	No. Frames	Conditions
2002 Feb 3/4	V	40	7.0	214	Photometric, seeing 1.3"
2002 Feb 4/5	R	40	4.2	129	Observed through cirrus, seeing 1"
2002 Feb 5/6	B	40	5.8	179	Cirrus. Seeing variable, 1.2" - 4"
2002 Feb 6/7	B	40	8.8	270	Not photometric. Seeing 2"
2002 Feb 7/8	R	40	6.9	181	Not photometric, seeing 3" - 5"

each night, through one of either a Harris B, V or R filter. The exposure time for each individual frame was 40 seconds. Combined with the fast readout time of just over one minute, this gave a duty cycle of $\sim$ 2 minutes. Full details are given in Table 3.2. Standard calibrations such as sky flats and bias frames were also obtained each night.

Data reduction was carried out using standard *Starlink* software routines (e.g. *Figaro*, Shortridge (2001)). Aperture photometry was performed using the *Photom* package (Eaton et al., 2001). Differential magnitudes were then calculated with respect to a brighter comparison star in the CCD field of view.

Further short photometric observations of HS1136 were also made from the JKT by Burleigh, Good, & Brinkworth during 2002 May 12-19 and 2002 May 26 - June 2, to help to unambiguously determine the binary orbital period. Typically, a set of five to ten 40 second exposures was made through a V filter each night. Data reduction was performed in an identical manner to that described above.

3.3 UH 2.2m Photometry

CCD photometry of HS1136 was obtained by collaborator Dr. Steve Howell of NOAO on 08 April 2003 UT at the University of Hawaii 88" telescope located on Mauna Kea. The observations were made with the OPTIC CCD camera using the newly implemented "video mode" for high speed CCD photometry (Howell et al., 2003). Integrations of 30 sec in a standard V filter were obtained from 8:30 to 10:45 UT and three local stars of similar brightness were used as comparisons for the differential photometry. HS1136 was placed on the standard system using observations

of the photometric standard fields near PG1047+694 and PG1528+062 (Landolt, 1992). The CCD photometry yielded a V-band magnitude of 13.63 ± 0.03 at an orbital phase of about 0.25.

3.4 2MASS Photometry

Near infrared photometry of HS1136 was obtained from the 2MASS All-Sky Point Source Catalog (http://irsa.ipac.caltech.edu/). The resulting magnitudes are J=12.314±0.021, H=11.695±0.024, and K_s=11.543±0.021, from which the corresponding colors can be derived (Carpenter, 2001), J-H = +0.619±0.032 and H-K_s=+0.152±0.032. These 2MASS magnitudes, colors, and uncertainties are used to estimate the apparent spectral type of the main sequence component of the binary system.

CHAPTER 4

HS1136+6646 Data Analysis

4.1 Radial Velocities

4.1.1 Optically Derived Velocity Measurements

Radial velocities of the K7 companion were measured from the unresolved emission lines in the optical data using standard IRAF packages by the following procedure. A template spectral image was formed by first flattening all the HS1136 observations with a 30^{th} order spline to remove the stellar continuum, applying a heliocentric velocity correction for each image, and then applying a preliminary velocity correction to shift each image onto the spectra with the strongest emission lines. All of the flattened spectra were then combined with the routine 'scombine' using a logarithmic wavelength scale. The heliocentric velocity for the template was removed for use in 'fxcor' ('fxcor' automatically applies a heliocentric correction). The original flattened spectra were then run through the 'fxcor' package which outputs the observed velocities for each spectra relative to the template. These observed velocities were then used to refine the preliminary velocity corrections and produce an improved template. This refining procedure was repeated, typically twice, until output velocities did not change significantly with each improved template. Radial mean velocities from this iteration procedure yielded uncertainties typically of 3 or 4 km s^{-1} (see Fig 4.1), in those spectra where the emission lines are strong.

Radial velocity curves for both components of the HS1136 system are shown in Figure 4.1. The apparent velocities of the K star are derived directly from the unresolved Bok CCD spectra of the emission lines. It should be noted here that the Mayall echelle spectra reveal the H I lines to be surprisingly broad and to consist of asymmetric centrally-reversed line profiles (see §4.4.3). Thus, the velocities in Figure 4.1 pertain to centroids of the emission lines. Since these emission lines may

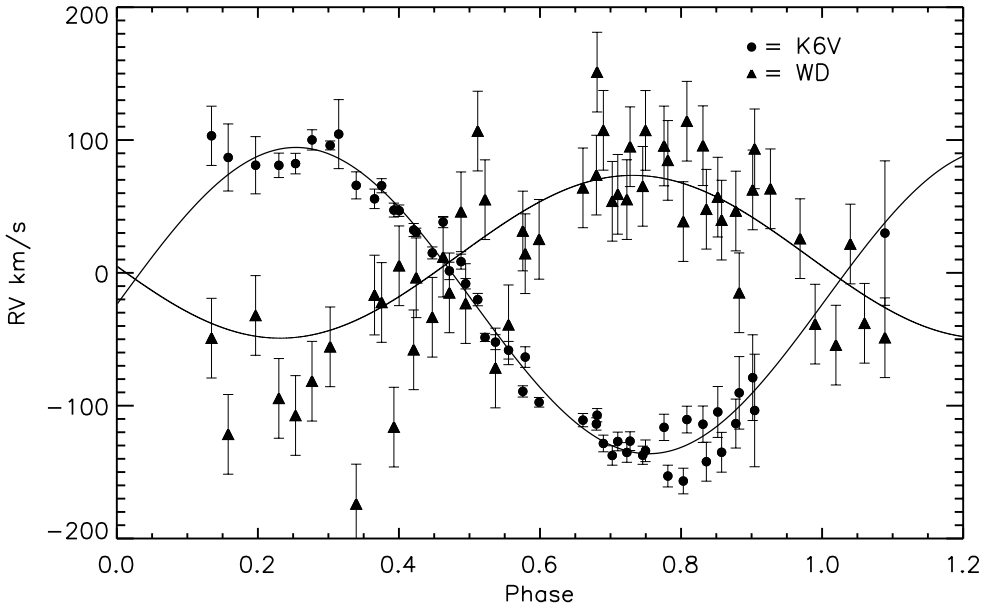

Figure 4.1: Folded radial velocities for both components derived from optical data, phased with a period of 0.83607 days.

contain non-photocentric components, they may also possess possible non-orbital biases.

For the optical data, the estimate of the K velocity for the white dwarf, based solely on the weak He II λ4686 line, is K_{WD}= 61±10 km s^{-1}. A significantly better estimate, however, is available from the analysis of the 2003 May *FUSE* observations of HS1136, which covered nearly a full orbital cycle and is discussed in §4.1.2.

All of the emission lines from the narrow irradiation component are observed to disappear near inferior conjunction and remain undetectable for ∼15% of the total orbit. At this orbital phase, the observed spectrum is effectively a composite of the white dwarf and the dark side of the K star. A DA+dM4 binary system with similar emission line behavior, PG 1224+309, was studied by Orosz et al. (1999) where the authors determined an inclination of 77° ± 7°. The 0.25 day period PG1224+309 system is only a few degrees away from giving rise to eclipses but the emission lines are seen throughout the entire orbital phase. Emission line disappearance in the HS1136 system therefore suggests relatively a high inclination.

Measurements of the equivalent widths of the spectral lines show a modulation at the same orbital period, but with a 1/4 phase difference (see Figure 4.2 and Table 4.1). This difference is consistent with the notion of the reflection effect giving rise to the narrow peaks of the photospheric emission lines.

4.1.2 *FUSE* Derived Velocity Measurements

Radial velocity determainations of the WD (see Figure 4.3) were made using the O VI $\lambda\lambda$ 1032, 1038 resonance doublet since they are strongest photospheric absorption lines in the *FUSE* wavelength regime, free of ISM or airglow contamination. The LiF 1a channel, containing the best S/N and which the *FUSE* spacecraft uses for guidance tracking on the stellar signal, was selected for the velocity measurements.

The *FUSE* spectra, taken with the wide LWRS aperture, are not on an absolute wavelength scale and can vary with the position of the stellar image on the aperture thus requiring a linear wavelength shift for each spectra. To establish an absolute velocity scale, we utilized the stationary interstellar features present in the spectra

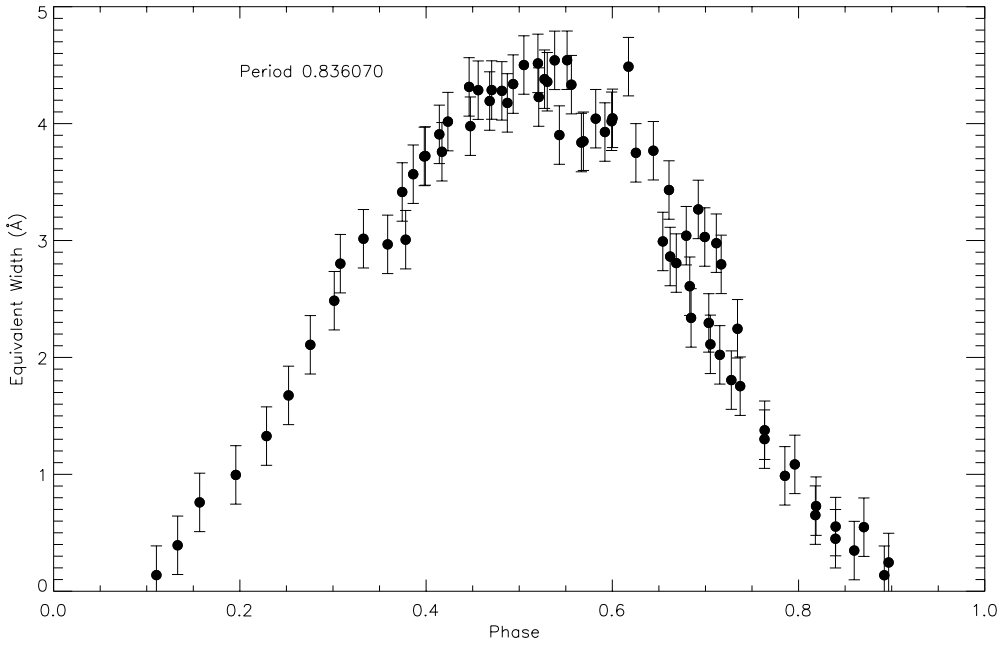

Figure 4.2: Mean spectroscopic emission line equivalent widths as a function of orbital phase (see discussion in text). Data for 2001 Mar., 2001 May, 2001 Dec. and 2002 Mar. are phased with a period of 0.83607 days.

Table 4.1: Bok equivalent Width Measurements of Emission lines at Orbital Phase=0.5

Species	Wavelength Å	Continuum (ergs $cm^{-2}s^{-1}Å^{-1}$)	Flux (ergs $cm^{-2}s^{-1}Å^{-1}$)	Equivalent Width Å	GFWHM† Å
H I	3970.072⋆	2.362×10^{-14}	9.958×10^{-14}	-4.22	3.526
H I	4101.740	1.968×10^{-14}	7.439×10^{-14}	-3.78	3.287
H I	4340.470	1.665×10^{-14}	7.385×10^{-14}	-4.44	3.124
H I	4861.330	1.119×10^{-14}	6.008×10^{-14}	-5.37	3.600
HeI&H I	3888.650	2.615×10^{-14}	9.188×10^{-14}	-3.51	3.623
He I	4026.191	2.241×10^{-14}	1.738×10^{-14}	-0.77	3.019
He I	4120.820	2.190×10^{-14}	6.686×10^{-15}	-0.31	3.264
He I	4143.760	2.200×10^{-14}	5.022×10^{-15}	-0.23	2.378
He I	4387.929	1.562×10^{-14}	7.074×10^{-15}	-0.45	2.658
He I	4471.479	1.463×10^{-14}	1.358×10^{-14}	-0.93	2.626
He I	4713.146	1.274×10^{-14}	6.121×10^{-15}	-0.48	2.690
He I	4921.931	1.180×10^{-14}	1.265×10^{-14}	-1.07	3.173
Ca II	3933.660	2.478×10^{-14}	2.685×10^{-14}	-1.08	3.016
C II	4267.260	1.702×10^{-14}	6.312×10^{-15}	-0.37	2.583
Mg II	4481.245‡	1.464×10^{-14}	8.717×10^{-15}	-0.60	2.258

†GFWHM - Full width at half maximum based on a Gaussian fit.

‡Blend of 4481.160 and 4481.330

⋆Includes the Ca II λ 3968.470 line, explaining a relatively larger equivalent width and GFWHM as compared to the other hydrogen lines.

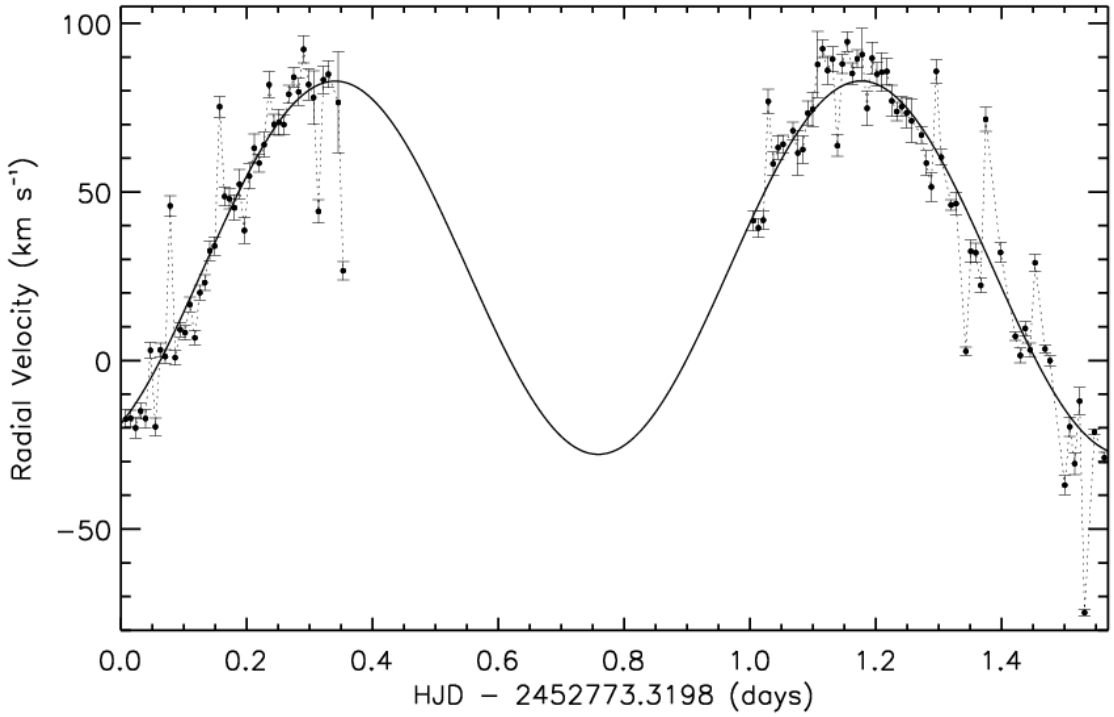

Figure 4.3: The *FUSE* radial velocity curve of the white dwarf.

as fiducials and separately determined the absolute radial velocity of these features from interstellar features in the *Hubble Space Telescope* spectra of HS1136, which are on an absolute scale. Cross correlation radial velocity measurements of the ISM, O I λ 1039 ISM line were used for the corrections to the O VI measurements. The preliminary analysis of Sing et al. (2004a) did not include these corrections, leading to differences in system parameters which are larger than the original error quoted (see §4.3.2).

The radial velocities were determined by fitting Gaussian profiles to the O VI absorption lines in the first spectra to determine its wavelength position and velocity and then correlating all subsequent spectra to the initial spectrum. Because of variations observed in the O VI line profiles (see §4.4.4) and due to the irregular stellar continuum in the vicinity of the O VI lines, a rigorous analysis of the systematics of the velocities was undertaken. No statistical difference in velocity was found between the use of any particular spectrum as the template for the cross-correlation,

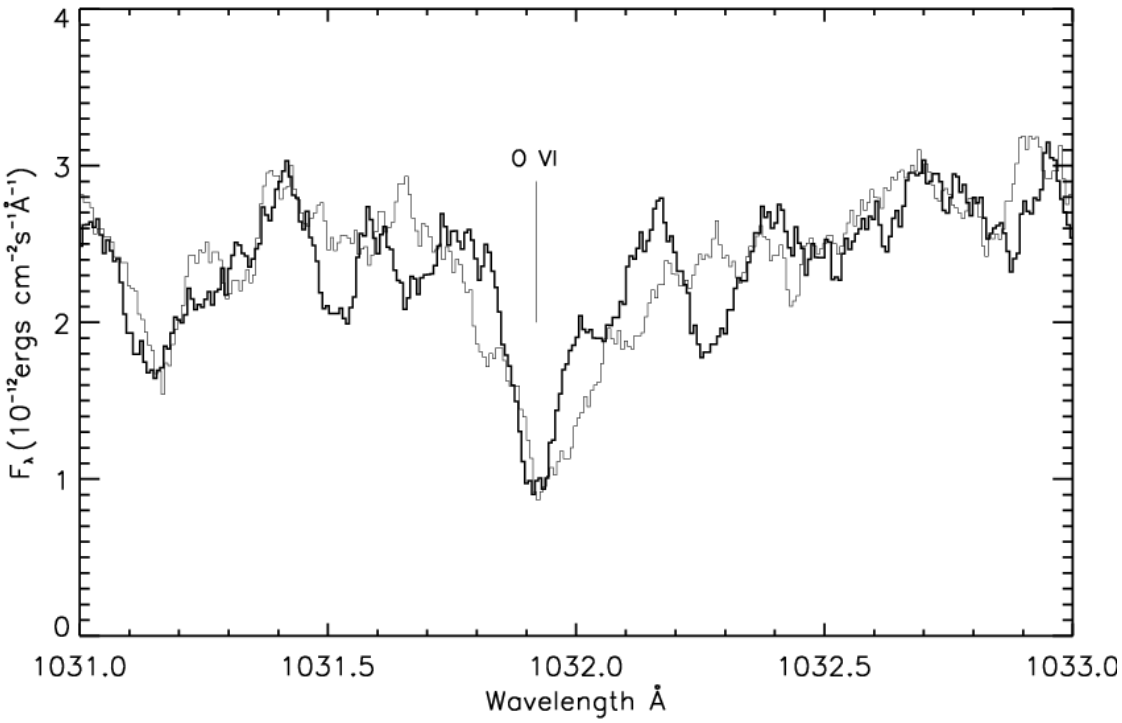

Figure 4.4: Two *FUSE* spectra Doppler shifted and overploted, illustrating the changing line shape of the O VI λ1032 photospheric absorption feature.

indicating minimal systematic errors resulting from template mismatches as the O VI line shape changes (see Figure 4.4 and §4.5 for an interpretation of these line shape changes). A small wavelength region, containing only the absorption line profile, was correlated to avoid the potential cross-correlation on any velocities or features other than that of the WD. A Gaussian was then used to fit the correlation function in order to determine the wavelength shift between the two spectra and thus the radial velocity difference between them. The velocity uncertainties were found from the χ^2 distribution for a series of Doppler shifts, calculating the 1σ confidence levels from $\chi^2_{min}+1$. This method yielded typical radial velocity uncertainties of 2-3 km s^{-1}.

4.2 Determination of Rotational Periods for HS1136+6646

4.2.1 Orbital Ephemeris

The orbital period was determined using the χ^2 based phase dispersion minimization (PDM) technique as described in Stellingwerf (1978). The V-band photometric data was supplemented with the emission line equivalent width data to achieve better accuracy. The equivalent widths of the emission lines were measured from the five brightest H I and He I lines (see Figure 4.5, and Table 4.1). An average strength for these five lines computed for each spectrum was used in the PDM technique, yielding an orbital period of 0.83607±0.00003 days using all of the ground based spectroscopic data (see Table 2.1 and Figure 4.2). Since the 234 min modulations are not necessarily related to the orbital motion, phasing the V-band data alone led to systematic errors in determining the period, since the PDM couples to the small variations. In order to avoid this systematic error, a preliminary fit of the small modulations with a sine function was made and subtracted from the V-band photometric data (see Figure 4.6). This procedure was performed by first fitting the orbital variations with a sine function of the form

$$V_{mag}(t) = V_O \sin\left[2\pi\frac{(t-T_0)}{P}\right] + < V >, \tag{4.1}$$

where V_{mag} is the observed V magnitude, V_O is the amplitude of the light curve, and $< V >$ is the mean magnitude. The fit was then subtracted from the photometric data before determining the period. Although some small modulations are still present, a period of 0.83604±0.00004 days is obtained from the PDM fit (see Figure 4.7). This closely matches the period obtained with spectroscopic equivalent width data (see Figure 4.2). The radial velocity data agrees well with this period, as shown in Figure 4.1, which over-plots the radial velocity data as sinusoids of the form

$$V_{WD}(t) = \gamma\prime + K_{WD}\sin\left[2\pi\frac{(t-T_0)}{P}\right], \tag{4.2}$$

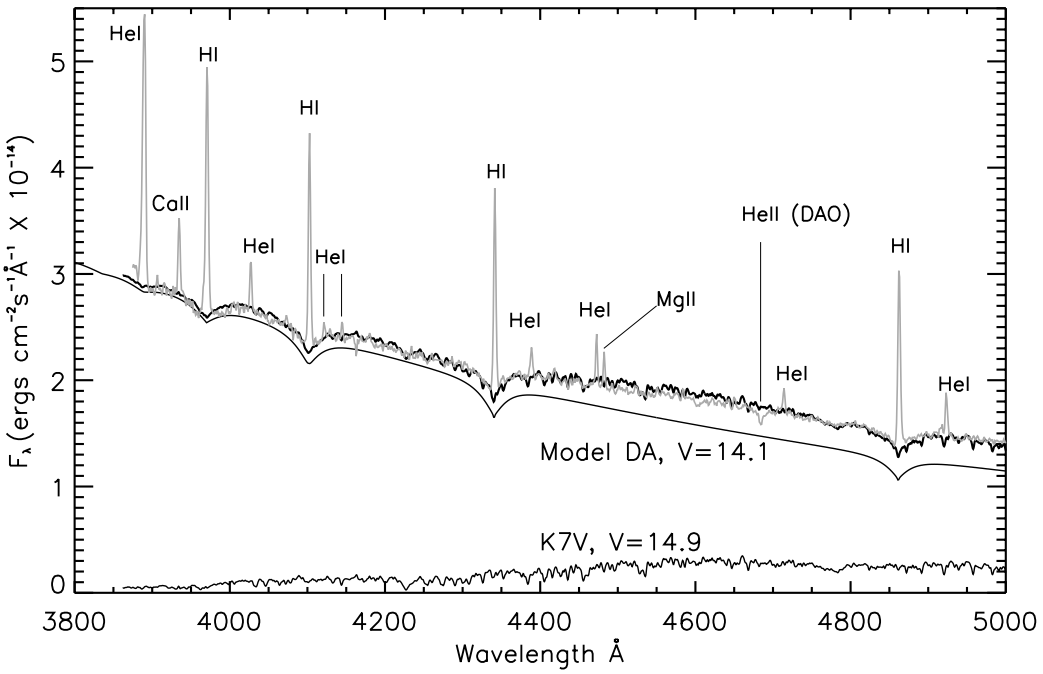

Figure 4.5: Models of the HS1136+6646 components and composite spectra overplotted with the Bok spectroscopic data (grey) near superior conjunction.

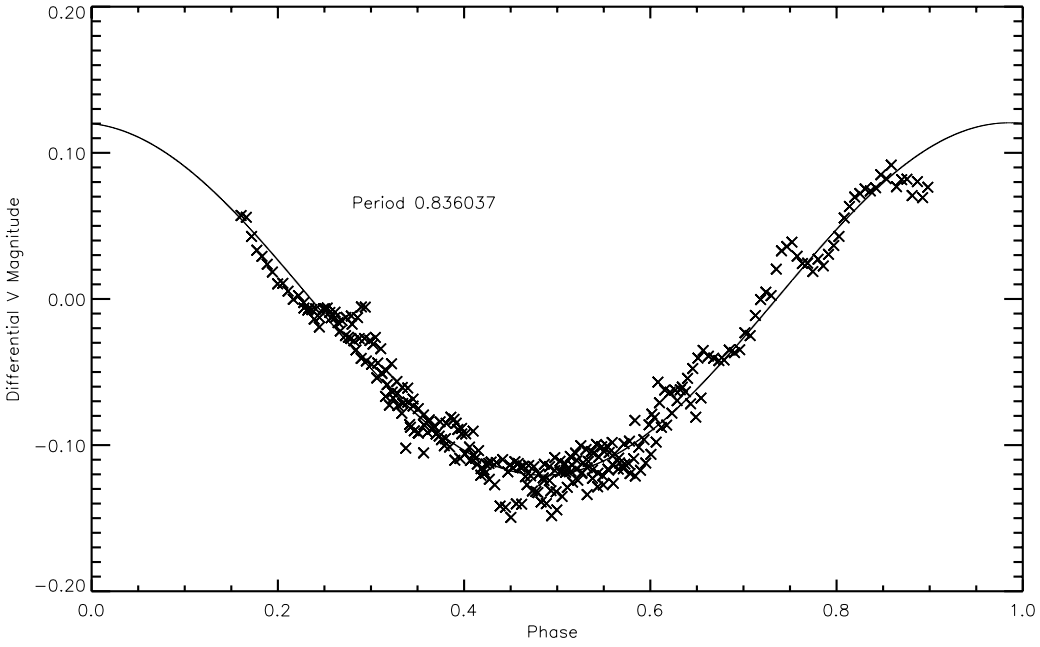

Figure 4.6: Resampled V-band SARA photometry phased after subtracting a sine curve fit to the small modulations. Phase dispersion minimization fits result in an orbital period of 0.83604 days.

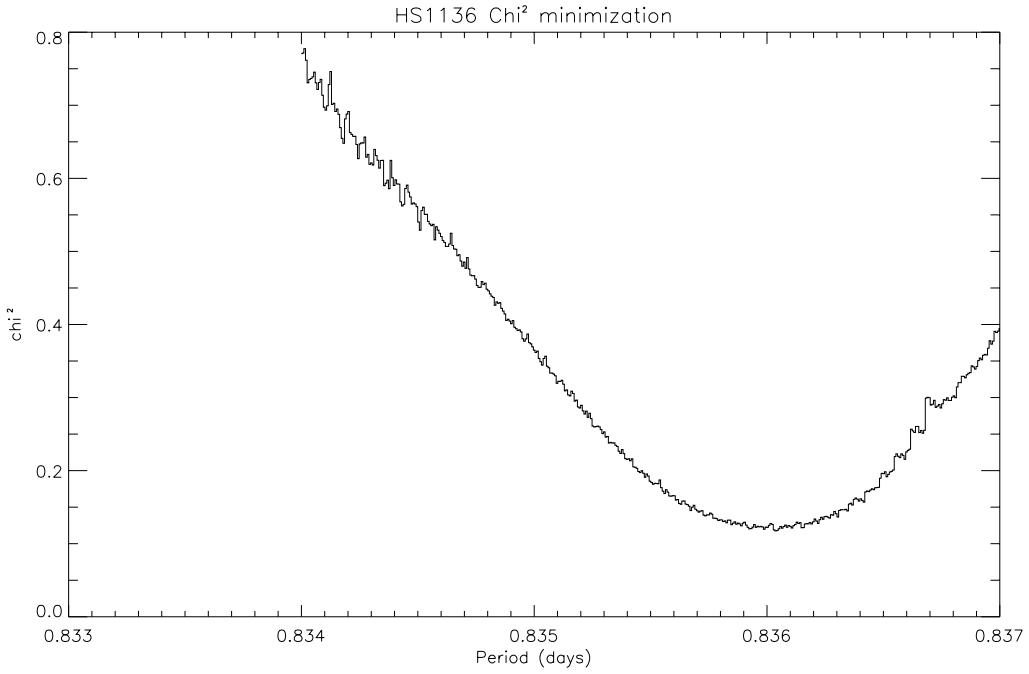

Figure 4.7: χ^2 plot from the PDM analysis. The minimum corresponds to the determined orbital period of 0.83604 days.

for the white dwarf, and

$$V_{MS}(t) = \gamma + K_{MS} \sin\left[2\pi \frac{(t - T_0)}{P}\right], \tag{4.3}$$

for the secondary star, with the orbital parameters as listed in Table 1.2. Where K_{WD} and K_{MS} are the K velocities, P is the orbital period, and T_0 and t are, respectively, the epoch and time. γ and $\gamma\prime$ (Equation 4.2) are respectively the system gamma velocity and the algebraic sum of the system velocity plus gravitational red shift of the white dwarf.

4.2.2 White Dwarf Rotational Period

UBVRI photometric observations revealed a dominant time-dependent sinusoidal variation of the light emission from HS1136 due to the orbital motion in the binary

system and the reflection effect. From the reflection effect, the hemisphere of the secondary star facing the hot white dwarf is optically brighter than the outward-facing hemisphere. As the two stars orbit one another, the observed UBVRI fluxes vary with the percentage of the illuminated hemisphere seen.

In addition to the dominant amplitude photometric variations associated with the orbit, which have a half amplitude of $\sim$0.12 mag; low amplitude photometric variations of much shorter period are also observed. These short-period modulations appear to have a period of 113.13 min, a half-amplitude of $\sim$0.0093 mag., and can be clearly seen in the orbital photometric light curve of Figure 4.6. They appear to be present in all observations and to be independent of orbital phase.

Handler (1998) searched for short period pulsations in HS1136 using high speed relative photometry. No evidence of short period variations were observed but the short duration of the observation (76 min) together with the orbital variations and the low frequency filtering of the data would have made it difficult to detect any variations of the type we report. The low amplitude, 113 min modulations are presumed to originate with the hot white dwarf and to be associated with either a rotational photometric modulation due to a magnetic spot or pole on the white dwarf's surface. Alternative explanations, such as pulsational instability in the white dwarf or rotational modulations of the K star, are less likely as the period is much longer than any known pulsational instablilties and the K7 secondary is believed to be tidally locked. The observed 113 minute period of the modulations is well outside the known range of degenerate star pulsations and is too short for any stable rotation of the K star.

In order to obtain a multi-night ephemeris for the low-amplitude modulations, a Lomb periodogram (PDM) of the 2004 Feb. data was used to help identify the period of the dominant frequency (see Figure 4.8). The photometric data was first detrended, removing the orbital variations (see Figure 4.6), and a 55 point boxcar smooth applied to the residuals. Those data points showing sufficient contamination from cloud cover were removed from the dataset. This procedure resulted in a period of 117.07 minutes for the photometric modulations, five minutes longer than the

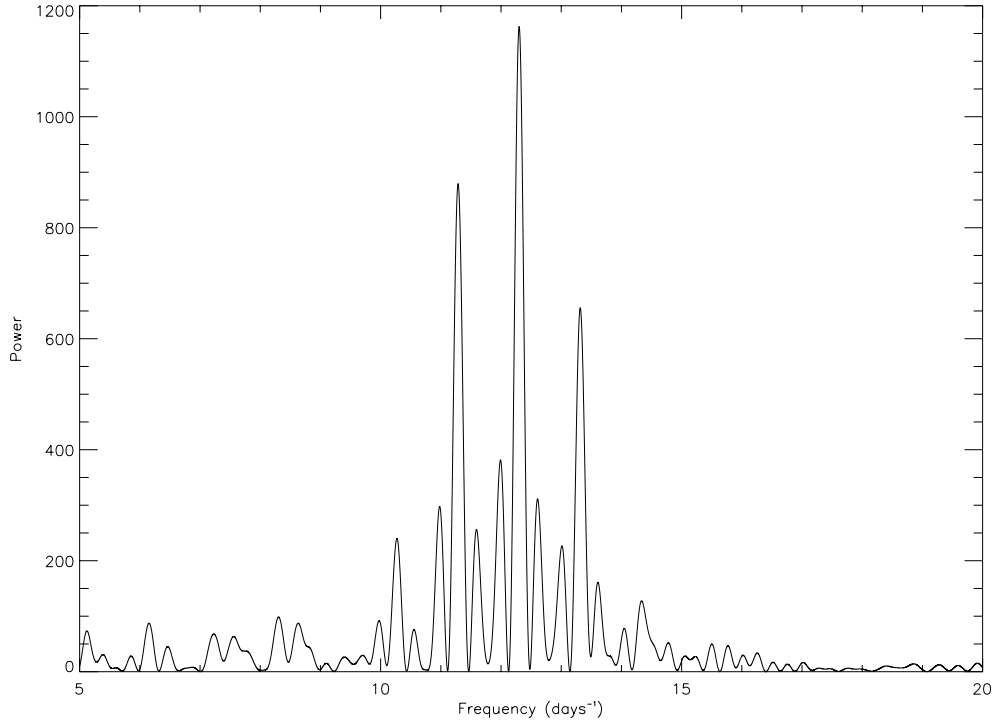

Figure 4.8: Periodogram of the SARA V-band photometric data.

original estimate in (Sing et al., 2004a).

Searching near the period derived from the periodogram, a χ^2-based phase dispersion minimization (PDM) technique (Stellingwerf, 1978) was used to further refine the dominant frequency, giving a final value of 117.078 minutes. The four nights of, data over-plotted with the derived spin period, can be seen in Figure 4.9. The lightcurve in Figure 4.9 is seen to alternate, with every other cycle reaching a magnitude of 0.005 lower than the previous cycle. This indicates the spin pulse of HS1136+6646 is *double-peaked*. Phasing the data on twice the value found from the PDM technique, 234.156 minutes, illustrates the double-peaked modulation of the light curve (see Figure 4.10).

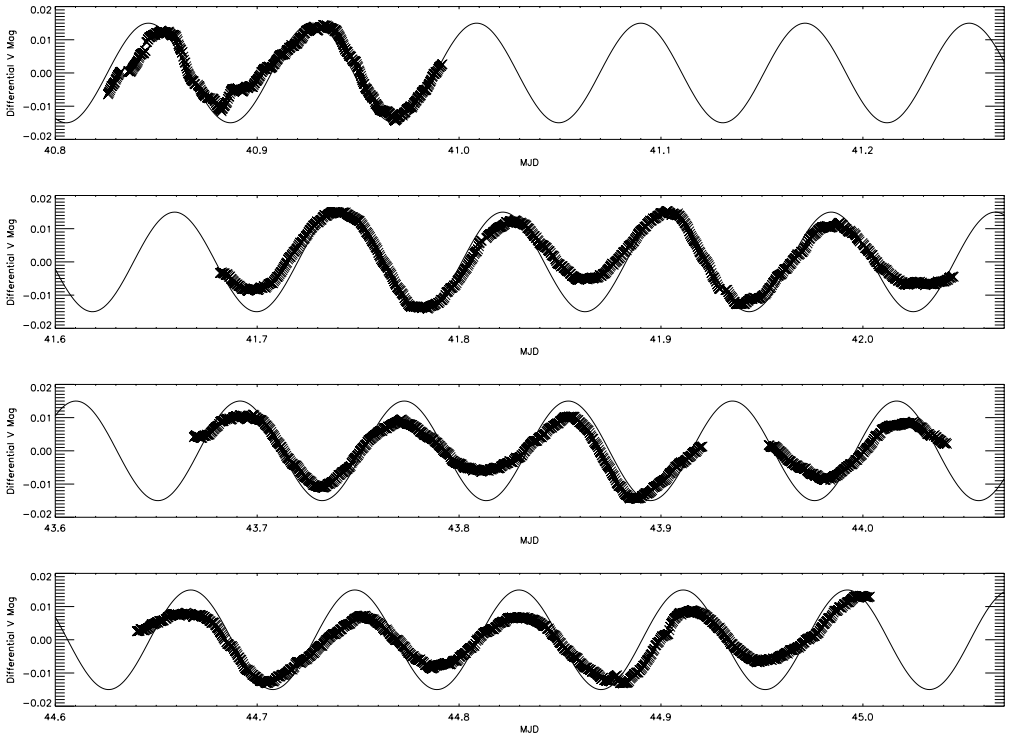

Figure 4.9: SARA differential V-band photometry on four seperate nights with the orbital variations removed. The data has been smoothed and over-plotted is a 117.078 minute period sine curve. Note deviations for alternate peaks and valleys with respect to the sine wave.

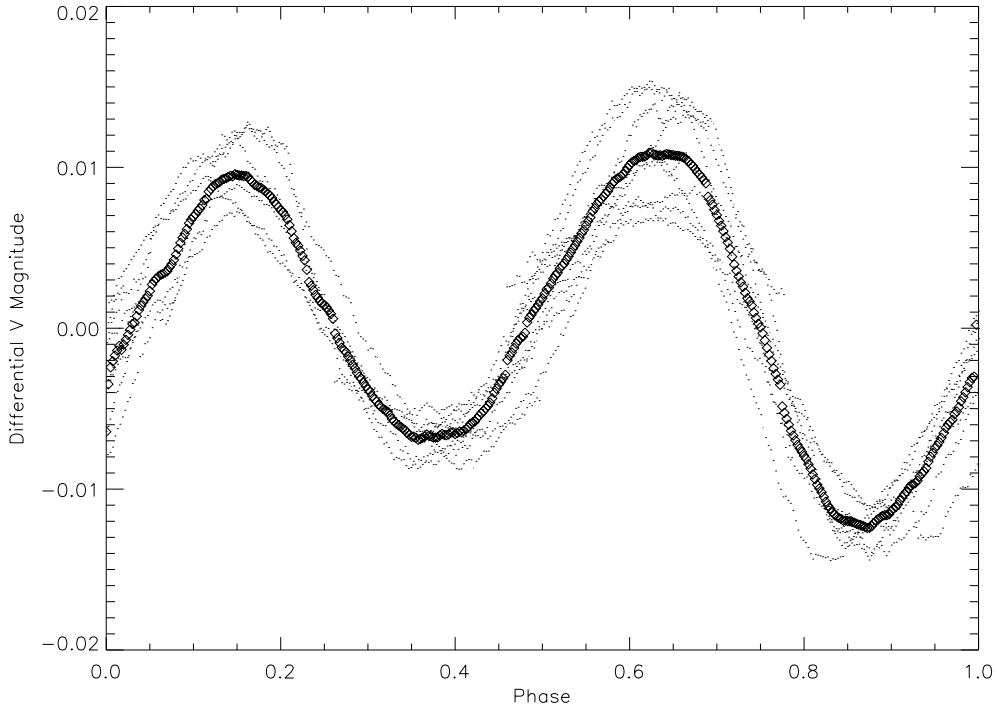

Figure 4.10: Photometric data (dots) from Fig 2 phased on a 234.008 minute period illustrating the double-peaked spin pulse. The diamonds represent the average of the co-phased data.

4.3 Binary Components

4.3.1 Secondary Main Sequence Star

Since the radial velocity profile of the K7V star is derived from observations of the emission lines, the observed value of the mass ratio q=0.6 represents an upper limit ($q = M_{MS}/M_{WD}$). In order to shift the apparent radial velocity from the center of light to the center of mass, a correction of +16 km s^{-1} to the radial velocity is needed (see Orosz et al. 1999 velocity correction discussion and technique). This estimate assumes a radius of 0.79 $R_{\odot}$ and mass 0.38 $M_{\odot}$ (Pickels 1998) for the secondary star which is uniformly illuminated over one hemisphere, along with a q value of 0.6. With an observed value of K_{K7V}=115 km s^{-1}, the "K corrected" value is then 131 km s^{-1}. The new q value is then 0.53 corresponding to a secondary star mass of M_{dK}=0.33 $M_{\odot}$.

4.3.2 White Dwarf

The resulting radial velocity curve derived from the O VI $\lambda\lambda$ 1032,1036 photospheric absorption lines shows a sinusoidal component consistent with the orbital motion of the WD found by Sing et al. (2004a), Figure 4.3. The radial velocity curve was fit with a function of the form,

$$V_{WD}(t) = \gamma' + K_{WD} \sin\left[2\pi \frac{(t - T_0)}{P}\right] \tag{4.4}$$

where K_{WD} is the K velocity of the WD, P is the orbital period, T_0 and t are respectively the epoch and time, and γ' is the algebraic sum of the system velocity with gravitational red shift of the WD, v_g. The apparent radial velocities show numerous points, $\sim$20%, which have large deviations from the expected smooth sinusoidal behavior. As discussed in §4.5, these occur at specific WD spin phases and we believe they are due to systematic magnetic modulations of the line shapes related to the rotation of the WD. We therefore assigned these points a low weight in the sinusoidal fit. The resulting parameters are listed in Table 1.2. Several of the parameters rederived in Table 1.2 differ from Sing et al. (2004a) outside the

quoted error, indicating systematic errors. The difference between the parameters are twofold. First, the analysis of Sing et al. (2004a) used the same *FUSE* data to determine K_{WD} as this work, but the necessary corrections to the wavelength solution required *HST* UV spectra, unavailable at the time. Second, M_{WD} in this work is determined directly through v_g, minimizing the problems of atmospheric model fitting and Balmer line contamination found in Sing et al. (2004a). With the proper corrections made during data reduction, and a M_{WD} nearly independent of model atmosphere fits, the system parameters of HS1136 derived in this work should therefore be much more robust and accurate.

A gravitational redshift for the WD allows an accurate an independent estimation of the mass, assuming an effective temperature, T_{eff}, and the degenerate mass-radius relation of Wood (1995). Small corrections need to be applied to the measured difference in system velocities, 48.4±1.5 km s^{-1}, in order to properly calculate the WD's gravitational redshift. These corrections (see Morales-Rueda et al. 2005) include adding the gravitational redshift at the white dwarf from the secondary star,

$$\frac{GM_{MS}}{R_{MS}c} \tag{4.5}$$

the difference between transverse Doppler shifts between the secondary and primary stars,

$$\frac{K_{MS}^2 - K_{WD}^2}{2c\sin^2 i} \tag{4.6}$$

and accounting for the gravitational potential resulting from having a companion,

$$\frac{G}{ac}(M_{WD} - M_{MS}), \tag{4.7}$$

where G is the gravitational constant and c is the speed of light. The other parameters are listed in Table 1.2. An initial estimate of the orbital parameters necessary for the corrections can be calculated by simply using the difference in system velocities as the gravitational redshift. For HS1136 we used an iterative process in determining the final values of the gravitational redshift corrections. These corrections are small, typically on the order of a few percent. After several iterations calculating

the orbital parameters, we find a WD gravitational redshift of 48.8±1.5 km s^{-1}. For the corrections, the secondary star was assumed to have a photospheric radius typical of a K7 main sequence star, given that such young post-CE secondaries are out of thermal equilibrium (see Schreiber and Gänsicke 2003 and Sing et al. 2004a).

The T_{eff} of the WD was determined in Sing et al. (2004a) to be 70,000 K based on Balmer line fits to an extracted WD spectrum but greater than 110,000 K based on Lyman line fits to *FUSE* spectra. A description for the T_{eff} general differences are discussed in detail by Barstow et al. (2003) for DA WDs and by Good et al. (2004) for DAO WDs. Even though the T_{eff} derived from fitting Lyman lines is substantially different from those calculated with Balmer lines, the theoretical model calculations of gravitational redshift have only a weak dependence on T_{eff} and only represent a small uncertainty in the derived mass for the WD, Silvestri et al. (2001). Indeed, the WD mass derived with a T_{eff}=70,000 K is 0.83 $M_{\odot}$ compared to a mass of 0.86 $M_{\odot}$ using a T_{eff}=110,000 K. In lieu of these two WD mass estimates, we will adopt a mass of 0.85±0.02 $M_{\odot}$. This mass estimate is consistent with the uncertainties of both the T_{eff} and the v_g. With an accurate WD mass, a final circular orbital solution follows from Kepler's third law giving the orbital separation a,

$$a^3 = G(M_{WD} + M_{MS})(\frac{P}{2\pi})^2, \tag{4.8}$$

while inclination follows from

$$\sin^3 i = \frac{PK_{MS}(K_{WD} + K_{MS})^2}{2\pi G M_{WD}} \tag{4.9}$$

(see Table 1.2). The derived inclination of 71.8°±0.3° is consistent with the observed reflection effect variations seen in the optical as well as the lack of any observed eclipses, which would occur at inclinations above 83°.

The secondary star (through the mass ratio) is found to have a mass of 0.37 ± 0.02 $M_{\odot}$, giving it a mass consistent with that of a M2.5V star. The spectral type of the secondary, however, based on atomic and molecular features (Heber et al., 1996) as well as modeling optical spectra and near-IR colors (Sing et al., 2004a) consistently gives a spectral type of K7V. This apparent discrepancy was realized

to be the manifestation of the long thermal time-scale for the relaxation of the secondary star's envelope compared with the short elapsed time since the CE phase. Thus the M2.5V star is out of equilibrium, resulting in an inflated radius. Indeed, a mass typical of a K7V star can be ruled out for the secondary component, because the observed mass ratio would require the WD to have a mass of 1.39 $M_{\odot}$. This is not only dangerously close to the well recognized Chandrasekhar mass limit, but quite inconsistent with the observed gravitational redshift.

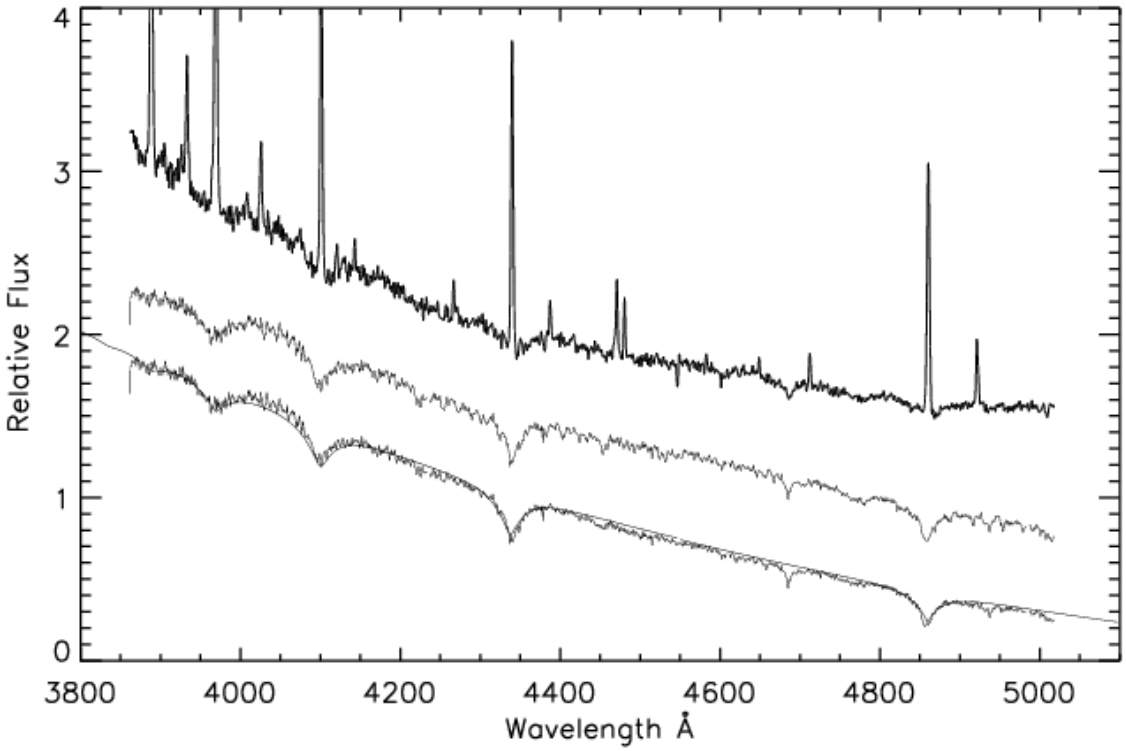

Figure 4.11: The Bok 2.4m emission line spectra at superior conjunction (top) compared with the spectrum at inferior conjunction (middle) and the extracted white dwarf spectrum (bottom). The best fitting model white dwarf spectrum of T_{eff}=70,000 K and log g=7.75 is over-plotted on top of the extracted white dwarf spectrum.

4.4 Characteristics of the Stellar Components

4.4.1 Properties of the White Dwarf

In principal, it is possible to independently estimate the effective temperature and gravity of a hot white dwarf such as HS1136 from a detailed analysis of both the Balmer and Lyman line profiles. However, in the case of HS1136, the H I Balmer lines are contaminated both by the continuum from the secondary star and the emission lines. I have attempted to minimize this contamination by the following procedure. The derived white dwarf parameters in this section are completely independent of the parameters derived in §4.3.2, and rely solely on optical data.

Optical spectra obtained near orbital inferior conjunction (see Figure 4.11) with

the Bok Telescope were used to extract a characteristic white dwarf spectrum. In order to remove as accurately as possible, the K star from the composite flux, a template spectrum of the K7V star BD +46° 1635 was obtained with the Bok Telescope on 2003 March 23. This ensured that the template K star spectrum had the same resolution, dispersion and wavelength range as the HS1136 spectra at inferior conjunction. Short-ward of 4000 Å, the flux of HS1136 is dominated by the hot white dwarf, making it possible to accurately flux calibrate an assumed *preliminary* model of the white dwarf (T_{eff} = 50,000 K, log g = 8.0). The template K7V star was then flux-calibrated so that the composite model flux corresponded to the observed levels of the HS1136 spectra. A preliminary model white dwarf spectrum was then obtained by subtracting the spectrum of the correctly flux-calibrated K7V star from the HS1136 spectra at inferior conjunction. This white dwarf spectrum was then fit with a grid LTE, pure-hydrogen model stellar atmospheres produced by TLUSTY (Hubeny and Lanz, 1995).

A final set of white dwarf parameters were obtained by the following iterative procedure. A synthetic white dwarf spectrum was generated from fitted T_{eff} and log g values which was used to rescale the subtracted K7V template spectrum. The new white dwarf spectrum was then refitted and a new set of white dwarf parameters determined. A final set of parameters corresponding to T_{eff} = (70,000±5,000) K and log g = 7.75±0.25 was achieved after several iterations. This final model is shown in Figure 4.11. Note that the fitting procedure employed normalized individual Balmer profiles, thereby minimizing any bias associated with the sloping spectral energy distribution. Best results were obtained from the Hγ and Hδ lines, suggesting that not all of the K7V flux was properly subtracted from the composite spectra.

In principal, it is is also possible to use the H I Lyman series lines to estimate the T_{eff} and log g of HS1136. Barstow et al. (2003) have extensively investigated the relationship between Balmer line estimates and those derived from the *FUSE* Lyman lines spectra for a set of 16 DA white dwarfs, while Good et al. (2004) analyzed the relationship for 16 DAO white dwarf (including HS1136+6646). Barstow et al. (2003) and Good et al. (2004) used the following model fitting procedure.

They used a grid of homogeneous model stellar atmospheres calculated using the non-local thermodynamic equilibrium code TLUSTY (Hubeny & Lanz 1995) along with SYNSPEC, its associated spectral synthesis program. A large grid of models were then calculated containing a wide range of T_{eff}, log g, and heavy element abundances. A χ^2 minimization technique was then used to determine the model spectra that best fit the optical H I Balmer lines. The same grid is then used to fit the UV H I Lyman lines. In general, they find very good agreement for stars with temperatures below $\sim$ 50,000 K and increasingly wide divergence for stars at higher temperatures. The sense of the difference in temperatures found by these two methods is that Lyman line temperatures began to exceed the Balmer line temperatures at $\sim$ 50,000 K, increasing to a discrepancy of 6% to 10% higher by 60,000 K. The corresponding correlation for gravities shows a good agreement between Lyman and Balmer results. There is a weak indication of higher Lyman line gravities for the very hottest stars but this is based only on two stars with large error bars. At present, there exists no accepted explanation for the differences between the two methods nor is there a clear indication of which method, Lyman or Balmer, provides the best estimate of effective temperature for the hottest H-rich white dwarfs. Good et al. (2004) found the T_{eff} discrepancies to decrease at lower gravities and luminocities for the DAO white dwarfs indicating future work on overcoming the problem might focus on stratification of elements in the white dwarf atmosphere or on mass loss (Good et al. 2004).

Keeping the results of Barstow et al. (2003) and Good et al. (2004) in mind, I have fit the Lyman lines for HS1136 in a χ^2 minimization technique similar to that of Barstow et al. (2003). I find T_{eff} = 110,000 K and log g = 7.0 to 7.5 using the 2001 and 2002 *FUSE* observations. However, this fit is very unsatisfactory (see Figure 2.2) and is also incompatible with the strong continuum which continues up to the Lyman limit with no discernible role off at the convergence of the Lyman series. Models indicate a much higher effective temperature is necessary to match the spectral energy distribution short-ward of 950 Å and the Lyman limit. Clearly, the Lyman line temperature and the FUV energy distribution are incompatible

with our results for the Balmer line fits. It is significant to note that this same effect was found by Good et al. (2004) in his analysis of hot DAO stars, which included HS1136+6646. For HS1136+6646, Good et al. (2004) determined an T_{eff} of 61,787±700 K using the optical spectra but a T_{eff} greater than 120,000 K from the FUV data. Thus discrepancy this represents an unmodeled aspect of the FUV photosphere of HS1136+6646 as well as several other hot DAO stars. Nevertheless, both Balmer and Lyman analysis place HS1136 among the hottest stars considered by Barstow et al. (2003) and among the hottest H-rich white dwarfs known. Although I am presently unable to reconcile the Balmer and Lyman line results, I will adopt the Balmer line parameters; T_{eff} = 70,000 K and log g = 7.75 as a good match to the white dwarf at optical wavelengths and use these results in the discussion which follows.

An estimate of the mass and thermal age of the white dwarf can be obtained from its Balmer line temperature and gravity. Using the thermally evolved models of Wood (1995), I find a mass of M_{WD}=0.63±0.05 $M_{\odot}$ and a thermal age of (8.2±0.7)×10^5 years for the white dwarf. From synthetic photometry of Bergeron et al. (1995) I find a corresponding M_v of 8.5 for the white dwarf. In addition to the temperature and gravity, the optical spectrum of the white dwarf can be used to estimate the photospheric He abundance of the white dwarf. The measured equivalent width of the He II λ4686 Å line is 32mÅ, which for a 70,000 K, log g = 7.75 white dwarf corresponds to a He abundance of He/H $\sim 2\times10^{-3}$.

The mass of the white dwarf derived from the optical data is 3/4 of that derived in §4.3.2 using a gravitational redshift. The large mass differences highlight the problems associated with using model atmosphere fits of very hot white dwarfs stars, such as HS1136+6646. The mass derived from the gravitational redshift is only weekly dependent on the T_{eff}, and therefore should be largely free of the H I Balmer vs. Lyman fit problems.

An estimate of the permissible bounds on the T_{eff} is possible by considering the ionization of ratios of various species in the photosphere. Here I have used the ions N IV/N V, O IV/O V/O VI and Fe VI/Fe VII to determine a lower bound on the

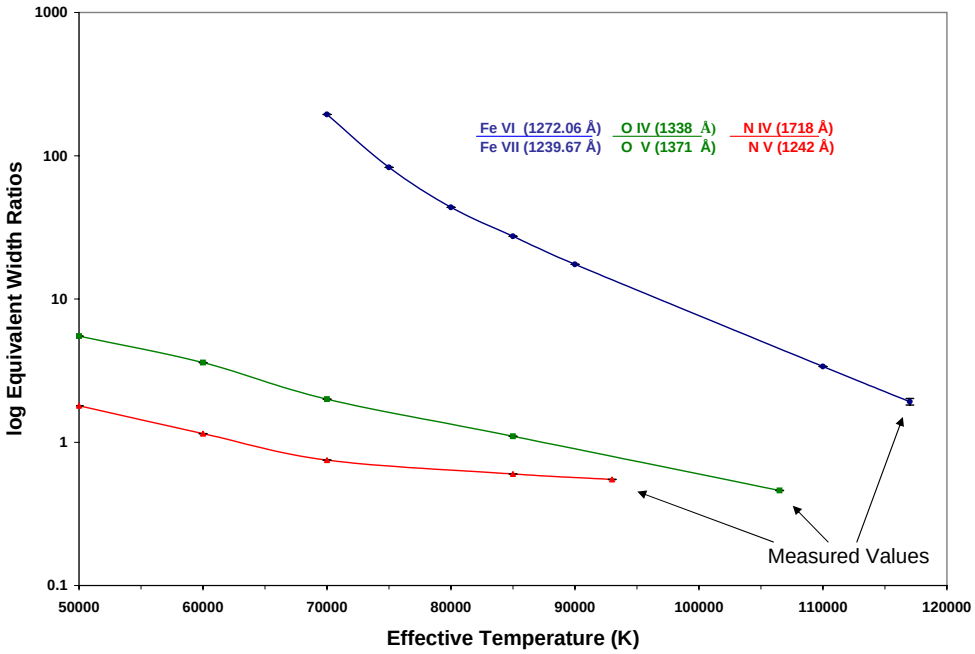

Figure 4.12: Equivalent width ratios for N (bottom), O (middle), and Fe (top) as a function of T_{eff} measured from non-LTE white dwarf model atmospheres. With higher T_{eff}, higher ionization species become more prevalent in the spectra resulting in the equivalent width ratio of a lower ionization to a higher ionization state to decrease. The effect is largely abundance independent and gives an estimate of the T_{eff}. The abundance ratios measured in HS1136+6646 are also plotted. The T_{eff} for each of the measured data points was determined by extrapolation.

T_{eff} by measuring the equivalent widths of these highly ionized heavy elements seen in HS1136+6646. The ionization state of a particular element is largely dependent on T_{eff} providing a way to estimate its value independent of H I Lyman or Balmer line profile fits, or to decide which of these methods gives the most reliable results. With the exception of O VI, these ions are not well represented in the *FUSE* spectra considered by Good et al. (2004). However, the *STIS* spectra do provide good determinations of the equivalent widths of most of these features and thus offer a means to explore the range of permissible temperatures in HS1136+6646.

HS1136+6646 exhibits absorption features from C IV, N IV, N V, O IV, O V, O VI, Fe VI, and Fe VII. The strength of these absorption features as a function of T_{eff}, log g and abundance can be estimated from TLUSTY white dwarf model atmospheres using the spectral synthesis program SYNSPEC. Seen in Figure 4.12 is the theoretical equivalent width ratios for N, O, and Fe as a function of T_{eff} estimated using non-LTE pure H white dwarf model atmospheres. The ratio of the equivalent width measured from a lower ionization state absorption line to that measured from a higher ionization state absorption line is largely independent of the abundance and thus can be used to probe T_{eff}. The equivalent width ratios measured in HS1136+6646 are plotted in Figure 4.12 with the T_{eff} estimated by extrapolating the theoretical equivalent width vs. T_{eff} trend to the measured value. The three T_{eff} estimates indicate the white dwarf in HS1136+6646 is between 95,000 and 117,000 K. This temperature estimate is seen to be much more compatible with the value measured from fitting the H I Lyman lines than that measured from fitting the H I Balmer lines. Indeed the T_{eff} = 70,000 K models which do provide a reasonable fit to the Balmer lines can be completely ruled out by this analysis. The T_{eff} obtained from the Fe equivalent width ratios trend, which is the most sensitive of the three to high T_{eff}, of 117,000 K is in reasonable agreement with the lower limit of 120,000 K determined from fitting the Lyman lines. The presence of Fe VII alone (measured equivalent width of 24±4 mÅ for Fe VII λ 1239.69Å) would seem to rule out effective temperatures below 80,000 K as the Fe VII absorption feature at λ 1239.69 Å was found to be undetectable in cooler model atmospheres.

The high temperature indicated by our ionization ratio analysis has several implications for HS1136+6646 and similar hot DAO stars of the type investigated by Good et al. (2004). First, on a practical level, it complicates the process of identifying many of the lines in our *STIS* and *FUSE* spectra, since many of these features are likely due to unfamiliar higher ionization states not contained in the current generation of models, for example Fe VIII. Second, at the high luminosity implied by our high temperature, mass loss of selected ions may also be occurring, which complicates the analysis of observed line shapes as well as violating the assumption of chemical homogeneity in the atmosphere. Stable, non-dynamic chemical stratification of selected ions within the photosphere is another possibility. Already in DA stars such as G191B2B (T_{eff} 58,000K) the need for stratification of heavy ions has been shown to play a critical role in the interpretation of the EUV spectra (Barstow et al. 2002).

4.4.2 Properties of the Secondary Star

The approximate spectral type of the main sequence companion can be best estimated from the observed 2MASS JHK colors in §3.4. These infrared colors can be compared with the intrinsic main sequence colors of K dwarfs given in Bessell and Brett (1988). After transforming the Bessell & Brett colors to the equivalent 2MASS colors using the color transformations in Carpenter (2001), the observed 2MASS colors correspond the range of spectral types of K4 to M0V with an apparent visual magnitude of 14.34 - 15.27. I will adopt $K7^{+4}_{-2}V$. This estimate is quite consistent with the spectroscopic determination of Heber et al. (1996) based on the atomic and molecular features seen in their red spectrum of the star as well as our modeling of the optical continuum near superior and inferior conjunction which assumed a K7V secondary (Pickles, 1998) and a 70,000 K, log g = 7.75 white dwarf (see Figure 4.5). It should be noted that the 2MASS data were obtained at a phase of 0.22±0.05 which corresponds to the mean of the V-band photometric orbital variations. Second, this also assumes that the main sequence star can be characterized by its JHK colors and is not over-luminous as is the case with V 471 Tau (O'Brien

et al., 2001).

4.4.3 Emission-Line Profiles

Observations of HS1136 were obtained on 2003 January 03-04 with the 4m Mayall Telescope yielding five spectra that cover an orbital phase range from 0.05 to 0.45. These echelle spectra, which fully resolve the emission lines, revealed lines which are unexpectedly broad and asymmetrically double-peaked (see Figure 4.13). Neither of these aspects is obviously compatible with emission arising solely from the irradiated stellar photosphere of the K7V star. The three hydrogen emission lines, Hα, Hβ and Hγ, have full widths at half maximum of 5.34, 3.15, and 2.84 Å respectively. Line broadening due to differential orbital motion during the 1800 second exposure and thermal Doppler broadening at 7,000 K explain the width of the He I, He II, Ca II, and Mg II lines, but not those of the broader H I lines. Unlike the other emission lines, the hydrogen lines clearly show the double-peaked feature. Figure 4.13 shows the development of the Hα emission line as a function of orbital phase over almost half a cycle. As the strength of the emission grows, there is a pronounced asymmetry between the two peaks which tends to diminish near superior conjunction.

One possibility for the double-peaked emission line structures observed in HS1136 is that they are due to an accretion disk. The aspects of the lines which lend themselves to this idea are the asymmetric nature of the peaks and the $\sim$300 km sec^{-1} widths. Under this assumption, I would assign the higher, narrow peak to irradiation from the K7V star with the underlying (now symmetric) double-peaked structure due to a disk of captured (wind) material orbiting the WD. Taking the orbital parameters I have derived in this paper, the line widths observed place the disk far from the WD near a radius of 0.7R$_L$, where R$_L$ is the Roche lobe radius, and its structure would have to be be very optically thin or completely evaporated (a Stromgren sphere) in its interior; a very ring-like disk structure. The argument against an accretion disk is that I note the large decrease in the line strengths and their symmetric nature at phase 0.05, requiring a nearly complete eclipse of the disk by the K7V star.

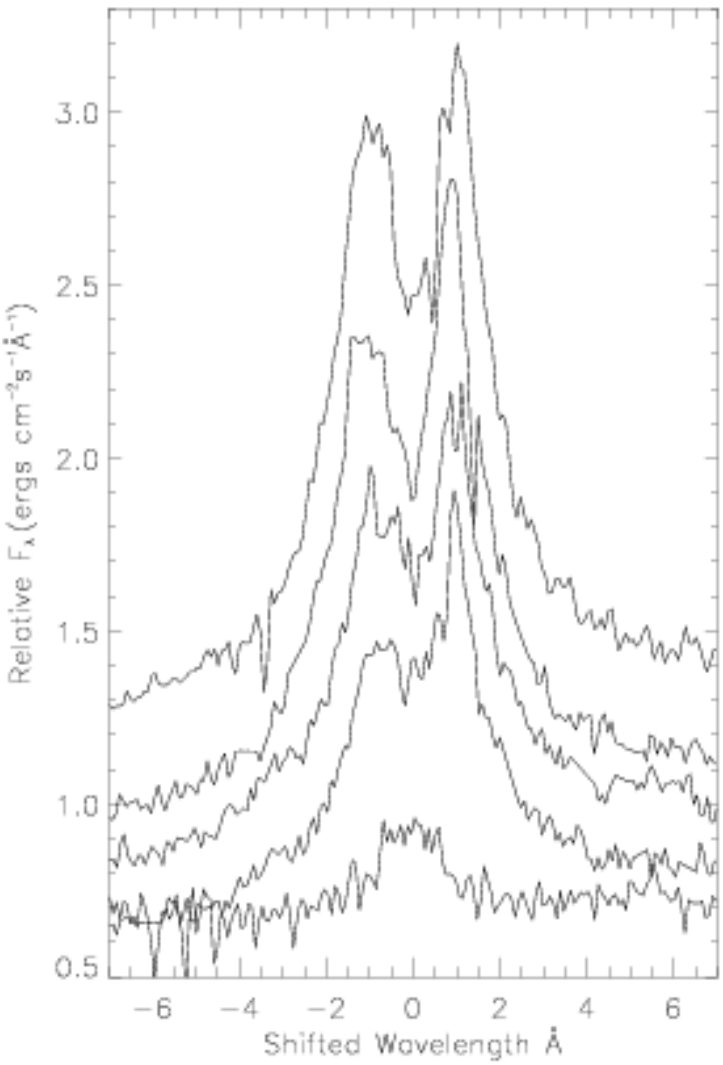

Figure 4.13: The Mayall 4 meter Hα emission line profiles from inferior conjunction (bottom) to superior conjunction (top). The corresponding phases from bottom to top are 0.05, 0.25, 0.28, 0.39 and 0.45.

The double-peaked emission line structure may also be attributed to Stark broadening analogous to BE UMa where the lines are formed deep in the atmosphere of the K7V star (Ferguson and James, 1994). Emission lines in BE UMa from elements heavier than hydrogen, such as C II, C III, and N III, are formed higher up in the atmosphere and thus are not as broad as the Balmer lines. Such would be the case with HS1136 were the He I, He II, Ca II, and Mg II lines are not as broad nor observed to be double-peaked. Unlike HS1136, however, the double-peaked emission line profiles of BE UMa are reportedly symmetric throughout the orbital cycle. The asymmetry of the Balmer lines in HS1136 raises doubts on the validity of the Stark broadening mechanism. Thus, there is presently no full satisfactory explanation for the shape and widths of the H I emission lines.

The curious double peaked structures of the H-α profiles bear some resemblance to those observed in the hot metal rich DA white dwarfs WD0621-376 and WD2211-495 (Holberg, private communication). In Figure 4.14 the NLTE emission core of H-alpha line of WD2214-249 is shown. The emission core in this star is seen to be cut by what appears to be a narrow off-center absorption core which gives the emission feature a bimodal structure. WD2211-495 is not known to have a companion and so explanations involving orbital motion are not relevant. It is conceivable the underling line structure in HS1136+6646 is a complex combination of a relatively narrow doubly peaked NLTE emission core and a broader emission line associated with the K7 companion and that changing appearance of the line in Figure 4.13 is due to a combination of these different components and the Doppler motion of the two stars. It would require additional time-resolved phase coverage of this feature to investigate this feature in more detail.

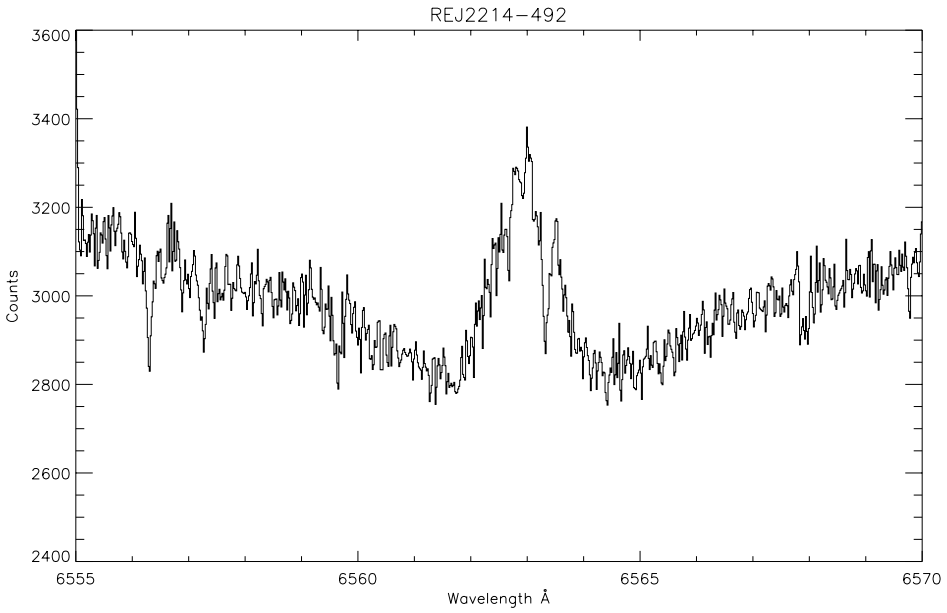

Figure 4.14: H-α emission line profile taken from the ESO Very Large Telescope showing a bimodal structure.

4.5 Magnetic Properties of HS1136+6646

Low amplitude 113.13 minute photometric modulations observed in HS1136 were hypothesized by Sing et al. (2004a) to be the result of spots on the WD surface at the magnetic poles rotating with the spin of the WD. Magnetic star spots are known to affect the photometric light curve of single magnetic WDs such as GD 356 and WD1953-011 (Brinkworth et al., 2004, 2005) where the spot, analogous to a sunspot, is an area of cooler temperature and lower luminosity. PCEBs also show modulations on the WD spin. They are also detected as periodic variations in the X-ray and EUV in V471 Tau, IN CMa, and RE 1016-053 (Barstow et al. 1992, Dobbie et al. 1999, & Vennes et al. 1997 respectively). The X-ray and EUV variability in these systems is attributed to wind accretion from the secondary star onto the magnetic poles of the WD, where emission is suppressed to do the absorption opacity of heavy elements. In order to search for possible spectral signatures of the magnetic spots or wind accretion, the TTAG *FUSE* spectra was re-reduced to have a sufficient time resolution to observe any effects, see §2.1.3. Along with the periodic motion, the O VI radial velocity curve seen in Figure 4.3 shows numerous abrupt departures from the normal orbital solution which can be upwards of ±40 to 50 km s^{-1}. Figure 4.15 highlights these radial velocity departures by subtracting the orbital solution, equation 4.4, and phasing the data on the double-peaked 224 minute low-amplitude modulation period observed in UBVRI photometry. The radial velocity variations phase with the observed photometric modulations, indicating that they are associated with the WD and the magnetic spots. Given that a WD with a 0.011 $R_{\odot}$ radius rotating with a period of approximately two hours would not produce ±40 to 50 km s^{-1} radial velocity deviations, the origin of these points most likely lies in unresolved Zeeman splitting changing the absorption line shape (see figure 4.4). Any non-symmetric line change in the O VI absorption features would be interpreted in our cross correlation technique as a change in radial velocity.

The absence of Zeeman split lines in the optical spectrum of HS1136 limits the magnetic field to <1 MG. The magnetic field strength, B, required to produce

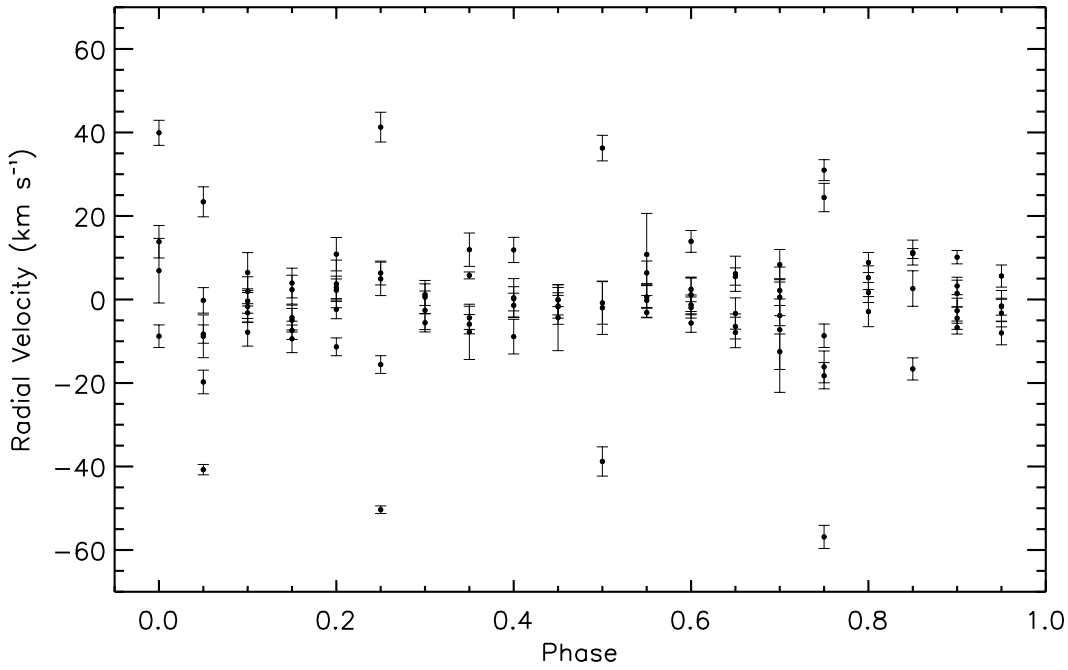

Figure 4.15: Radial velocity phased on the suspected white dwarf spin with the orbital variations removed. Note the large radial velocity deviations seen in Figure 4.3 group together at phases 0.0 to 0.1 and phase 0.5.

sufficient wavelength shifts, $\Delta\lambda$, for the O VI λ1032 absorption line to be shifted by $\sim$45 km s^{-1} is calculated using

$$\Delta\lambda = 4.7 \times 10^{-7} g B \lambda^2, \tag{4.10}$$

where B is measured in MG, g is the Landé g-factor, and the λ is measured in Å. Magnetic field strengths on the order of 450 kG could produce the largest radial velocity deviations, consistent with the limits imposed by optical spectra.

The O VI $\lambda\lambda$ 1032, 1038 resonance doublet variations seem reminiscent of a Si III absorption feature in V471 Tau interpreted by Bond et al. (2001) as a coronal mass ejection (CME) from the K2 secondary star passing across the line of sight to the WD. Interpreting the O VI variations in HS1136 as a CME would see unlikely

since its characteristics are distinctively different from those expected of circumstellar material. The radial velocity deviations are clearly tied to the WD rotation period (Figure 4.15) and are centered around orbital velocity variations of the WD. Moreover, the optical emission lines due to the secondary appear to vary as expected with the orbital phase and show no evidence of any intrinsic activity associated with the secondary.

CHAPTER 5

HS1136+6646 Discussion

5.1 Age of the Binary System

The cooling time of the hot white dwarf in HS1136+6646 is on the order of 2.4×10^5 or 6.4×10^5 years from Wood (1995), depending on which T_{eff} derived from Lyman or Balmer lines is used. This relatively short time indicates the HS1136+6646 system has just recently emerged from the post common-envelope phase (see Table 5.1). This system can be used to test aspects of common envelope (CE) evolution and help determine such parameters as the efficiency of the CE process and whether post-CE secondaries satisfy a normal main sequence mass-radius relation (Orosz et al., 1999). HS1136+6646 is similar in many respects to the well-known systems Feige 24 and V 471 Tau which are hot DA stars with dM2 and dK2 companions, respectively. Feige 24 shows a well-studied reflection effect while the DA in V471 Tau is too cool relative to its main sequence companion to produce an observable reflection effect.

5.2 The Past and Future Evolution of HS1136+6646

The high mass of the WD found for HS1136+6646 indicates a carbon and oxygen core, requiring that its progenitor reached the asymptotic giant branch (AGB) phase in its evolution before onset of the CE process. The nature of the WD progenitor

Table 5.1: Post-CE Systems Similar to HS1136+6646

System	Period (d)	a ($R_\odot$)	Components	T_{eff} (K)	WD Mass ($M_\odot$)	Post-CE age (yrs)
BE UMa	2.291	7.5	sdO/DAO+K5V	105,000	0.7	10^4
HS1136+6646	0.836	3.99	DAO+K7V	70,000	0.85	10^5
V 471 Tau	0.521	3.3	DA+K2V	34,000	0.84	10^7

can be estimated using the techniques described in Nelemans and Tout (2005). I used the stellar evolution model code TYCHO (Young and Arnett, 2005) to compute the core masses for different giant stars, using an initial metalicity of Z=0.02. The calculation was started on the Hayashi track (pre-MS track on a Hertzsprung-Russell diagram) and proceeded through the pre-MS phase (see Figure 5.1). Progenitor masses between 5.5 and 6 $M_\odot$ produced carbon-oxygen cores of 0.85 $M_\odot$ along the AGB. Given that other stellar models have calculated 0.86 $M_\odot$ core masses at the beginning of the thermal pulse-AGB phase for a 5 $M_\odot$ giant, (see Table 1 of Weidemann 2000), a more realistic range between 5-6 $M_\odot$ for the progenitor mass accounts for modeling differences. This mass range corresponds to a progenitor spectral type of B5-B7. The initial-to-final mass relationship for single white dwarf stars has recently been determined by Ferrario et al. (2005) using white dwarfs associated with open clusters. In general, Ferrario et al. (2005) finds a 0.85 $M_\odot$ white dwarf stars are produced by a 4 $M_\odot$ progenitors. Our higher 5-6 $M_\odot$ range for the progenitor of HS1136+6646 indicates that the common-envelope phase truncates the evolution of the progenitor star, resulting in a less massive white dwarf compared to those produced in single star evolution.

HS1136+6646, now in a detached state, will evolve toward shorter orbital periods via an angular momentum loss (AML) by emission of gravitational waves and magnetic braking (see appendix A and B). An upper estimate for the orbital decay time until HS1136+6646 becomes a semi-detached binary star (see Ritter 1986) is calculated by integrating the change in orbital period due to emission of gravitational waves,

$$\frac{dP}{dt} = -\frac{192\pi}{5}\frac{G^{5/3}}{c^5}\frac{M_{WD}M_{MS}}{(M_{WD}+M_{MS})^{1/3}}\left(\frac{2\pi}{P}\right)^{5/3}. \tag{5.1}$$

from the current period P_1 to the final semi-detached period, P_{sd}, where the variables have their usual meaning. P_{sd} can be estimated from Kepler's third law along with Roche geometry,

$$P_{sd} = 2\pi\left[\frac{R_{MS}^3}{GM_{MS}(1+q')f_2^3(q')}\right]^{1/2}, \tag{5.2}$$

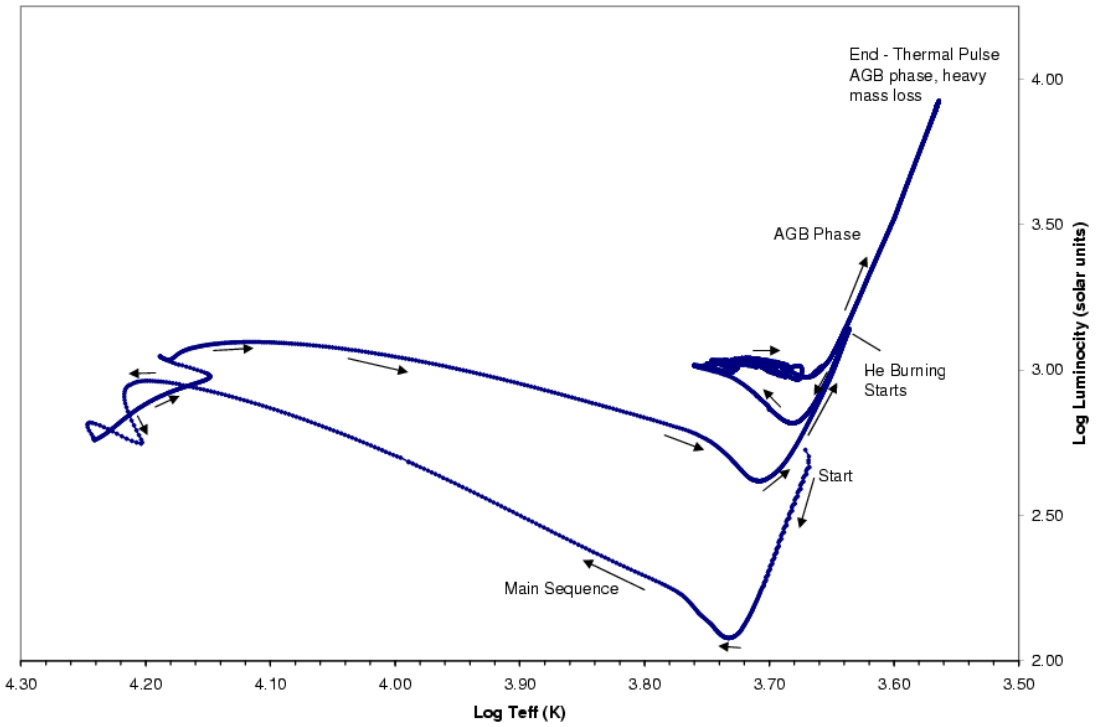

Figure 5.1: Hertzsprung-Russell diagram of a 5.0 $M_{\odot}$ star output from a TYCHO simulation. The simulation starts well before hydrogen burning and ends on the AGB.

where $q' = M_{WD}/M_{MS} = 1/q$ and $f_2(q)$ is the approximation from Paczyński (1971),

$$f_2(q) = \left(\frac{8}{81}\right)^{1/3}(1+q')^{-1/3}, \qquad q' > 1.25. \tag{5.3}$$

For the values taken from Table 1.2, P_{sd} is found to be 4.25 hours. Integrating Equation 5.1 yields the total time of the detached state t_d,

$$t_d = \frac{5c^5}{256G^{5/3}(2\pi)^{8/3}}\frac{(M_{WD}+M_{MS})^{1/3}}{M_{WD}M_{MS}}[P_1^{8/3} - P_{sd}^{8/3}]. \tag{5.4}$$

From the parameters listed in Table 1, t_d for HS1136+6646 is found to be 9.8×10^{10} years or $\log(t_d)$=10.99.

Angular momentum loss mechanisms involving magnetic braking can be calculated by either a classical (CMB) or reduced (RMB) prescription (see Schreiber and Gänsicke 2003 for a complete description). For CMB, magnetic braking is assumed to dominate over gravitational radiation and the time of the detached state becomes,

$$t_d = \frac{2.63 \times 10^{29} G^{2/3} M_{WD} R_\odot^{-4}}{(2\pi)^{10/3}(M_{WD}+M_{MS})^{1/3}}\left(\frac{R_\odot}{R_{MS}}\right)^2 [P_1^{10/3} - P_{sd}^{10/3}]. \tag{5.5}$$

The lifetime of the detached state assuming RMB is found from

$$t_d = \frac{3b}{4a}\left[\frac{(1+aP^{4/3})}{(P^{-4/3}+a)} - \frac{ln(1+aP^{4/3})}{a}\right]_{P_{sd}}^{P_1} \tag{5.6}$$

where

$$a = \left[\frac{M_\odot R_{dK}}{M_{dK}R_\odot}\right]^{1/5}\frac{K_W \omega_{crit}(M_{WD}+M_{MS})^{2/3}5c^5}{32(2\pi)^{4/3}G^{7/3}M_{WD}^2 M_{MS}^2} \tag{5.7}$$

and

$$b = \frac{5c^5(M_{WD}+M_{MS})^{1/3}}{96G^{5/3}(2\pi)^{8/3}M_{WD}M_{MS}}. \tag{5.8}$$

Using the values found in Andronov et al. (2003) for variables K_W and ω_{cirt} as well as a non-inflated secondary radius gives $\log(t_d)$ of 10.11 and 10.59 for CMB and RMB respectively. Taking into account magnetic braking reduces the semi-detached lifetime to less than one Hubble time in the case of classical AML, assuming the value $\log(\tau_0)$=10.11 (Ferreras et al., 2001). This makes HS1136+6646 a probable representative precursor to the current CV population.

5.3 Similar Post-Common Envelope Pre-Cataclysmic Variable Stars

It is of interest to compare HS1136+6646 with two other well-observed systems that, in many ways, appear to bracket it. These two systems are BE UMa (Ferguson et al. 1999 and references therein) and V 471 Tau (O'Brien et al. 2001 and references therein). All of these systems appear to have a recent post-CE origin and to contain a hot degenerate star with a main sequence K star. In Table 5.1, I list the system parameters and the characteristics of the degenerate stars. Since both BE UMa and V 471 Tau are eclipsing systems, the stellar parameters of the two components are relatively well determined.

Like HS1136+6646, BE UMa exhibits a very strong reflection effect, both in the continuum and emission lines (see Figure 5.2. The latter exhibits a host of first and second ionization-stages of CNO species as well as Si and Al. The key aspect of BE UMa is the high luminosity of the degenerate star, which has led Ferguson et al. (1999) to classify it as a borderline sdO/DAO star. By contrast, although the effective temperatures of the degenerate stars in HS1136+6646 and BE UMa are similar, the DAO star in HS1136+6646 is not nearly as luminous or dominant compared to its main sequence companion. Ferguson et al. (1999) estimate the gravity of the degenerate star in BE UMa to be 6.5, while the gravitational redshift of HS1136+6646 can be used to place a lower limit of 8.3 on the gravity of the DAO.

V 471 Tau, on the other hand, is almost completely dominated by the K star and shows no detectable reflection effect. However, low amplitude variations, similar to the ones detected in HS1136+6646 (§4.2.2), have been reported in the soft X-ray in V471 Tau (Jensen et al., 1986) and in the EUV from the hot white dwarf GD 394 (Dupuis et al., 2000). In both cases these modulations are believed to be associated with the rotation of the white dwarf. In particular, the magnetic 'spots' are thought to accrete high-z matter producing a non-uniform distribution of heavy elements on the stellar surface. Ellipsoidal variations cannot contribute to the main orbital photometric modulations seen in HS1136+6646, as the secondary does not fill its Roche lobe and should be tidally locked to the orbital period. Note the

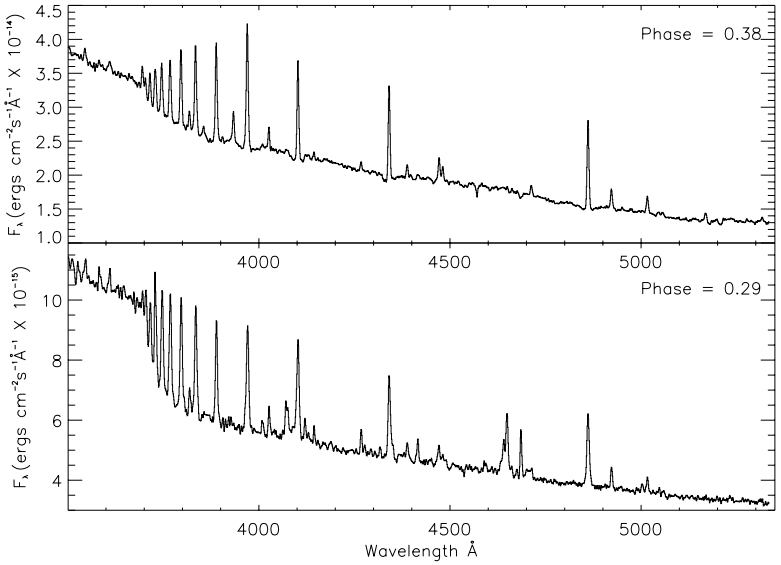

Figure 5.2: Optical spectra of the two youngest post-common envelope binaries, BE UMa (bottom) and HS1136+6646 (top).

study of V471 Tau is complicated by activity of the K star and the presence of mass ejection which propagates through the system. We have seen no evidence for any activity associated with the K star in HS1136+6646 in any of our observations. The broad double-peaked H I Balmer profiles are the only possible evidence we have for non-photospheric material in the system.

As with HS1136+6646, the four other youngest PCEBs UU Sge, V477 Lyr, KV Vel, and Be UMa, all have secondary stars out of thermal equilibrium (see Table 5.2

Table 5.2: Youngest Post-Common Envelope Binaries

Name	T_{eff} (K)	$M_{MS}[M_\odot]$	$R_{MS}[R_\odot]$	$R_{MS}/R^\dagger_{norm}$	Ref.
BE UMa	105,000	0.36	0.72	1.64	1
HS1136+6646	70,000	0.37	0.68	1.51	2
V 477 Lyr	60,000	0.15	0.46	1.76	3
UU Sge	57,000	0.29	0.53	1.45	4

† R_{MS}/R_{norm}: Ratio of the radius of the secondary star to its relaxed main sequence value.

References:(1)Ferguson et al. (1999), (2)Sing et al. (2004a), (3)Pollacco and Bell (1994),(4)Bell et al. (1994).

and Schreiber and Gänsicke 2003). All of these binaries have just emerged from the CE phase. The K5V secondary star of BE UMa is twice the expected radius. The large radii in these stars is a result of the thermal time-scale of stars envelope being longer than the time elapsed since the emersion from the CE phase (Ferguson et al., 1999). The thermal relaxation time-scale for the K7V star in HS1136+6646 is $\sim 10^6$ years, which is more than the estimated age of 2.4×10^5 years, resulting in an extended radius.

In Table 5.1 I also list the estimated post-CE ages for all three systems based on white dwarf cooling ages. In the case of BE UMa, the high luminosity of the degenerate star complicated the interpretation of its evolutionary status. It is clearly a very young system since Liebert et al. (1995) have detected a 3' nebula surrounding the star. For reasonable estimates of the expansion rate of the nebula, they find good agreement with the thermal age of the degenerate. V 471 Tau is clearly the oldest system of the three, but the thermal age of the DA is in apparent conflict with its being a member of the Hyades cluster (O'Brien et al., 2001).

5.4 Reconstructed Common-Envelope Efficiency

The classical α and alternative γ prescriptions for the common-envelope (CE) process relate the initial binary parameters, before the onset of the CE process, to the final post-CE values. These processes are characterized by the efficiencies, α and γ, assumed to be constants. An estimation of the efficiencies can be calculated by knowing the component masses and binary separations before and after the CE process. For HS1136+6646, the final post-CE parameters are well determined (see Table 1.2), but the initial mass of the primary and the initial separation have to be estimated.

Following Nelemans and Tout (2005), I assume the initial pre-CE separation of the binary is determined by finding the photospheric radius of a primary star at the time along the AGB phase when its core has grown to the mass observed for the white dwarf ($M_c = M_{WD}$). At this size, the photospheric radius is then assumed to

fill its Roche lobe, initiating mass transfer and the common-envelope process. The range of possible progenitors is calculated in §5.2 to have a mass range from 5 to 6 $M_\odot$, which I will call the low-mass and high-mass scenarios. Using these models, the radius of the progenitor star, R_g is estimated to be 3069 $R_\odot$ for the low-mass model and 2394 $R_\odot$ for the high-mass model. These values give an initial separation, a_i, of 3290 $R_\odot$ and 2537 $R_\odot$ respectively. The secondary mass is assumed not to change during the CE phase. The mass of the envelope, M_e, is assumed to be the difference between the WD progenitor giant mass, M_g, and the observed WD mass, M_{WD}.

In the classical prescription, solving for $\alpha\lambda$ in equation 1.2 results in a value of 0.18 in the low-mass scenario and 0.34 for the high mass scenario. The structure constant λ is usually taken to be a constant, typically 0.5 (de Kool et al., 1987), or incorporated with α as one free parameter, $\alpha\lambda$. Solving for γ from equation 1.4 results in a value of 1.28 for the low-mass scenario and 1.22 for the high-mass scenario. The errors in these efficiency values rest mostly with the uncertainty of initial progenitor star. As such, HS1136+6646 alone can not differentiate as to which is the better model for the CE process.

Comparing the efficiency values found here to other calculations by, $\alpha\lambda$ is found have a value similar to the most probable value found by Nelemans and Tout (2005), while λ is $\sim$0.25 smaller than the average they find. Note that Nelemans and Tout (2005) calculate $\alpha\lambda$ and γ for HS1136+6646, but it is unclear in the paper what values they use. Moreover, at the time of publication, Nelemans and Tout (2005) would have to rely on the values found in Sing et al. (2004a) or earlier estimations. These early values contained systematic errors, namely in radial velocity, which results in a much lighter WD mass than this work indicates.

5.5 Future Problems for HS1136+6646 to be Solved

HS1136+6646 is an intriguing yet challenging object for continued study. Future observations, which would significantly extend the work presented here include the following. A deep imaging search for the remnants of the common envelope phase and post-AGB phase would be possible, similar to the study done of BE UMa. As mentioned earlier, an expanding nebula has been detected around BE UMa, providing direct evidence for mass loss in the CE phase. The presence of a magnetic field could be directly detected with spectropolarimetric observations. A positive detection would help to establish a better estimate of the field strength and orbitally phased resolved observations could help place constraints on the field configuration. Such observations are well within the capabilities of instruments here at the UofA and time has been scheduled in 2005 Dec 31. The potential results of this observation will not be a part of this dissertation. Further high resolution spectroscopic observations of the structure of the Balmer H I lines are another candidate for further observations. Coverage of the line profiles as a function of orbital phase could help provide an understanding of the nature of this phenomena.

Theoretically, the bright reflection effect also opens up the possibility for atmospheric modeling of the secondary star, as was done by Ferguson (1983) for the similar post-common envelope binary, BE UMa. Such studies would probe the complex atmospheric structures of these objects which, among other interesting features, poses an inverted temperature profile.

A full non-local thermodynamic equilibrium line blanketed model atmospheric study of the UV data would also greatly enhance our understanding of the white dwarf in HS1136+6646. Preliminary work has shown these model atmospheres can give an effective temperature estimation independent of H I Lyman or Balmer line profile fits by analyzing the absorption strengths of highly ionized heavy elements. An extensive model atmospheric grid spanning a higher temperature, log g, and abundance range should ultimately provide an accurate temperature and heavy element abundance for HS1136+6646.

CHAPTER 6

Observations of Cataclysmic Variables V405 Aurigae and J0604+3344

6.1 V405 Aurigae

6.1.1 *FUSE* Observations of V405 Aurigae

Far Ultraviolet spectra (905-1195 Å) of V405 Aur were obtained with the *Far Ultraviolet Spectroscopic Explorer* (*FUSE*) satellite (Moos et al. 2000 during Cycle 4 observations, Table 6.1). These observations were designed to look for complex emission line behaviors related to interactions between the white dwarf in V405 Aur and its partial accretion disk. A total of 20 exposures were taken through the large (LWRS, 30" × 30") aperture in time tagged (TTG) mode between MJD 2452913.08758 and 2452913.59935 for a total exposure time of 22,800 s. Data from the 2003 observations were processed with the *FUSE* data reduction software (CalFUSE ver. 2.4.1 and ver. 3.0.6). The extracted spectra consist of four different instrument channels (separate optical paths with different mirrors and gratings) and two different instrumental sides (independent micro-channel plate detectors). The extracted spectra, excluding the LiF 1B channel containing "the worm", were concatenated and co-added to produce a spectrum with the highest possible signal-to-noise for line identification purposes. "The worm" is an artifact, seen in the spectra, produced by an obstruction of one or more grid wires lying 6 mm above the microchannel plate detectors. This causes a significant percentage of the light to be blocked out in the LiF 1B channel. In order to observe possible O VI and other line variations on the white dwarf spin and orbital period, we re-extracted the time-tagged spectra as a function of both phases.

Table 6.1: Log of V405 Aurigae *FUSE* Spectroscopic Observations

Exposure Name	MJD Start (JD-2,450,000)	MJD End (JD-2,450,000)	Exposure Time (seconds)	Orbital Phase
D0800101001	2913.08758	2913.11561	2422	0.56
D0800101901	2913.11590	2913.12695	955	0.67
D0800101003	2913.15425	2913.18488	2647	0.95
D0800101902	2913.18521	2913.19673	996	0.07
D0800101004	2913.20171	2913.20446	238	0.14
D0800101005	2913.22638	2913.25415	2400	0.36
D0800101903	2913.25447	2913.26647	1037	0.48
D0800101006	2913.27255	2913.27730	411	0.56
D0800101007	2913.29834	2913.32342	2167	0.77
D0800101904	2913.32373	2913.33613	1072	0.88
D0800101008	2913.33909	2913.35157	1079	0.97
D0800101009	2913.37021	2913.39269	1943	0.18
D0800101905	2913.39300	2913.40578	1105	0.28
D0800101010	2913.40789	2913.42558	1528	0.38
D0800101011	2913.44204	2913.46196	1722	0.59
D0800101906	2913.46225	2913.47541	1138	0.68
D0800101012	2913.48132	2913.49967	1586	0.81
D0800101013	2913.51362	2913.53124	1522	0.99
D0800101907	2913.53155	2913.54502	1164	0.09
D0800101014	2913.55101	2913.59935	4177	0.30

The exposure names beginning with D08001019 were taken during an occultation.

6.1.2 *FUSE* Spectrum of V405 Aurigae

The UV spectra of V405 Aur (Figure 6.1) lack continuum emission (the error in the continuum flux is larger than the measured flux) but contain broad O VI and C III emission-lines which can be attributed to the accretion disk (see below). While a broad O VI λ1032 resonance line appears in the spectra, the corresponding broad O VI λ1038 doublet line does not seem to be present and is probably too faint to detect. The small emission lines surrounding the narrow O VI λ1038 line are identified as C II λ1036.337, C II λ1037.018 and O I λ1039.230. The spectra also show a narrow emission-line component for the O VI resonance doublet $\lambda\lambda$1032, 1038 (Figure 6.2); but no He II λ1085 emission is evident. The other *FUSE* spectral lines, shown in Figures 6.2 and 6.1, were identified as airglow. The emission-line FUV spectra of V405 Aur closely resembles that seen in AM Her (Hutchings et al., 2002; Mauche and Raymond, 1998), having both narrow and broad emission-line components, although AM Her does not contain an accretion disk. The FWHM of the broad emission-lines seen in the *FUSE* spectrum of V405 Aur measure 4.5 Å corresponding to a disk broadening of 1100$\pm$50 km s^{-1} for the C III λ 1175 line.

Measurements of the O VI narrow emission-line components were performed in the Interactive Data Language (IDL) software package, recording empirical parameters, such as equivalent width, as well as those found from fitting the line to a Gaussian profile, which were used for measuring radial velocities. An eleven point, $\sim$0.06 Å, boxcar smooth was applied to the data, to increase the apparent signal-to-noise ratio. The SiC 2B and LiF 1A *FUSE* channels containing the O VI doublet were used to determine the radial velocity solution and exposure-to-exposure wavelength shifts were found to be negligible by measuring shifts in the airglow lines. Radial velocity and line flux measurements for the brighter O VI λ 1032 line were phased on the white dwarf spin period of 545.455 sec (Allan et al., 1996), but neither parameter produced an obvious modulation related to the spinning WD. Measurements of the O VI narrow emission-line components were phased on the orbital period. The resulting radial velocity curve is shown in Figure 6.3. We used the optical orbital

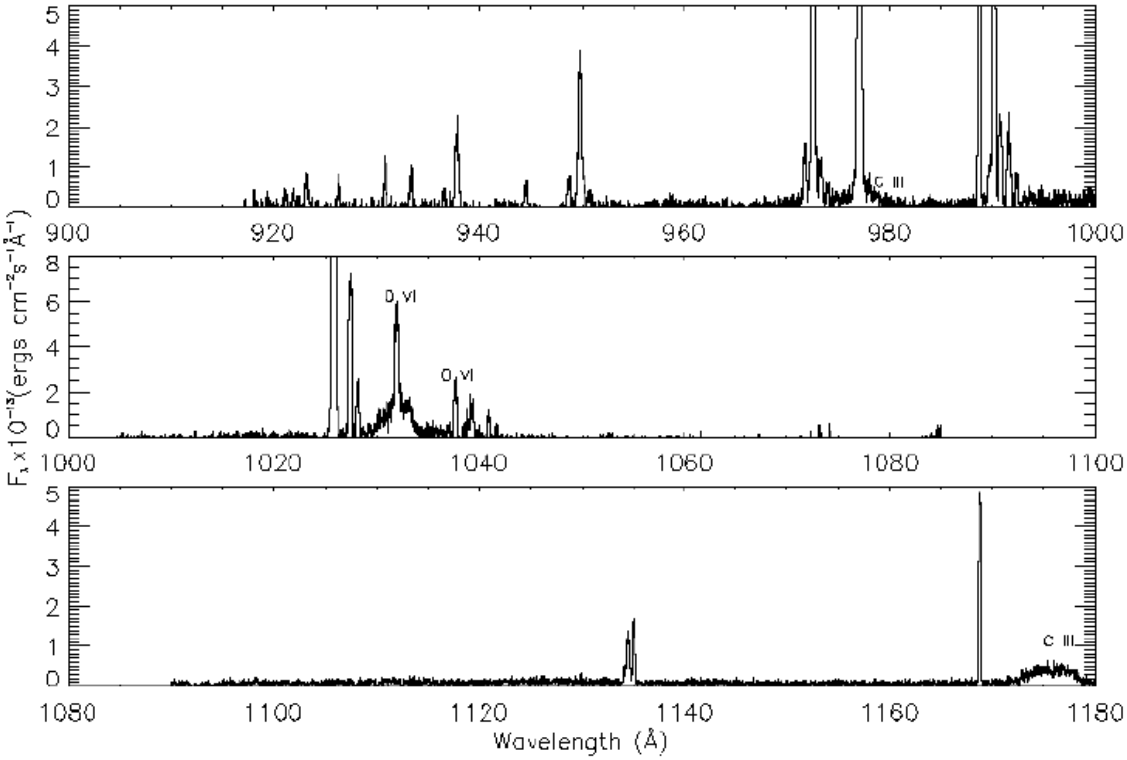

Figure 6.1: Coadded *FUSE* spectra of V405 Aurigae, smoothed over 0.04Å, showing broad and narrow emission-lines of O VI and broad C III emission lines. All other lines are terrestrial airglow.

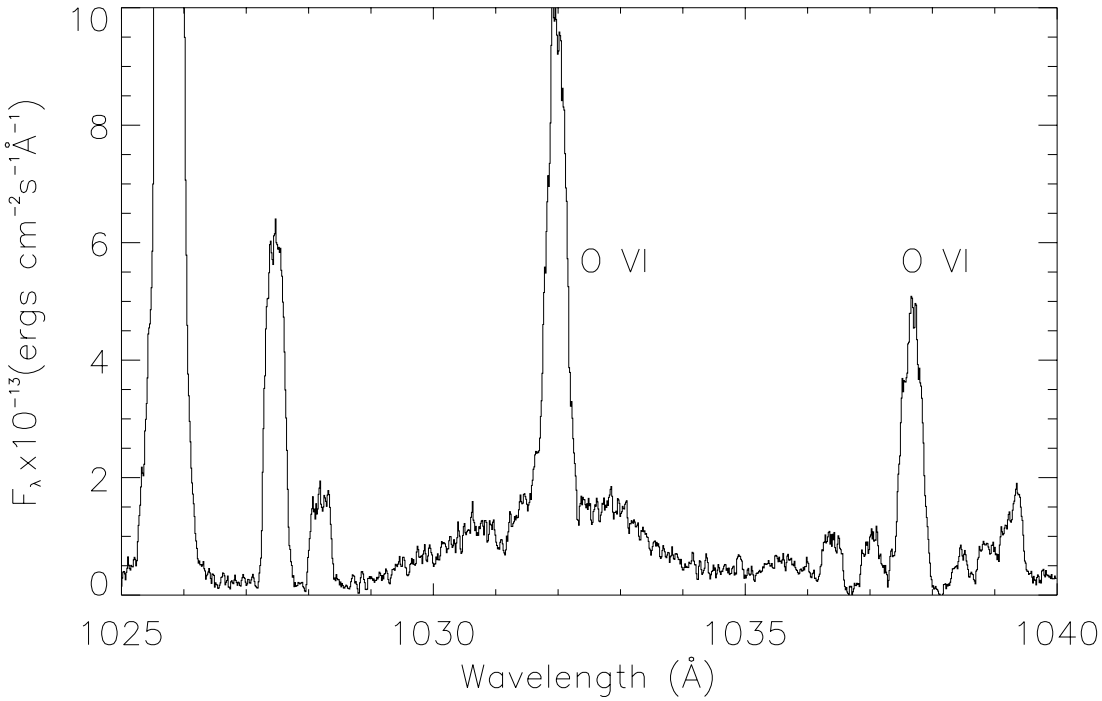

Figure 6.2: *FUSE* Spectra, smoothed over 0.04Å, showing resolved O VI $\lambda\lambda$ 1032, 1038 Å emission-lines. Note the broad component of the O VI λ1032 and the lack of continuum flux. All other lines are terrestrial airglow.

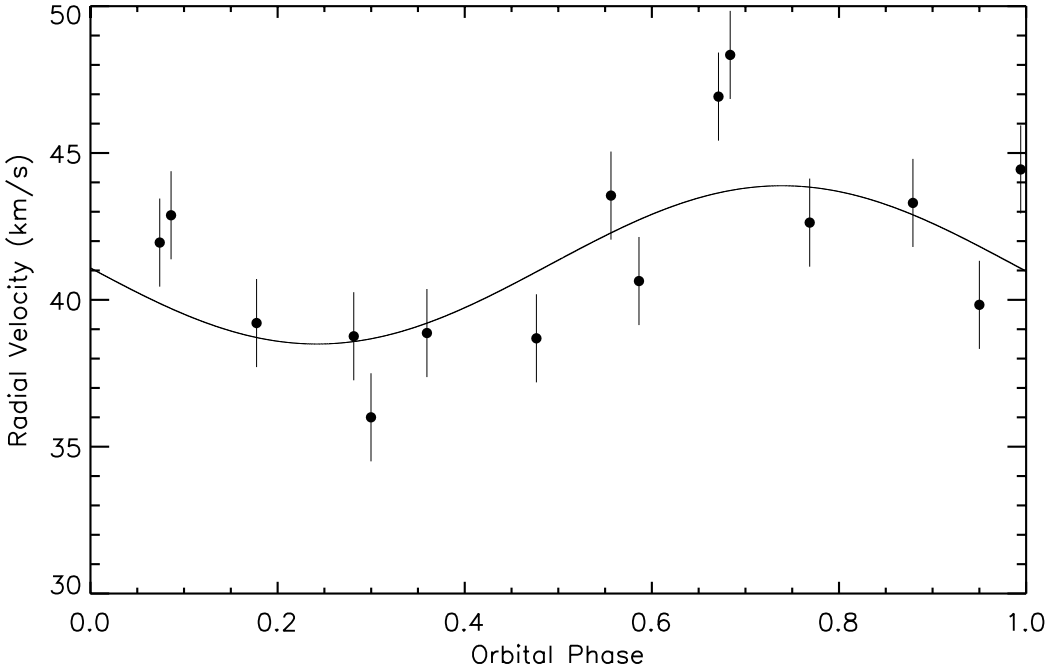

Figure 6.3: Radial Velocity curve for V405 Aurigae of the O VI 1032 narrow emission-line phased on the orbital period. The red-to-blue crossing of the fit is at ϕ=0.01 indicating correspondence with the motion of the white dwarf.

ephemeris from Szkody et al. (2000), (ϕ(HJD)=2,451,088.76164+0.1726196E) where E is the cycle count, in which they defined phase zero by a measured Hα red-blue crossing (ie., the red-to-blue crossing of the accretion disk/white dwarf), noting a zero phase difference of 0.23 between their observations and those of Haberl et al. (1994). The zero phase uncertainty in extrapolating the ephemeris from Szkody et al. (2000) to our epoch is 0.07. From our radial velocity results and by comparing our *FUSE* radial velocity curve of the O VI narrow emission-lines to the optical emission-line radial velocities reported by Haberl et al. (1994; where their zero phase corresponds to blue-to-red crossing), we find that the O VI narrow emission-lines phase, and thus can be attributed to, formation at or near the white dwarf.

A χ^2 fit of the radial velocity data was performed using a sinusoid of the form

$$V_{WD}(t) = \gamma + K_{WD} \sin\left[2\pi \frac{(t - T_0)}{P} - 2\pi\phi\right], \tag{6.1}$$

with the orbital parameters as listed in Table 1.3, where K_{WD} is the K velocity, P is the orbital period, T_0 and t are, respectively, the epoch and time, ϕ is the zero phase difference, and γ is the system gamma velocity. It should be noted that although the source of the zero phase difference between Haberl et al. (1994) and Szkody et al. (2000) is unknown and a similar discrepancy between our *FUSE* data and Szkody et al. (2000) is possible, our zero phase is within 0.01 of the value from Szkody et al. (2000). The mean value of our radial velocity measurements, 41.1±0.1 km s^{-1}, is in fair agreement with the systemic velocity of 31±2 km s^{-1} reported by Haberl et al. (1994). The possible discrepancy in this *FUSE* velocity can be attributed to the use of a large aperture, resulting in velocities that can not be precisely placed on an absolute scale. The difference might also be due to a bias imparted through comparison of optical disk emission lines (Haberl et al. 1994) and FUV lines. No obvious orbital correlation was seen in phasing radial velocity measurements of the FUV broad emission line components, although this was not a robust test due to the low signal-to-noise of these lines. The results of this analysis are contained in §6.4.

6.2 J06044+3344

6.2.1 61" Photometry of J06044+3344

Time resolved differential photometric observations of J0644 were obtained on 2005 January and 2005 March with the Steward Observatory 61" Kuiper Telescope located on Mt. Bigelow by E. M. Green. A NSF llick3 2048 x 2048 pixel CCD was used which has 0.15 "pixel−1 giving a 307×307 " field of view. The February data consisted of 45 sec exposures, 69 sec sampling time, through a Harris *R* filter. The March data consisted of 30 sec exposures through the *R* filter and 60 sec exposures through a Harris *B* filter giving a sampling time of 160.5 sec between two exposures

of the same filter. Standard calibration frames were obtained each night. The data were reduced using standard IRAF routines. Comparison stars in the field of view were used for differential photometry.

6.2.2 Bok Spectroscopic Observations of J0604+3344

I obtained spectroscopic observations of J0644+3344 in and out of eclipse were obtained on the Steward Observatory 2.4m Bok telescope, located on Kitt Peak, during a 2005 January 16-17 observing run. Spectra were obtained using the Boller and Chivens Spectrograph at the Ritchey-Chretien f/9 focus. A 1200×800 15 μm pixel CCD was used in combination with a 1st order 600 line/mm grating blazed at 3568 Å was used to record the spectra. With a 2.5 arcsec slit width, a typical spectral resolution of 5.5 Å was achieved at a reciprocal dispersion of 1.87 Å/pixel on the CCD. Typical exposure times of 300 seconds yielded characteristic S/N ratios of 60-70. Before each observation, the instrument was rotated to align the slit perpendicular to the horizon, minimizing the effects of atmospheric dispersion.

Standard Image Reduction and Analysis Facility (IRAF) routines were used to reduce the data. The wavelength calibration was established with He-Ar arc-lamp spectra, interpolated between exposures taken before and after each observation, to account for any small wavelength shifts that may occur while the telescope tracks an object. The spectra were flux calibrated using the Massey et al. (1988) spectrophotometric standard G191-B2B observed over a range of zenith angles covering the program star's airmass range.

6.3 Analysis of J06044+3344

Photometric coverage in the B and R bands show deep 1 to 1.2 magnitude primary eclipses of the hot primary star (see Figure 6.4). There also is considerable 'flickering' in the light curve, indicative of mass transfer, but no significant evidence of a secondary eclipse. With multiple night coverage of J0644+3344, the fundamental orbital period of the system was subsequently determined to be 6.46488± 0.00024

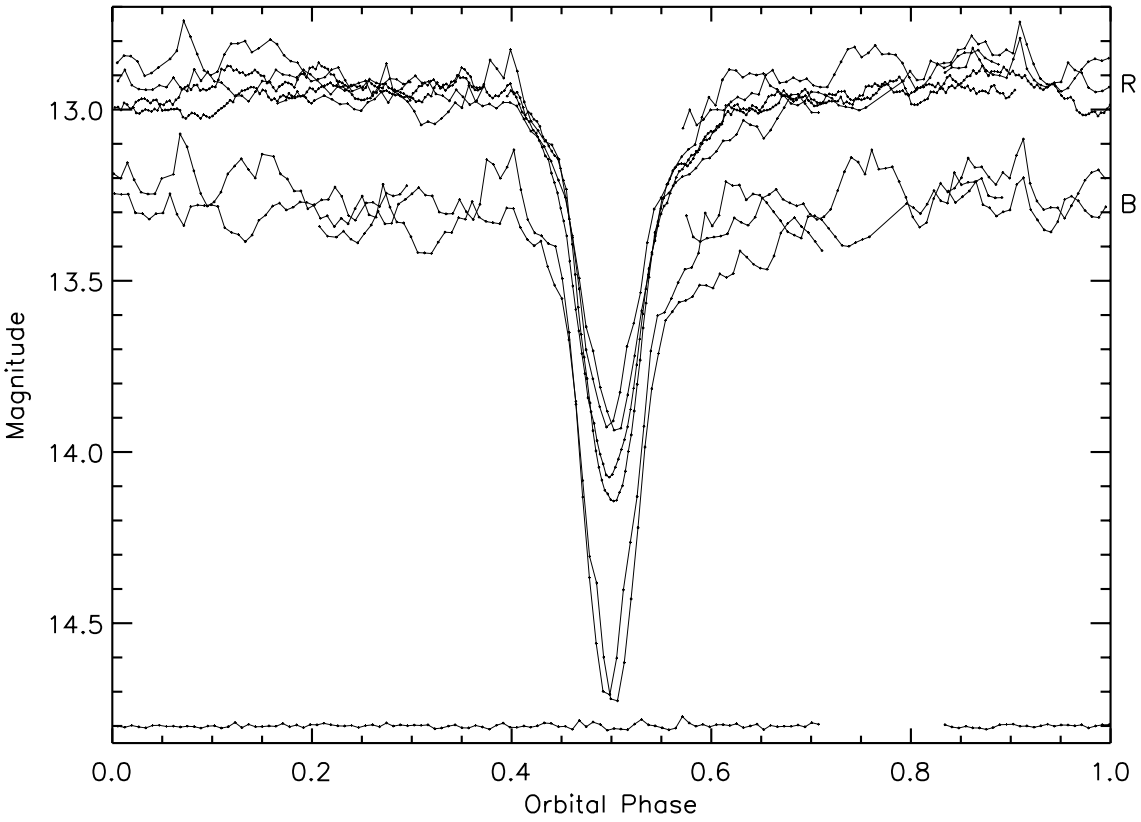

Figure 6.4: R and B photometry showing the eclipse of the primary star in J0604+3344. The points at the bottom of the plot are the R residuals for the 2005 March 02 data which characterize the standard differential photometry errors.

hrs, half the original estimate. It is also interesting to note that that R, J, H, and K photometric bands have a lower magnitude than the B band. The spectrum seen in Figure 6.5, however, indicates a continuum which rises toward shorter wavelengths. This may indicate there are significant contributions from the secondary star at longer wavelengths. If so, it would prove to be the first time a secondary star has been observed to dominate over the emission from the accretion disk at optical wavelengths for nova-like CVs. The current ephemeris for primary eclipse is given by, HJD = 3403.6255± 0.0007 + (0.26937 ±0.00001)(E-0.5).

Spectroscopically, the out-of-eclipse observations show a strong blue continuum with superimposed broad emission lines due to H I and He II (see Figure 6.5). The strongest emission line, He II λ4686, implies a very high level of excitation.

It diminishes relative to the H I lines during eclipse, further implying that a hot spot or inner line forming region is partially eclipsed. Note that strong He II lines occur in both polars and in high $\dot{M}$, longer period CVs. About 1/3 of the CVs known with strong He II λ4686 emission lines are non-magnetic (Szkody et al., 1990). The out-of-eclipse continuum of J0644+3344 is blue and resembles that of a hot white dwarf more than that of the accretion flux dominated continuum of a polar. During eclipse, the blue continuum dramatically flattens and weakens but the emission lines persist. The Doppler widths of the emission lines indicate velocities of 2200 km/s, typical of a CV accretion disk. Such a system would be expected to be show strong X-ray and/or EUV emission but the *ROSAT* detection (1RXSJ 064434.5+334451) at the position of this object (galactic latitude $b^{II} = +15°$) is relatively faint and unremarkable, apparently indicating that it was caught during the eclipse phase. An alternate, but unlikely, scenario in view of the other previously mentioned characteristics, is that the system is a polar and was in a low state when observed with *ROSAT*. However, we have only two months of observations and have not seen any typical low state type behavior. We interpret this system as a bright mass transfer binary containing an accretion disk, a hot degenerate sdB or WD primary, and a late K star secondary.

Our interpretation is supported by theoretical models (Howell et al., 2001) which predict a K star secondary based on a star filling its Roche lobe at a 6.5 hour orbital period. The lack of a noticeable secondary eclipse strongly supports a compact primary. Optical spectra contain few clues to the nature of the primary star, due to both the strength and persistence of the emission lines as well as the underlying continuum of the accretion disk. The 2MASS colors of J0644+3344 are similar to those of a non-interacting sdB + late F/early G composite system; however, since the accretion disk must be a significant contributor to the overall color, a hot white dwarf primary is also quite possible. The lack of a noticeable secondary eclipse in the R band could alternatively mean that the luminosity of the secondary is negligible with respect to a very much brighter primary + accretion disk. If the primary star is an sdB, then J0644+3344 would be a virtually unique example of a short period

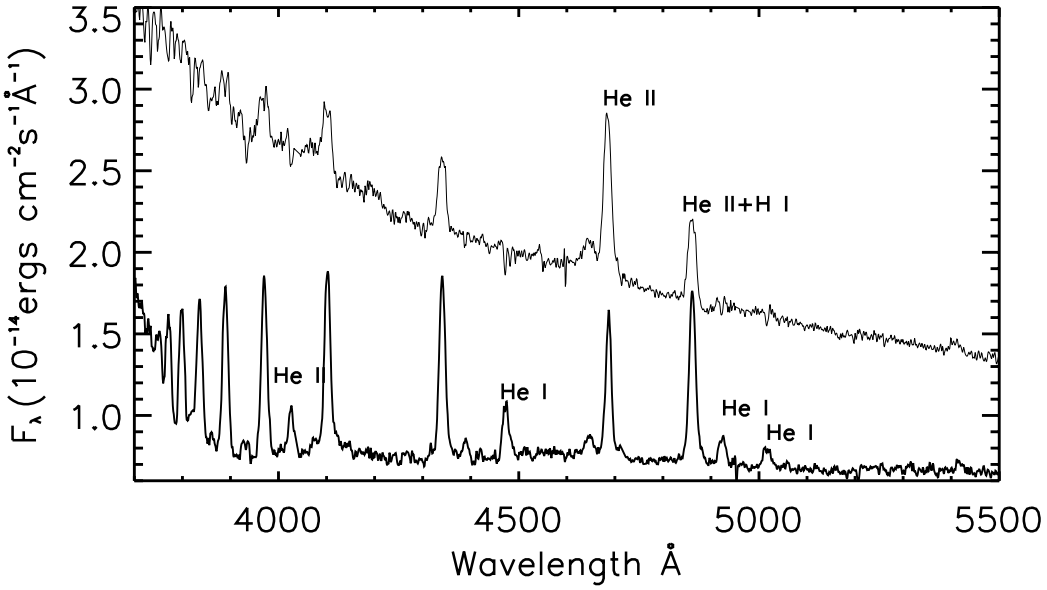

Figure 6.5: Optical spectra of J0644+3344 both in eclipse (bottom) and out (top), showing the H I Balmer series, He I, and He II. A 'Bowen fluorescence' feature is also visible at λ4640 Å caused by ionized carbon and nitrogen.

sdB/K star mass transfer binary. If primary turns out to be a hot white dwarf, then it would be by far the brightest example of an eclipsing CV binary. Either way, with future observations planned, we expect to be able to determine the masses and effective temperatures of each component as well as measure the orbital inclination more accurately then in previously studied eclipsing CV systems.

6.4 V405 Aurigae Results

The fit to the radial velocity measurements of the narrow O VI emission-line gives K_{wd} =2.5 +/− 0.5 km s^{-1}. Assuming different mass values for the primary and secondary star, a probable range of inclination, $< 5°$, for V405 Aur can be estimated using K_{wd} and Eq. (8) in Huber et al. (1998). The most likely theoretical value for the mass of the secondary star is 0.36 $M_{\odot}$ (Howell et al., 2001) however, we can not set any meaningful constraints on the white dwarf mass. Further evidence for a low inclination, $< 5°$, comes from the small K_{wd} amplitude and the single peaked nature of the broad optical and UV emission-lines which can be attributed to the accretion disk. The broad *FUSE* emission-lines observed (C III λ1175 and O VI λ1032) are single peaked, as well as those seen in the optical (Szkody et al., 2000) and in a *Hubble Space Telescope* UV spectrum (Figure 6.6 & 6.7).

In AM Her, the narrow O VI emission-line components are attributed to irradiation of the secondary star, as the line velocities phase with the secondary star and have FWHM values far less than those of a typical accretion disk (Hutchings et al., 2002). The narrow O VI emission-lines (FWHM $\sim$70 km s^{-1}) seen in V405 Aur are narrower than typical accretion disks as well, but their orbital phasing identifies their source at or near the white dwarf, not the secondary star. Since V405 Aur and AM Her have similar orbital periods and binary separations and possibly similar temperature WDs, the lack of irradiation producing narrow-lines in V405 Aur is likely due to shielding of the secondary star by the truncated accretion disk, or alternately, the ionization parameter (X-ray luminosity) could be too low as is the case with EX Hya (Mauche, 1999) due to the larger accretion regions in IPs.

Haberl et al. (1994) reported non-zero X-ray flux throughout the orbit of V405 Aur and detected modulations in the X-ray light curve on the white dwarf spin period. We, however, do not see such a modulation in the O VI emission-lines, line flux, or radial velocities on the spin period. A possible simple explanation could be that at such a low inclination, $\sim 5°$, no aspect changes of the O VI emission region are seen by the observer. In this scenario, the X-ray modulations would result from

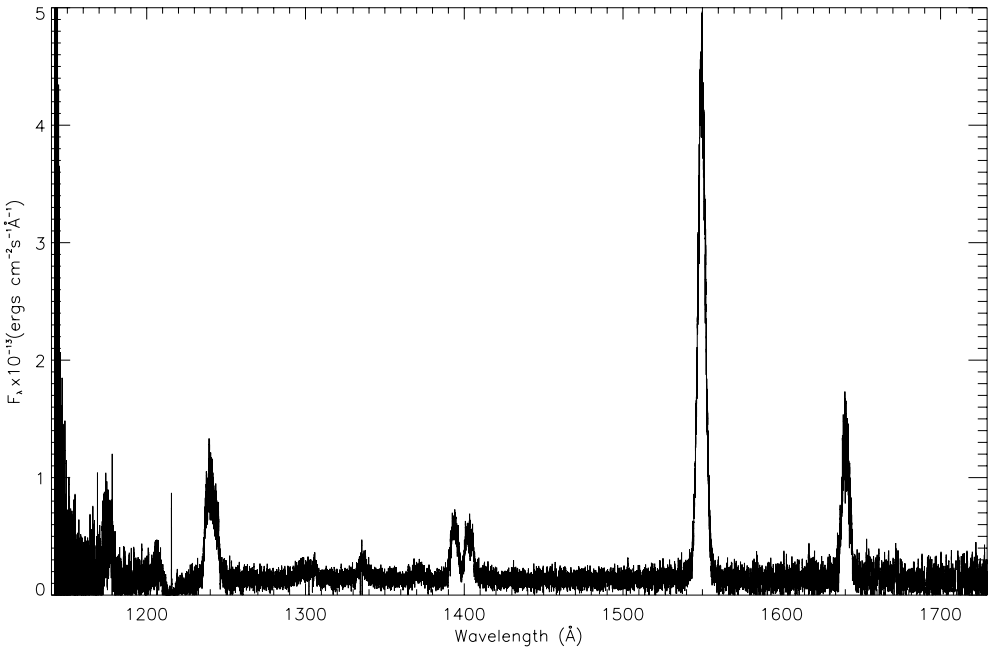

Figure 6.6: Hubble Space Telescope spectrum of V405 Aur showing N V, Si IV, C IV, and He II emission lines. This spectrum was obtained from the Multimission Archive at the Space Telescope Science Institute.

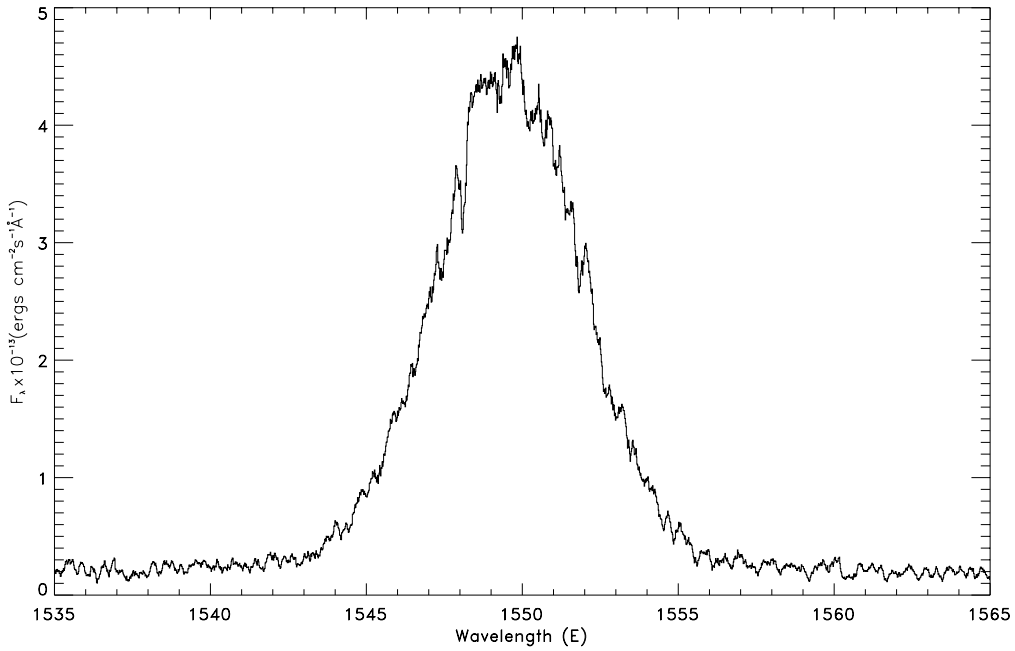

Figure 6.7: C IV doublet emission line profile of V405 Aur from the Figure 6.6 spectrum having a FWHM of 5.4 Å. The single peaked nature of the UV emission lines is additional evidence for a low binary inclination.

a partial self-eclipse of the magnetic pole(s), while the O VI emission region would form higher up the accretion column and not be eclipsed.

The flux ratio of the narrow O VI emission-lines (λ1032/λ1038) remained nearly constant at 2.2±0.4 (Figure 6.8), indicating their formation in an optically thin gas (Mauche, 1999). This interpretation is complicated, however, by the lack of an observable continuum flux in the V405 Aur *FUSE* spectra. It is possible that the *FUSE* spectra only detect the "tips" of the emission lines (especially O VI λ1038), making their ratio appear higher than it is. Indeed, a standard T_{eff} = 25,000 K, 0.55 $M_{\odot}$ DA white dwarf at the estimated 300 pc distance (Haberl 1994) would produce a continuum flux of 3×10^{-14} ergs cm^{-2} s^{-1} Å^{-1} at 1000 Å, well below the co-added *FUSE* flux detection limit (see Figure 1).

By fitting a black body curve to the Haberl et al. (1994) optical spectrum plus unpublished *IUE* spectrum (LWP31948 and LWP31949 which show an apparent continuum roll-off near 2500 Å) and making the assumption that the continuum in dominated by the accretion disk flux in the optical and UV regions, I estimate the accretion disk to have a maximum temperature of 11,000 K. At this temperature, the accretion disk is too cool to contribute to the continuum flux in the far-ultraviolet wavelength range. The FWHM accretion disk velocity measured from the broad C III λ1175 Å emission-line is $\sim$ 1100 km s^{-1} in agreement with FWHM velocities obtained from optical data. Accretion disk line widths for intermediate polars with truncated accretion disks range from 1400-1900 km s^{-1} (Mauche, 1999), indicating that V405 Aur contains a fairly typical truncated accretion disk in which the inner disk is destroyed by material threading along the magnetic field onto the white dwarf (see Belle et al. 2003).

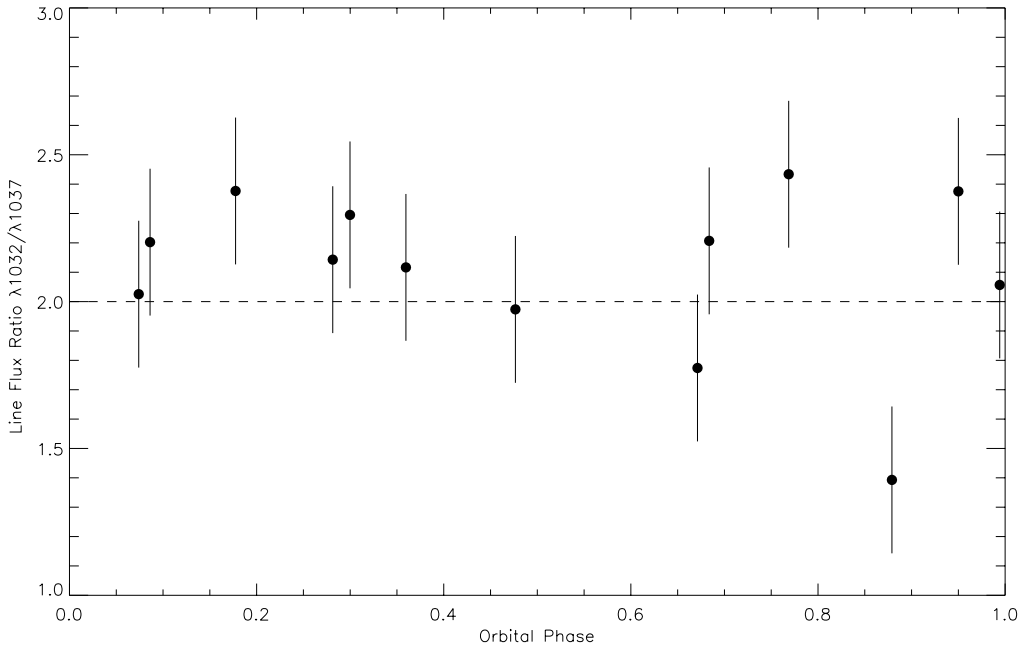

Figure 6.8: Line flux ratio of O VI λ1032/λ1038 vs. orbital phase. A value of 2.0 indicates an origin in optically thin gas.

CHAPTER 7

Conclusions

7.1 HS1136+6646

HS1136+6646 offers a unique opportunity to study a recently evolved common-envelope system which is relatively bright and nearby. We have presented new spectroscopic and photometric observations that characterize the binary parameters of HS1136+6646. These observations also show HS1136+6646 to be the second youngest post-CE system known having emerged of its CE phase only $\sim 10^5$ years ago. From analysis of the binary parameters, we find that HS1136+6646 has a K7V star that is out of thermal equilibrium. The photometric measurements reveal low amplitude 234 min modulations which are presumably due to the rotation of the white dwarf. Synthetic white dwarf model fits to the Balmer line profiles of the white dwarf in HS1136+6646 give an T_{eff} = 70,000 K and log g = 7.75. This temperature and gravity remains difficult to reconcile with the UV spectrum Lyman line results, T_{eff} =110,000 K and log g =7.00-7.5, as well as a log g = 8.29 calculated from the gravitational redshift of the WD.

In 2003 May, HS1136+6646 was observed by the *FUSE* spacecraft. These UV observations have provided nearly complete orbital coverage of the binary system and should allow a better determination of the white dwarf velocity curve. Cycle 12 observations with the *Space Telescope Imaging Spectrograph* (*STIS*) have also been obtained and analyzed. The echelle UV spectra from these observations have allowed the placement of the *FUSE* velocity for the white dwarf on an absolute scale, thus providing a gravitational redshift for the white dwarf and an accurate estimation of its mass.

Only about 30 Post-CE Pre-CV systems have well characterized orbital parameters (Schreiber and Gänsicke, 2003). With such a limited sample and the difficulty in

accurately parameterizing these binary systems, HS1136+6646 provides important bounds on Post-CE and Pre-CV evolutionary scenarios. *FUSE* observations, over nearly an entire orbital period, have made it possible to accurately determine the orbital solution of HS1136+6646, which had been proven difficult relying on optical data alone. The WD mass obtained is higher than all known PCEBs except V471 Tau, which has been suggested to have originated from a triple system (O'Brien et al., 2001).

7.2 V405 Aurigae

FUSE spectra of the magnetic cataclysmic variable V405 Aur show the system to be an intermediate polar having a low inclination. Radial velocity measurements of the narrow O VI emission-lines reveal their source to be on or near the magnetic poles of the white dwarf, not irradiation of the secondary as is the case with AM Her. Since the narrow O VI emission-lines show neither radial velocity nor line flux variations on the white dwarf spin period, their origin appears to be higher up in the near WD accretion columns, unlike the X-rays which may be spin modulated due to self-eclipse of the pole(s). Given the difficulty of observing the white dwarf in IP systems, far-ultraviolet emission-lines might prove to be the only method of more-or-less direct measurement of the compact object.

V405 Aur, PQ Gem, RXJ0512, and RXJ0757 all have magnetic field strengths at the low end of the distribution in polars and all four have fairly long orbital periods. The strength of the magnetic field in V405 Aur has been estimated to be > 5 MG by the flux ratio of hard bremsstrahlung to soft black body in the *ROSAT* band (Haberl and Motch, 1995). This value is consistent with the strongest field strengths of IPs as well as the lowest field strength polars such as AM Her which has a field strength of 14.5 MG (Bailey et al., 1991). These systems are likely to become AM Her-like polars as their orbital and spin periods synchronize in an astrophysically short time. With the average magnetic field strength of polars being much stronger than those in typical IPs, including these four possible transition objects, the question then

remains; where are the magnetically strong IPs which will become magnetically strong polars? Perhaps they undergo a rapid pre-polar to polar evolution becoming polars essentially at the same time they become mass transferring CVs.

7.3 J0604+3344

J0644+3344 is a bright new example of an eclipsing binary with ongoing mass transfer. Although the nature of the primary star is presently not well determined, being either a sdB or WD, it is a unique variable consisting of either the first example of a sdB/K mass transfer system, or possibly among the brightest eclipsing cataclysmic variables known. Future ground based observations are planned to determine the masses of the binary system and study the accretion disk structure. Ultimately, ultraviolet observations will probably be needed to unambiguously determine the spectral type of the primary star, and the ability to obtain such observations no longer exists.

APPENDIX A

Angular Momentum Loss Via Gravitational Waves

In this section I review the general relativistic calculations for angular momentum loss via gravitational waves in binary systems. The following prescription for angular momentum has been laid out in many fine sources in great detail, notably Misner et al. (1973), Shapiro and Teukolsky (1983), and more recently Hartle (2003).

The loss of angular momentum in a binary system is straightforward to calculate starting from the energy flux of gravitational waves given by the T_{0r} component of the stress energy tensor,

$$T_{0r} = \frac{32}{5}\frac{c^4}{G} < h^{TT}_{jk,0} h^{TT}_{jk,r} >, \tag{A.1}$$

where $h^{TT}_{jk,0}$ is the transverse-traceless component of the linearized metric perturbation,

$$h^{TT}_{jk,0} = \frac{2}{r}\frac{G}{c^4}\ddot{I}^{TT}(t - \frac{r}{c}), \tag{A.2}$$

I is the mass quadrapole moment,

$$I_{jk} = \sum_A m_A [x^A_j x^A_k - \frac{1}{3}\delta_{jk}(x^A)^2], \tag{A.3}$$

$$I^{TT}_{jk} = P_{jl}P_{km}I_{lm} + \frac{1}{2}P_{jk}(P_{lm}I_{lm}), \tag{A.4}$$

and P_{jk} is the projection tensor,

$$P_{jk} = \delta_{jk} - n_j n_k. \tag{A.5}$$

For simplification, we will calculate the mass quadrapole moment from a binary system in a circular orbit with a primary mass M_1, secondary mass M_2, primary separation a_1 and secondary separation a_2, where the distances, a, are from the respective binary components to the center of mass. All close binary systems are highly circular due to the strong tidal forces.

Evaluating equation 3 for the binary system gives three nonzero components,

$$I_{xx} = (M_1 a_1^2 + M_2 a_2^2) cos^2(\phi) + constant, \tag{A.6}$$

$$I_{yy} = -(M_1 a_1^2 + M_2 a_2^2) cos^2(\phi) + constant, \tag{A.7}$$

and

$$I_{xy} = (M_1 a_1^2 + M_2 a_2^2) sin^2(\phi), \tag{A.8}$$

where we have grouped all terms which are not time dependent into a constant. Equations A.6-A.8 can be further simplified with the definitions of reduced mass,

$$\mu = \frac{M_1 M_2}{M_1 + M_2}, \tag{A.9}$$

and $\phi = \Omega t$, into

$$I_{xx} = \frac{1}{2}\mu a^2 cos(2\Omega t) + constant, \tag{A.10}$$

$$I_{xx} = -\frac{1}{2}\mu a^2 cos(2\Omega t) + constant, \tag{A.11}$$

$$I_{xx} = \frac{1}{2}\mu a^2 sin(2\Omega t), \tag{A.12}$$

where Ω is the orbital angular velocity. From equations A.1, A.2, A.3 and A.4, the energy flux in terms of the mass quadrapole moment can be written as,

$$\frac{d^2 E}{dt d\Theta} = \frac{1}{8\pi}\frac{G}{c^5} < \dddot{I}_{jk}^{TT} \dddot{I}_{jk}^{TT} >, \tag{A.13}$$

where $\dddot{I}_{jk}^{'}$ is the third derivative of the mass quadrapole moment. Integration of equation A.13 yields the luminosity of the gravitational waves,

$$L_{GW} = \int T^{0r} r^2 d\Theta, \tag{A.14}$$

$$L_{GW} = \frac{1}{5}\frac{G}{c^5} < \ddot{I}_{jk} \ddot{I}_{jk} > . \tag{A.15}$$

Substituting in equations A.10, A.11 and A.12 into equation A.15 gives the luminosity in terms of the parameters of the binary system,

$$L_{GW} = \frac{32}{5}\frac{G^4}{c^5}\frac{M^2 \mu}{a^4}, \tag{A.16}$$

where $a = a_1 + a_2$. Loosing energy in a binary system leads to the two stars spiraling in toward each other. Since period measurements in a binary system are much more precise than a separation measurements, it is useful to calculate the decrease in period due to the loss of energy from gravitational waves. The energy of the binary system is simply the kinetic energy plus the potential energy,

$$E = \frac{1}{2}(M_1 a_1 + M_2 a_2)\Omega^2 - \frac{GM_1 M_2}{a} = -\frac{1}{2}\frac{G\mu M}{a}. \tag{A.17}$$

From Kepler's third law,

$$\Omega^{2/3} = \frac{GM}{a}. \tag{A.18}$$

and using equation A.17 we get,

$$-\frac{1}{2}\Omega^{2/3} = -\frac{GM}{2a} = E. \tag{A.19}$$

Taking the derivative of equation A.19 gives,

$$-\frac{1}{3}\Omega^{-1/3} = \frac{dE}{d\Omega}, \tag{A.20}$$

which can be rewritten in terms of the orbital period P,

$$\frac{1}{P}\frac{dP}{dt} = -\frac{3}{2}\frac{dE}{E}, \tag{A.21}$$

and in terms of the binary parameters,

$$\frac{dP}{dt} = -\frac{96}{5}\frac{G^3}{c^5}\frac{M^2\mu}{a^4}P, \tag{A.22}$$

or

$$\frac{dP}{dt} = -\frac{192\pi}{5}\frac{G^{5/3}}{c^5}\frac{M_1 M_2}{(M_1 + M_2)^{1/3}}(\frac{2\pi}{P})^{5/3}. \tag{A.23}$$

Integrating Equation A.23, gives the decay time from an initial period to a final value.

APPENDIX B

Angular Momentum Loss Via Magnetic Braking

In this section, I review the mechanism of magnetic braking in close binary systems. Magnetic braking is thought to be a key angular momentum loss (AML) mechanism for post-common envelope and cataclysmic variable binary stars being a much more efficient loss mechanism than gravitational waves alone can produce. For instance, steady angular momentum loss is the only way the mass transfer can occur in long-lived cataclysmic variables. Mass transfer from a less massive secondary star to a more massive primary star causes the orbital separation to increase, detaching the secondary from its Roche lobe, and ultimately halting mass transfer. Steady orbital angular momentum loss counteracts this effect, keeping the secondary filling its Roche lobe and steady mass transfer continuing.

Single stars, such as our sun, loose rotational angular momentum from the interaction of a star's wind with its magnetic field. The ionized gas particles in a stellar wind are emitted from a star at high velocities. These stellar wind particles travel away from the star along the long arms of the magnetic field. The magnetic field lines are tied back to the star effectively placing a torque on the star, reducing its rotational angular momentum. This angular momentum loss mechanism is thought to occur in binary systems as well, although with an additional effect. In a close binary system, tidal interactions force the secondary star to co-rotate with the orbital period. Thus, a decrease in the rotational angular momentum of the secondary star is transfered instead to a decrease in orbital angular momentum of the binary system, causing the binary system to contract. Following Rappaport et al. (1983), the AML from such a scenario can be estimated using a correlation between equatorial rotation velocity and age. In main sequence stars around one

$M_\odot$, Smith (1979) expressed the correlation as,

$$v_e = f \times 10^{14}\ t_o^{-0.5}\ cm\ s^{-1}, \tag{B.1}$$

where v_e is the equatorial velocity, f is a constant whose value is around unity, and t_o is the stars main sequence age. A braking torque, τ_{mb}, can be inferred from Equation B.1,

$$\tau_{mb} = -0.5 \times 10^{-28} f^{-2}\ k^2\ M\ R^4 \omega^3 dyn\ cm, \tag{B.2}$$

where ω is the rotational angular frequency and k is a structure constant that yield the moment of inertia for the star ($I = kMR^2$). Equation B.2 is usually parameterized with an index γ. For binary systems the resulting loss of angular momentum can be expressed as,

$$\frac{d\mathbf{J}}{dt} = -3.8 \times 10^{-30} M_{sec} R_\odot^4 \left[\frac{R_{sec}}{R_\odot}\right]^\gamma \left[\frac{2\pi}{P}\right]^3, \tag{B.3}$$

where R_{sec} is the radius of the secondary, M_{sec} is the secondary mass and P is the orbital period. Values of γ=2.0 are typically used in the context of cataclysmic variables. When the secondary star becomes fully convective, the magnetic field lines are no longer anchored to a radiative core and are free to rise to the surface of the star. The effect would be to stop the magnetic dynamo ultimately responsible for the stellar wind, halting AML.

REFERENCES

Allan, A., K. Horne, C. Hellier, K. Mukai, H. Barwig, P. J. Bennie, and R. W. Hilditch (1996). The spin period of the intermediate polar RX J0558+53. *MNRAS*, **279**, pp. 1345–1348.

Andronov, N., M. Pinsonneault, and A. Sills (2003). Cataclysmic Variables: An Empirical Angular Momentum Loss Prescription from Open Cluster Data. *ApJ*, **582**, pp. 358–368. doi:10.1086/343030.

Bailey, J., L. Ferrario, and D. T. Wickramasinghe (1991). Cyclotron features in the infrared spectrum of AM Herculis. *MNRAS*, **251**, pp. 37P–40P.

Barstow, M. A., M. R. Burleigh, N. P. Bannister, J. B. Holberg, I. Hubeny, F. C. Bruhweiler, and R. Napiwotzki (2001). Heavy Elements in DA White Dwarfs. In *ASP Conf. Ser. 226: 12th European Workshop on White Dwarfs*, pp. 128–+.

Barstow, M. A., S. A. Good, M. R. Burleigh, I. Hubeny, J. B. Holberg, and A. J. Levan (2003). A comparison of DA white dwarf temperatures and gravities from FUSE Lyman line and ground-based Balmer line observations. *MNRAS*, **344**, pp. 562–574.

Barstow, M. A., J. H. M. M. Schmitt, J. C. Clemens, J. P. Pye, M. Denby, A. W. Harris, and G. S. Pankiewicz (1992). ROSAT sky survey observations of the eclipsing binary V471 Tauri. *MNRAS*, **255**, pp. 369–378.

Belczynski, K., T. Bulik, and A. J. Ruiter (2005). New Constraints on Type Ia Supernova Progenitor Models. *ApJ*, **629**, pp. 915–921. doi:10.1086/431578.

Bell, S. A., D. L. Pollacco, and R. W. Hilditch (1994). Direct Optical Observations of the Secondary Component of Uu-Sagittae. *MNRAS*, **270**, pp. 449–+.

Belle, K. E., S. B. Howell, E. M. Sion, K. S. Long, and P. Szkody (2003). Hubble Space Telescope Space Telescope Imaging Spectrograph Spectroscopy of the Intermediate Polar EX Hydrae. *ApJ*, **587**, pp. 373–383. doi:10.1086/368180.

Bergeron, P., F. Wesemael, and A. Beauchamp (1995). Photometric Calibration of Hydrogen- and Helium-Rich White Dwarf Models. *PASP*, **107**, pp. 1047–+.

Bessell, M. S. and J. M. Brett (1988). JHKLM photometry - Standard systems, passbands, and intrinsic colors. *PASP*, **100**, pp. 1134–1151.

Bond, H. E., D. J. Mullan, M. S. O'Brien, and E. M. Sion (2001). Detection of Coronal Mass Ejections in V471 Tauri with the Hubble Space Telescope. *ApJ*, **560**, pp. 919–927. doi:10.1086/322980.

Boughn, S. and R. Crittenden (2004). A correlation between the cosmic microwave background and large-scale structure in the Universe. *Nature*, **427**, pp. 45–47.

Brinkworth, C. S., M. R. Burleigh, G. A. Wynn, and T. R. Marsh (2004). Photometric variability of the unique magnetic white dwarf GD 356. *MNRAS*, **348**, pp. L33–L37. doi:10.1111/j.1365-2966.2004.07538.x.

Brinkworth, C. S., T. R. Marsh, L. Morales-Rueda, P. F. L. Maxted, M. R. Burleigh, and S. A. Good (2005). Rotational period of WD 1953-011- a magnetic white dwarf with a star-spot. *MNRAS*, **357**, pp. 333–337. doi:10.1111/j.1365-2966.2005.08649.x.

Burwitz, V., K. Reinsch, K. Beuermann, and H.-C. Thomas (1996). A new soft intermediate polar: RX J0512.2-3241 in Columba. *A&A*, **310**, pp. L25–L28.

Carpenter, J. M. (2001). Color Transformations for the 2MASS Second Incremental Data Release. *AJ*, **121**, pp. 2851–2871.

Clarke, D. (2002). String/Rope length methods using the Lafler-Kinman statistic. *A&A*, **386**, pp. 763–774. doi:10.1051/0004-6361:20020258.

de Kool, M., E. P. J. van den Heuvel, and E. Pylyser (1987). An evolutionary scenario for the black hole binary A0620-00. *A&A*, **183**, pp. 47–52.

Dobbie, P. D., M. A. Barstow, M. R. Burleigh, and I. Hubeny (1999). Opacities along the line of sight to and in the atmosphere of the white dwarf in the close detached DAO+dM binary ¡ASTROBJ¿RE J0720-318¡/ASTROBJ¿. *A&A*, **346**, pp. 163–174.

Dupuis, J., P. Chayer, S. Vennes, D. J. Christian, and J. W. Kruk (2000). Adding More Mysteries to the DA White Dwarf GD 394. *ApJ*, **537**, pp. 977–992.

Eaton, N., P. W. Draper, and A. Allan (2001). PHOTOM: A Photometry Package, Starlink User Note. p. 45.12.

Ferguson, D. H. (1983). The emission line spectra of cataclysmic variable accretion disks. *Ph.D. Thesis*.

Ferguson, D. H. and T. A. James (1994). The spectacular emission-line reflection effect of BE Ursae Majoris. *ApJS*, **94**, pp. 723–747.

Ferguson, D. H., J. Liebert, S. Haas, R. Napiwotzki, and T. A. James (1999). Masses and Other Parameters of the Post-Common Envelope Binary BE Ursae Majoris. *ApJ*, **518**, pp. 866–872.

Ferrario, L., D. Wickramasinghe, J. Liebert, and K. A. Williams (2005). The open-cluster initial-final mass relationship and the high-mass tail of the white dwarf distribution. *MNRAS*, **361**, pp. 1131–1135. doi:10.1111/j.1365-2966.2005.09244.x.

Ferreras, I., A. Melchiorri, and J. Silk (2001). Setting new constraints on the age of the Universe. *MNRAS*, **327**, pp. L47–L51. doi:10.1046/j.1365-8711.2001.04979.x.

Good, S. A., M. A. Barstow, J. B. Holberg, D. K. Sing, M. R. Burleigh, and P. D. Dobbie (2004). Comparison of the effective temperatures, gravities and helium abundances of DAO white dwarfs from Balmer and Lyman line studies. *MNRAS*, **355**, pp. 1031–1040. doi:10.1111/j.1365-2966.2004.08406.x.

Haberl, F. and C. Motch (1995). New intermediate polars discovered in the ROSAT survey: two spectrally distinct classes. *A&A*, **297**, pp. L37+.

Haberl, F., J. R. Throstensen, C. Motch, A. Schwarzenberg-Czerny, M. Pakull, A. Shambrook, and W. Pietsch (1994). Discovery of the new intermediate polar RX J0558.0+5353. *A&A*, **291**, pp. 171–180.

Handler, G. (1998). A search for pulsations among low-mass DAO white dwarfs. *A&A*, **339**, pp. 170–172.

Hartle, J. B. (2003). *Gravity : an introduction to Einstein's general relativity*. Gravity / James B. Hartle. San Francisco, CA, USA: Addison Wesley, ISBN 0-8053-8662-9, 2003, XXII + 582 pp.

Heber, U., S. Dreizler, and H.-J. Hagen (1996). On the hot ends of the white dwarf spectral sequences: Hot white dwarfs containing helium from the Hamburg-Schmidt survey. *A&A*, **311**, pp. L17–L20.

Hoard, D. W., S. Wachter, L. L. Clark, and T. P. Bowers (2002). Infrared Properties of Cataclysmic Variables in the 2 Micron All-Sky Survey Second Incremental Data Release. *ApJ*, **565**, pp. 511–538. doi:10.1086/324499.

Holberg, J. B., D. Sing, M. A. Barstow, and S. Good (2001). HS 1136+6646: A New Short Period DAO + dMe System. In *Astronomische Gesellschaft Meeting Abstracts*, pp. 106–+.

Howell, S. B., M. E. Everett, J. L. Tonry, A. Pickles, and C. Dain (2003). Photometric Observations Using Orthogonal Transfer CCDs. *PASP*, **115**, pp. 1340–1350.

Howell, S. B., L. A. Nelson, and S. Rappaport (2001). An Exploration of the Paradigm for the 2-3 Hour Period Gap in Cataclysmic Variables. *ApJ*, **550**, pp. 897–918.

Hubeny, I. and T. Lanz (1995). Non-LTE line-blanketed model atmospheres of hot stars. 1: Hybrid complete linearization/accelerated lambda iteration method. *ApJ*, **439**, pp. 875–904.

Huber, M. E., S. B. Howell, D. R. Ciardi, and R. Fried (1998). Time-resolved Photometry and Spectroscopy of the Cataclysmic Variable V592 Cassiopeiae. *PASP*, **110**, pp. 784–793.

Hutchings, J. B., A. W. Fullerton, A. P. Cowley, and P. C. Schmidtke (2002). Far Ultraviolet Spectroscopic Explorer 900-1200 Å Spectroscopy of AM Herculis. *AJ*, **123**, pp. 2841–2846. doi:10.1086/340080.

James, C. H., G. Ramsay, M. C. Mark Cropper, and G. Branduardi-Raymont (2002). X-ray spectroscopy of the intermediate polar PQ Gem. *MNRAS*, **336**, pp. 550–558. doi:10.1046/j.1365-8711.2002.05772.x.

Jensen, K. A., J. H. Swank, R. Petre, E. F. Guinan, E. M. Sion, and H. L. Shipman (1986). EXOSAT observations of V471 Tauri - A 9.25 minute white dwarf pulsation and orbital phase dependent X-ray dips. *ApJ*, **309**, pp. L27–L31.

Kemp, J., J. Patterson, J. R. Thorstensen, R. E. Fried, D. R. Skillman, and G. Billings (2002). Rapid Oscillations in Cataclysmic Variables. XV. HT Camelopardalis (=RX J0757.0+6306). *PASP*, **114**, pp. 623–629.

Landolt, A. U. (1992). UBVRI photometric standard stars in the magnitude range 11.5-16.0 around the celestial equator. *AJ*, **104**, pp. 340–371.

Leibundgut, B. (2001). Cosmological Implications from Observations of Type Ia Supernovae. *ARA&A*, **39**, pp. 67–98. doi:10.1146/annurev.astro.39.1.67.

Liebert, J., R. W. Tweedy, R. Napiwotzki, and M. S. Fulbright (1995). Be Ursae Majoris: Precataclysmic binary system and planetary nucleus. *ApJ*, **441**, pp. 424–428.

Livne, E. (1990). Successive detonations in accreting white dwarfs as an alternative mechanism for type I supernovae. *ApJ*, **354**, pp. L53–L55. doi:10.1086/185721.

Marsh, T. R. and K. Horne (1988). Images of accretion discs. II - Doppler tomography. *MNRAS*, **235**, pp. 269–286.

Massey, P., K. Strobel, J. V. Barnes, and E. Anderson (1988). Spectrophotometric standards. *ApJ*, **328**, pp. 315–333.

Mauche, C. W. (1999). ORFEUS II and IUE Spectroscopy of EX Hydrae. *ApJ*, **520**, pp. 822–832. doi:10.1086/307498.

Mauche, C. W. and J. C. Raymond (1998). ORFEUS II Far-Ultraviolet Spectroscopy of AM Herculis. *ApJ*, **505**, pp. 869–875. doi:10.1086/306185.

Misner, C. W., K. S. Thorne, and J. A. Wheeler (1973). *Gravitation*. San Francisco: W.H. Freeman and Co., 1973.

Mobasher, B. (2002). *HST Data Handbook: Introduction to Reducing HST Data, Volume 1, Version 4.0*. User's Guide, Hubble Space Telescope, January 2002. Edited by Bahram Mobasher. Baltimore: Space Telescope Science Institute.

Monet, D. G., S. E. Levine, B. Canzian, H. D. Ables, A. R. Bird, C. C. Dahn, H. H. Guetter, H. C. Harris, A. A. Henden, S. K. Leggett, H. F. Levison, C. B. Luginbuhl, J. Martini, A. K. B. Monet, J. A. Munn, J. R. Pier, A. R. Rhodes, B. Riepe, S. Sell, R. C. Stone, F. J. Vrba, R. L. Walker, G. Westerhout, R. J. Brucato, I. N. Reid, W. Schoening, M. Hartley, M. A. Read, and S. B. Tritton (2003). The USNO-B Catalog. *AJ*, **125**, pp. 984–993.

Moos, H. W., W. C. Cash, L. L. Cowie, A. F. Davidsen, A. K. Dupree, P. D. Feldman, S. D. Friedman, J. C. Green, R. F. Green, C. Gry, J. B. Hutchings, E. B. Jenkins, J. L. Linsky, R. F. Malina, A. G. Michalitsianos, B. D. Savage, J. M. Shull, O. H. W. Siegmund, T. P. Snow, G. Sonneborn, A. Vidal-Madjar, A. J. Willis, B. E. Woodgate, D. G. York, T. B. Ake, B.-G. Andersson, J. P. Andrews, R. H. Barkhouser, L. Bianchi, W. P. Blair, K. R. Brownsberger, A. N. Cha, P. Chayer, S. J. Conard, A. W. Fullerton, G. A. Gaines, R. Grange, M. A. Gummin, G. Hebrard, G. A. Kriss, J. W. Kruk, D. Mark, D. K. McCarthy, C. L. Morbey, R. Murowinski, E. M. Murphy, W. R. Oegerle, R. G. Ohl, C. Oliveira, S. N. Osterman, D. J. Sahnow, M. Saisse, K. R. Sembach, H. A. Weaver, B. Y. Welsh, E. Wilkinson, and W. Zheng (2000). Overview of the Far Ultraviolet Spectroscopic Explorer Mission. *ApJ*, **538**, pp. L1–L6.

Morales-Rueda, L., T. R. Marsh, P. F. L. Maxted, G. Nelemans, C. Karl, R. Napiwotzki, and C. K. J. Moran (2005). Six detached white-dwarf close binaries. *MNRAS*, **359**, pp. 648–662. doi:10.1111/j.1365-2966.2005.08943.x.

Nelemans, G. and C. A. Tout (2005). Reconstructing the evolution of white dwarf binaries: further evidence for an alternative algorithm for the outcome of the common-envelope phase in close binaries. *MNRAS*, **356**, pp. 753–764. doi: 10.1111/j.1365-2966.2004.08496.x.

Nelemans, G., F. Verbunt, L. R. Yungelson, and S. F. Portegies Zwart (2000). Reconstructing the evolution of double helium white dwarfs: envelope loss without spiral-in. *A&A*, **360**, pp. 1011–1018.

O'Brien, M. S., H. E. Bond, and E. M. Sion (2001). Hubble Space Telescope Spectroscopy of V471 Tauri: Oversized K Star, Paradoxical White Dwarf. *ApJ*, **563**, pp. 971–986.

Oegerle, W., E. Murphy, and J. Kriss (2000). *The FUSE Data Handbook, Version 1.1*. User's Guide, Far Ultraviolet Spectroscopic Explorer, 4 February 2000. Baltimore: Johns Hopkins University.

Orosz, J. A., R. A. Wade, J. J. B. Harlow, J. R. Thorstensen, C. J. Taylor, and M. Eracleous (1999). The Post-Common Envelope and Pre-Cataclysmic Binary PG 1224+309. *AJ*, **117**, pp. 1598–1608.

Paczyński, B. (1971). Evolutionary Processes in Close Binary Systems. *ARA&A*, **9**, pp. 183–+. doi:10.1146/annurev.aa.09.090171.001151.

Paczynski, B. (1976). Common Envelope Binaries. In *IAU Symp. 73: Structure and Evolution of Close Binary Systems*, pp. 75–+.

Paczyński, B. and J. Ziółkowski (1967). Evolution of Close Binaries. III. *Acta Astronomica*, **17**, pp. 7–+.

Perlmutter, S., G. Aldering, G. Goldhaber, R. A. Knop, P. Nugent, P. G. Castro, S. Deustua, S. Fabbro, A. Goobar, D. E. Groom, I. M. Hook, A. G. Kim, M. Y. Kim, J. C. Lee, N. J. Nunes, R. Pain, C. R. Pennypacker, R. Quimby, C. Lidman, R. S. Ellis, M. Irwin, R. G. McMahon, P. Ruiz-Lapuente, N. Walton, B. Schaefer, B. J. Boyle, A. V. Filippenko, T. Matheson, A. S. Fruchter, N. Panagia, H. J. M. Newberg, W. J. Couch, and The Supernova Cosmology Project (1999). Measurements of Omega and Lambda from 42 High-Redshift Supernovae. *ApJ*, **517**, pp. 565–586. doi:10.1086/307221.

Pickles, A. J. (1998). A Stellar Spectral Flux Library: 1150-25000 Å. *PASP*, **110**, pp. 863–878.

Pollacco, D. L. and S. A. Bell (1994). A preliminary analysis of the planetary nebula central star V477 Lyrae. *MNRAS*, **267**, pp. 452–464.

Rappaport, S., F. Verbunt, and P. C. Joss (1983). A new technique for calculations of binary stellar evolution, with application to magnetic braking. *ApJ*, **275**, pp. 713–731. doi:10.1086/161569.

Riess, A. G., W. H. Press, and R. P. Kirshner (1996). A Precise Distance Indicator: Type IA Supernova Multicolor Light-Curve Shapes. *ApJ*, **473**, pp. 88–+. doi: 10.1086/178129.

Ritter, H. (1986). Precataclysmic binaries. *A&A*, **169**, pp. 139–148.

Schmidt, B. P., N. B. Suntzeff, M. M. Phillips, R. A. Schommer, A. Clocchiatti, R. P. Kirshner, P. Garnavich, P. Challis, B. Leibundgut, J. Spyromilio, A. G. Riess, A. V. Filippenko, M. Hamuy, R. C. Smith, C. Hogan, C. Stubbs, A. Diercks, D. Reiss, R. Gilliland, J. Tonry, J. Maza, A. Dressler, J. Walsh, and R. Ciardullo (1998). The High-Z Supernova Search: Measuring Cosmic Deceleration and Global Curvature of the Universe Using Type IA Supernovae. *ApJ*, **507**, pp. 46–63. doi:10.1086/306308.

Schreiber, M. R. and B. T. Gänsicke (2003). The age, life expectancy, and space density of Post Common Envelope Binaries. *A&A*, **406**, pp. 305–321.

Schwarzenberg-Czerny, A. (1989). On the advantage of using analysis of variance for period search. *MNRAS*, **241**, pp. 153–165.

Shapiro, S. L. and S. A. Teukolsky (1983). *Black holes, white dwarfs, and neutron stars: The physics of compact objects*. Research supported by the National Science Foundation. New York, Wiley-Interscience, 1983, 663 p.

Shortridge, K. (2001). Starlink User Note. p. 86.19.

Silvestri, N. M., T. D. Oswalt, M. A. Wood, J. A. Smith, I. N. Reid, and E. M. Sion (2001). White Dwarfs in Common Proper Motion Binary Systems: Mass Distribution and Kinematics. *AJ*, **121**, pp. 503–516. doi:10.1086/318005.

Sing, D. K., J. B. Holberg, M. A. Barstow, M. Burleigh, S. Good, T. Oswalt, S. Howell, and C. Brinkworth (2003). HS1136+6646: A Hot DAO.5+K6V Young Post-CE Pre-CV Binary. In *NATO ASIB Proc. 105: White Dwarfs*, pp. 349–+.

Sing, D. K., J. B. Holberg, M. R. Burleigh, S. A. Good, M. A. Barstow, T. D. Oswalt, S. B. Howell, C. S. Brinkworth, M. Rudkin, K. Johnston, and S. Rafferty (2004a). Spectroscopic and Photometric Analysis of HS 1136+6646: A Hot Young DAO+K7 V Post-Common-Envelope, Pre-Cataclysmic Variable Binary. *AJ*, **127**, pp. 2936–2947.

Sing, D. K., S. B. Howell, P. Szkody, and F. A. Cordova (2004b). Far Ultraviolet Spectroscopic Explorer Spectroscopy of the Transitional Magnetic Cataclysmic Variable V405 Aurigae. *PASP*, **116**, pp. 1056–1060. doi:10.1086/426124.

Smith, M. A. (1979). Rotational studies of lower main-sequence stars. *PASP*, **91**, pp. 737–745.

Solheim, J.-E. and L. R. Yungelson (2005). The White Dwarfs in AM CVn Systems – Candidates for SN Ia? In *ASP Conf. Ser. 334: 14th European Workshop on White Dwarfs*, pp. 387–+.

Stark, M. A. (2005). *Ph.D. Thesis*.

Stellingwerf, R. F. (1978). Period determination using phase dispersion minimization. *ApJ*, **224**, pp. 953–960.

Strolger, L.-G., A. G. Riess, T. Dahlen, M. Livio, N. Panagia, P. Challis, J. L. Tonry, A. V. Filippenko, R. Chornock, H. Ferguson, A. Koekemoer, B. Mobasher, M. Dickinson, M. Giavalisco, S. Casertano, R. Hook, S. Blondin, B. Leibundgut, M. Nonino, P. Rosati, H. Spinrad, C. C. Steidel, D. Stern, P. M. Garnavich, T. Matheson, N. Grogin, A. Hornschemeier, C. Kretchmer, V. G. Laidler, K. Lee, R. Lucas, D. de Mello, L. A. Moustakas, S. Ravindranath, M. Richardson, and E. Taylor (2004). The Hubble Higher z Supernova Search: Supernovae to z ˜ 1.6 and Constraints on Type Ia Progenitor Models. *ApJ*, **613**, pp. 200–223. doi: 10.1086/422901.

Szkody, P., J. Armstrong, and R. Fried (2000). Extreme Ultraviolet Explorer and Optical Observations of the Magnetic Cataclysmic Variables RX J1015.5+0904 and V405 Auriga (RX J0558+5353). *PASP*, **112**, pp. 228–236.

Szkody, P., P. Garnavich, S. Howell, and T. Kii (1990). New DQ Hers. In *Accretion-Powered Compact Binaries*, pp. 251–+.

Tegmark, M., M. A. Strauss, M. R. Blanton, K. Abazajian, S. Dodelson, H. Sandvik, X. Wang, D. H. Weinberg, I. Zehavi, N. A. Bahcall, F. Hoyle, D. Schlegel, R. Scoccimarro, M. S. Vogeley, A. Berlind, T. Budavari, A. Connolly, D. J. Eisenstein, D. Finkbeiner, J. A. Frieman, J. E. Gunn, L. Hui, B. Jain, D. Johnston, S. Kent, H. Lin, R. Nakajima, R. C. Nichol, J. P. Ostriker, A. Pope, R. Scranton, U. Seljak, R. K. Sheth, A. Stebbins, A. S. Szalay, I. Szapudi, Y. Xu, J. Annis, J. Brinkmann, S. Burles, F. J. Castander, I. Csabai, J. Loveday, M. Doi, M. Fukugita, B. Gillespie, G. Hennessy, D. W. Hogg, Ž. Ivezić, G. R. Knapp, D. Q. Lamb, B. C. Lee, R. H. Lupton, T. A. McKay, P. Kunszt, J. A. Munn, L. O'Connell, J. Peoples, J. R. Pier, M. Richmond, C. Rockosi, D. P. Schneider, C. Stoughton, D. L. Tucker, D. E. vanden Berk, B. Yanny, and D. G. York (2004). Cosmological parameters from SDSS and WMAP. *Phys. Rev. D*, **69**(10), pp. 103501–+. doi:10.1103/PhysRevD.69.103501.

Vennes, S., J. Dupuis, S. Bowyer, and A. K. Pradhan (1997). The Accreting White Dwarf in the Close Binary EUVE J1016-053. *ApJ*, **482**, pp. L73+. doi: 10.1086/310690.

Webbink, R. F. (1984). Double white dwarfs as progenitors of R Coronae Borealis stars and Type I supernovae. *ApJ*, **277**, pp. 355–360. doi:10.1086/161701.

Weidemann, V. (2000). Revision of the initial-to-final mass relation. *A&A*, **363**, pp. 647–656.

Wood, M. A. (1995). Theoretical White Dwarf Luminosity Functions: DA Models. *LNP Vol. 443: White Dwarfs*, **443**, pp. 41–+.

Woźniak, P. R., W. T. Vestrand, C. W. Akerlof, R. Balsano, J. Bloch, D. Casperson, S. Fletcher, G. Gisler, R. Kehoe, K. Kinemuchi, B. C. Lee, S. Marshall, K. E. McGowan, T. A. McKay, E. S. Rykoff, D. A. Smith, J. Szymanski, and J. Wren (2004). Northern Sky Variability Survey: Public Data Release. *AJ*, **127**, pp. 2436–2449. doi:10.1086/382719.

Young, P. A. and D. Arnett (2005). Observational Tests and Predictive Stellar Evolution. II. Nonstandard Models. *ApJ*, **618**, pp. 908–918. doi:10.1086/426131.

Zacharias, N., S. E. Urban, M. I. Zacharias, G. L. Wycoff, D. M. Hall, D. G. Monet, and T. J. Rafferty (2004). The Second US Naval Observatory CCD Astrograph Catalog (UCAC2). *AJ*, **127**, pp. 3043–3059. doi:10.1086/386353.